

Dissipative particle dynamics for advanced coarse-grained molecular dynamics simulation

Emadaldin Moeendarbary

2009

Emadaldin Moeendarbary. (2009). Dissipative particle dynamics for advanced coarse-grained molecular dynamics simulation. Master's thesis, Nanyang Technological University, Singapore.

<https://hdl.handle.net/10356/42231>

<https://doi.org/10.32657/10356/42231>

**DISSIPATIVE PARTICLE DYNAMICS FOR ADVANCED
COARSE-GRAINED MOLECULAR DYNAMICS
SIMULATION**

EMADALDIN MOEENDARBARY

School of Mechanical and Aerospace Engineering

A thesis submitted to the Nanyang Technological University
in fulfilment of the requirement for the degree of
Master of Engineering

2009

Dissipative Particle Dynamics for Advanced Coarse-Grained Molecular Dynamics Simulation

Emadaldin Moeendarbary

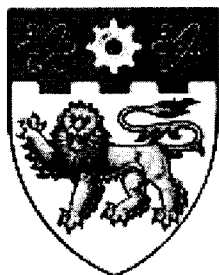
Supervisors:

Professor Lam Khin Yong

Associate Professor Ng Teng Yong

A thesis submitted to the Nanyang Technological University
in fulfillment of the requirement for the degree of
Master of Engineering (M.Eng Mechanical Engineering)

**Nanyang Technological
University**



**Agency for Science,
Technology and
Research**



Agency for
Science, Technology
and Research

SINGAPORE

Abstract

Recently advances in biological science have been dependent in corresponding advances in the field of DNA and protein separation. It therefore also requires the progress of the related electro-mechanical devices, in terms accuracy and speed of analysis. Most of these devices are composed of micro- and/or nano- channels which involve flow of complex phenomena. Our focus is on these micro/nano channel devices, consisting of many entropic traps, which were designed and fabricated for the separation of long DNA molecules. The channel comprises narrow constriction and wider regions that cause size-dependent trapping of DNA at the onset of a constriction. This process creates electrophoretic mobility differences, thus enabling efficient separation without gel matrix or pulsed electric fields [1-3]. Simulation and in particular numerical simulation is an efficient way to investigate the complex flow in the related electro-mechanical devices. Investigations for different simulation methods were carried out and we came into conclusion that the Dissipative Particle Dynamics method, which groups a number of atoms/molecules into particles, is most suitable for the above-mentioned applications. Dissipative Particle Dynamics (DPD) is a mesoscopic fluid modeling method, which facilitates the simulation of the statics and dynamics of complex fluid systems at physically interesting length and time scales. Currently, there are various applications of DPD, such as colloidal suspensions, multi-phase flow, rheology of polymer chains, DNA macromolecular suspension, etc., which employ this technique for their numerical simulation. The DPD technique is capable of modeling macroscopic properties of the bulk flow very well, but difficulties arise if the flows are confined through wall-bounded regions, or when different boundaries simultaneously exist in the simulation domain. These boundaries cause negative effects on the macroscopic temperature, density and

velocity profiles, as well as the shear stress and pressure distributions. In particular, the interaction of DPD particles with solid boundaries causes large density fluctuations at the near wall regions. This density distortion leads to pronounced fluctuations in the pressure and shear stress, which are not actually present.

To overcome these serious deficiencies, we introduce a new method in this work, which uses a combination of randomly distributed wall particles and a novel reflection adaptation at the wall. This new methodology is simple to implement and incurs no additional computational cost. More importantly, it does not cause any distortion in the macroscopic properties. This novel reflection adaptation is a novel version of the bounce back reflection, which we shall term the bounce-normal reflection. The most important characteristic of this method is that it reduces density fluctuations near the boundaries without affecting the velocity and temperature profiles. This new method is easily applicable to any wall-bounded problem with stationary boundaries and it has a very good consistency with macroscopic features. Following this numerical development work, we moved on to investigate suspension flow through micro/nano channels of fluidic NEMS/MEMS devices, with applications to DNA and protein separation. These micro/nano channel devices, consisting of many entropic traps, are designed and fabricated for the separation of proteins and long DNA molecules. The numerical results obtained compared very well with available experimental data, where counterintuitive behavior of longer DNA strands being able to escape through the traps in faster manner, was earlier observed [1-3].

To

my parents, *Badri & Alireza,*

and

my beloved wife, *Shima.*

Acknowledgments

I would like to express my greatest appreciation to my advisors, Professor Lam Khin Yong and Associate Professor Ng Teng Yong for their guidance and encouragement through this research project. It has been my privilege to have the opportunity to work with them and I really hope that this interaction continues in the future.

I am always grateful to all my teachers from Andishe primary school to Ejei-NODET secondary and high school (National Organization for Development of Exceptional Talents). Through their dedication, I acquired much basic knowledge, and more importantly, the enthusiasm to continue my education and the road to discovery through research.

I would like to acknowledge the financial support from the Singapore Agency for Science, Technology and Research (A*STAR) through the prestigious International Graduate Scholarship.

Contents

ABSTRACT	I
ACKNOWLEDGMENTS	IV
LIST OF TABLES	VIII
CHAPTER 1	
INTRODUCTION	1
1.1 Complex flow Simulation Techniques	1
1.2 Dissipative Particle Dynamics: A Coarse-Grained Technique	3
1.3 Research Objectives	4
1.4 Thesis Outline	5
CHAPTER 2	
THEORETICAL ASPECTS OF DPD	7
2.1 The DPD Algorithm	7
2.2 Derivation of Fokker-Planck Equation	10
2.3 DPD H-Theorem	14
CHAPTER 3	
BOUNDARY MODELS IN DPD	19
3.1 Introduction	19
3.2 DPD Boundary Conditions	20
3.3 The Periodic Boundary Conditions	21
3.4 The Lees-Edward Boundary Conditions	23
3.5 Freezing and Reflecting Boundary Conditions	26
CHAPTER 4	
DPD SIMULATION METHODS AND PARAMETERS	35
4.1 Neighbor List Method and Linear Scaling	35

4.2	Numerical Time Integration Schemes	39
4.3	The Noise Amplitude and Maxwellian Distribution	43
4.4	Random Generator and Choice of Random Numbers	45
 CHAPTER 5		
SIMULATION RESULTS		47
5.1	Macroscopic Transport Properties (Data Analysis)	47
5.1.1	Density Profiles and Diffusion Coefficient	48
5.1.2	Velocity and Temperature Profiles	49
5.1.3	Stress Tensor	50
5.1.4	Shear Viscosity	52
5.2	Bounce Normal Reflection	53
5.3	Diagnostic DPD Simulations	55
5.3.1	Poiseuille Flow	55
5.3.2	Couette Flow	72
5.4	Lid-Driven Cavity with Low Reynolds Number	78
5.5	Conclusions	83
 CHAPTER 6		
POLYMER PHYSICS THEORY, BASIC CONCEPTS AND DPD		84
6.1	Ideal Chains	84
6.1.1	Radius of Gyration	86
6.1.2	Freely Rotating and Worm-Like Chain Models	87
6.1.3	Probability Distribution of End-to-End Distance of an Ideal Chain	89
6.1.4	Free Energy and Entropic Elasticity of an Ideal Chain	90
6.2	Non-Ideal Chains (More Realistic Polymers)	94
6.3	Coarse-Grained DPD Simulation of Polymer Chain	97
6.3.1	DPD Polymeric Models	98
6.3.2	DPD Simulation of Worm-Like Chain in a Dilute Solution and Scaling Laws	102
 CHAPTER 7		
DISSIPATIVE PARTICLE DYNAMICS SIMULATION OF DNA SEPARATION IN ENTROPIC TRAP		112
7.1	Motivation	112
7.2	Entropic Trapping – Theory and Experiment	113
7.2.1	Experimental background	113
7.2.2	Theoretical aspects	115
7.2.3	Numerical Simulation	117
7.3	Description of Simulation Model and Parameters	121
7.3.1	DPD Algorithm and Chain Model	121

7.3.2	Microchannel Geometry and Wall Boundary Conditions	122
7.4	Results and Discussions	126
7.5	Concluding Remarks	129
CHAPTER 8		
CONCLUDING REMARKS AND FUTURE PERSPECTIVE		139
8.1	Concluding Remarks and Major Contribution	139
8.2	Possible Future Work	140
8.2.1	Theoretical Aspects	140
8.2.2	Applications	141
PUBLICATIONS ARISING FROM THESIS		143
REFERENCES:		144

List of Tables

Table 6-1 Two and three dimensional critical exponent for different solvent conditions.	97
Table 6-2 DPD simulation parameters for 2D simulation.	106
Table 7-1 DPD simulation parameters.	121
Table 7-2 Simulation parameter sets for WLC model.	122
Table 7-3 The dimensions of the microchannel.	123

List of Figures

Figure 1.1 Dissipative Particle Dynamics: Bridging the gap between Micro-scale and Macro-scale.	3
Figure 3.1 A two-dimensional periodic system. Particles can enter and leave each box across each of the four edges. In a three-dimensional case, particles would be free to cross any of the six cube faces [35].	23
Figure 3.2 Homogeneous shear boundary conditions (Lees-Edward method) [35].	25
Figure 3.3 Schematic sketch of periodic Poiseuille flow method (a new kind of Lees-Edwards boundary conditions).	26
Figure 3.4 Total force exerted by wall particles to a point that moves on the center line of the flat wall.	32
Figure 3.5 Total force exerted by two-layer wall particles to a point that moves on the center line of the flat wall.	32
Figure 4.1 Plot of computational cost (time in minutes), comparison between the neighbor-list and Verlet-list methods.	39
Figure 4.2 Temperature deviations versus size of time step for Euler method, simple Verlet method and Verlet method with optimum λ parameter.	43
Figure 4.3 Results of momentum distribution for different timestep sizes.	44
Figure 4.4 Plot of temperature variation against the time for different values of noise amplitude.	45
Figure 5.1 Schematic diagram of bounce-back (bb), bounce-forward (bf), specular (Spec) and bounce-normal (bn) for particle that penetrates into the stationary wall region.	55
Figure 5.2 The 3D and 2D position of the wall (blue balls) and the fluid (green small balls) DPD particles distribution in the simulation box.	57
Figure 5.3 Top: Density profile. Middle: Temperature and Velocity profiles. Bottom: Shear Stress Profile. The Navier-Stokes solutions are shown with solid lines. Model with walls of random frozen particles ($\rho_w = \rho_f$; $a_{wf} = a_{ff}$).	59
Figure 5.4 Top: Density profile. Middle: Temperature and Velocity profiles. Bottom: Shear Stress Profile. The Navier-Stokes solutions are shown with solid lines. Model with walls of random frozen particles ($\rho_w = 2\rho_f$; $a_{wf} = a_{ff}$).	60
Figure 5.5 Top: Density profile. Middle: Temperature and Velocity profiles. Bottom: Shear Stress Profile. The Navier-Stokes solutions are shown with solid lines. Model with walls of random frozen particles ($\rho_w = \rho_f$; $a_{wf} = 2a_{ff}$).	61
Figure 5.6 Top: Density profile. Middle: Temperature and Velocity profiles. Bottom: Shear Stress Profile. The Navier-Stokes solutions are shown with solid lines. Model with walls of random frozen particles combined with bounce-back reflection ($\rho_w = \rho_f$; $a_{wf} = a_{ff}$).	64
Figure 5.7 Top: Density profile. Middle: Temperature and Velocity profiles. Bottom: Shear Stress Profile. The Navier-Stokes solutions are shown with solid lines.	

Model with walls of two layer structured particles combined with bounce-back reflection ($\rho_w = \rho_f$; $a_{wf} = 0.3766a_{ff}$).....	65
Figure 5.8 Top: Pressure profile. Bottom: First and second normal stress differences profiles. Model with walls of random frozen particles combined with bounce-back reflection ($\rho_w = \rho_f$; $a_{wf} = a_{ff}$).....	66
Figure 5.9 Top: Density profile. Middle: Temperature and Velocity profiles. Bottom: Shear Stress Profile. The Navier-Stokes solutions are shown with solid lines. Model with walls of random frozen particles combined with bounce-normal reflection ($\rho_w = \rho_f$; $a_{wf} = a_{ff}$).....	67
Figure 5.10 Top: Pressure profile. Bottom: First and second normal stress differences profiles. Model with walls of random frozen particles combined with bounce-normal reflection ($\rho_w = \rho_f$; $a_{wf} = a_{ff}$).....	68
Figure 5.11 Top: Density profile. Middle: Temperature and Velocity profiles. Bottom: Shear Stress Profile. The Navier-Stokes solutions are shown with solid lines. Model with walls of random frozen particles combined with bounce-normal reflection ($\rho_w = \rho_f = 9$; $a_{wf} = a_{ff}$).....	71
Figure 5.12 Couette flow. Top: Density and Temperature profiles. Middle: Velocity profile. Bottom: Shear Stress Profile. The Navier-Stokes solutions are shown with solid lines. Model with walls of random frozen particles combined with bounce-normal reflection ($\rho_w = \rho_f = 4$; $a_{wf} = 0.7a_{ff}$).....	74
Figure 5.13 Couette flow. Top: Density and Temperature profiles. Middle: Velocity profile. Bottom: Shear Stress Profile. The Navier-Stokes solutions are shown with solid lines. Model with walls of random frozen particles combined with bounce-normal reflection ($\rho_w = \rho_f = 4$; $a_{wf} = 0.3766a_{ff}$).....	75
Figure 5.14 Couette flow. Top: Density and Temperature profiles. Middle: Velocity profile. Bottom: Shear Stress Profile. The Navier-Stokes solutions are shown with solid lines. Model with walls of random frozen particles combined with bounce-normal reflection ($\rho_w = 10$; $a_{wf} = 0.3766a_{ff}$).....	76
Figure 5.15 Couette flow. Top: Pressure profile. Bottom: First and second normal stress differences profiles. Model with walls of random frozen particles combined with bounce-normal reflection ($\rho_w = 10$; $a_{wf} = 0.3766a_{ff}$).....	77
Figure 5.16 Contour plot of lid-driven cavity flow. Left: Total velocity of DPD simulation. Right: Total velocity of Navier-Stokes simulation.	80
Figure 5.17 Contour plot of lid-driven cavity flow. Left: V-component velocity of DPD simulation. Right: V-component velocity of Navier-Stokes simulation.	80
Figure 5.18 Contour plot of lid-driven cavity flow. Left: U-component velocity of DPD simulation. Right: U-component velocity of Navier-Stokes simulation.	81
Figure 5.19 DPD and Navier-Stokes comparison of velocity profiles. Left: U and V profiles along the horizontal line at $y=0.25$. Right: U and V profiles along the vertical line at $x=0.25$. (DPD Results are shown with dotted lines)	81

Figure 5.20 DPD and Navier-Stokes comparison of velocity profiles. Left: U and V profiles along the horizontal line at $y=0.5$. Right: U and V profiles along the vertical line at $x=0.5$. (DPD Results are shown with dotted lines)	82
Figure 5.21 DPD and Navier-Stokes comparison of velocity profiles. Left: U and V profiles along the horizontal line at $y=0.75$. Right: U and V profiles along the vertical line at $x=0.75$. (DPD Results are shown with dotted lines)	82
Figure 6.1 The atomic and overall structure of sample polymer chain.....	84
Figure 6.2 Schematic of end-to-end distance of one conformation of a flexible polymer. The vector lines represent sample actual links in the chain and the rest of the contour of the chain is represented by curved dotted line.	86
Figure 6.3 Normalized distribution function of end-to-end distances of an ideal chain with different number of segments.....	90
Figure 6.4 Plot of normalized stretching force versus normalized average end-to-end distance for a Gaussian chain equation (6.19), freely jointed chain equation (6.20), and three models of worm-like chain. The data for exact worm-like chain (▲) are from [88].....	94
Figure 6.5 Lennard-Jones potential and the soft-repulsive potential after averaging. Figure extracted from [95].	99
Figure 6.6 A 40 bead 3D polymer chain at equilibrium state in a periodic box of solution.	102
Figure 6.7 The 2D representation of a 128 bead chain (blue balls) in a 20×20 simulation box. The yellow crossed circles show the positions of the ghost chain beads. The small green dots represent the solvent particles.	104
Figure 6.8 Left: Scaling of radius of gyration (red) or end-to-end distance (blue). Right: Ratio $\frac{\langle R^2 \rangle}{\langle R_g^2 \rangle}$ (red) and the chain temperature absolute error (blue). 3D Simulation parameters: $L_{sp} = 2$, $\lambda_p^{eff} = 1/7$, $a_{pf} = a_{ff}$, $k_B T = 0.2$, $L_c = 0.695$	107
Figure 6.9 Left: Scaling of radius of gyration (red) or end-to-end distance (blue). Right: Ratio $\frac{\langle R^2 \rangle}{\langle R_g^2 \rangle}$ (red) and the chain temperature absolute error (blue). Simulation parameters: $L_{sp} = 0.5$, $\lambda_p^{eff} = 0.05$, $a_{pf} = a_{ff}$, $L_c = 0.253$	107
Figure 6.10 Left: Scaling of radius of gyration (red) or end-to-end distance (blue). Right: Ratio $\frac{\langle R^2 \rangle}{\langle R_g^2 \rangle}$ (red) and the chain temperature absolute error (blue). Simulation parameters: $L_{sp} = 0.5$, $\lambda_p^{eff} = 0.15$, $a_{pf} = a_{ff}$, $L_c = 0.304$	108
Figure 6.11 Left: Scaling of radius of gyration (red) or end-to-end distance (blue). Right: Ratio $\frac{\langle R^2 \rangle}{\langle R_g^2 \rangle}$ (red) and the chain temperature absolute error (blue). Simulation parameters: $L_{sp} = 1$, $\lambda_p^{eff} = 0.15$, $a_{pf} = a_{ff}$, $L_c = 0.434$	108

Figure 6.12 Left: Scaling of radius of gyration (red) or end-to-end distance (blue). Right: Ratio $\frac{\langle R^2 \rangle}{\langle R_g^2 \rangle}$ (red) and the chain temperature absolute error (blue). Simulation parameters: $L_{sp} = 1.5$, $\lambda_p^{eff} = 0.15$, $a_{pf} = a_{ff}$, $L_c = 0.525$	109
Figure 6.13 Left: Scaling of radius of gyration (red) or end-to-end distance (blue). Right: Ratio $\frac{\langle R^2 \rangle}{\langle R_g^2 \rangle}$ (red) and the chain temperature absolute error (blue). Simulation parameters: $L_{sp} = 1.5$, $\lambda_p^{eff} = 0.15$, $a_{pf} = 0.75a_{ff}$, $L_c = 0.613$	109
Figure 6.14 Left: Scaling of radius of gyration (red) or end-to-end distance (blue). Right: Ratio $\frac{\langle R^2 \rangle}{\langle R_g^2 \rangle}$ (red) and the chain temperature absolute error (blue). Simulation parameters: $L_{sp} = 1.5$, $\lambda_p^{eff} = 0.15$, $a_{pf} = 0.5a_{ff}$, $L_c = 0.667$	110
Figure 6.15 Left: Scaling of radius of gyration (red) or end-to-end distance (blue). Right: Ratio $\frac{\langle R^2 \rangle}{\langle R_g^2 \rangle}$ (red) and the chain temperature absolute error (blue). Simulation parameters: $L_{sp} = 1.5$, $\lambda_p^{eff} = 0.15$, $a_{pf} = 1.25a_{ff}$, $L_c = 0.485$	110
Figure 6.16 Left: Scaling of radius of gyration (red) or end-to-end distance (blue). Right: Ratio $\frac{\langle R^2 \rangle}{\langle R_g^2 \rangle}$ (red) and the chain temperature absolute error (blue). Simulation parameters: $L_{sp} = 1.5$, $\lambda_p^{eff} = 0.15$, $a_{pf} = a_{ff}$, $L_c = 0.566$, $S = 2$, $a_{pp} = 2a_{ff}$	111
Figure 7.1 schematic diagram of nanofluidic separation device (adapted from Han et al. [1-3]).....	117
Figure 7.2 Top: The electric potential ϕ contour plot and representation of several electric field vectors near the slit. Bottom: The x-component of the electric field inside the channel E_x , as a function of length of channel, measured along the plane in middle of the shallow region.....	124
Figure 7.3 Top: The electric field x-component E_x contour plot. Bottom: The electric field y-component E_y contour plot.....	125
Figure 7.4 The x -component of the center of mass trajectories of DNA chains of $N = 5, 10, 20, 40, 80$ beads for the case of $E_{av} = 0.5$ and $L_{sp} = 4$	129
Figure 7.5 Top: Dimensionless mobility μ of DNA chains for $E_{av} = 0.0625, 0.125, 0.25, 0.5$ as a function of N . Bottom: Dimensionless mobility μ of DNA chains for $N = 5, 10, 20, 40, 80, 160$ as a function of E_{av}	131
Figure 7.6 Traverse (or xy) view of the center of mass trajectories (blue lines) of migrating DNA chains of different sizes through array for the case of $E_{av} = 0.5$ and $L_{sp} = 4$. Top: $N = 5$. Middle: $N = 20$. Bottom: $N = 80$	132

Figure 7.7 Conformation evolution snapshots of DNA chain with $N = 80$ beads passing through trap for case of $E_{av} = 0.5$ and $L_{sp} = 4$. Traverse (or xy) view of translations from (a) time $t = 3600$ to (f) time $t = 4000$.	133
Figure 7.8 Conformation evolution snapshots of DNA chain with $N = 80$ beads passing through trap for case of $E_{av} = 0.5$ and $L_{sp} = 4$. Top (or xz) view of translations from (a) time $t = 3600$ to (f) time $t = 4000$.	134
Figure 7.9 Conformation evolution snapshots of DNA chain with $N = 80$ beads passing through trap for case of $E_{av} = 0.5$ and $L_{sp} = 4$. Traverse (or xy) view of translations from (a) time $t = 5520$ to (j) time $t = 5820$.	135
Figure 7.10 Conformation evolution snapshots of DNA chain with $N = 80$ beads passing through trap for case of $E_{av} = 0.5$ and $L_{sp} = 4$. Top (or xz) view of translations from (a) time $t = 5520$ to (j) time $t = 5820$.	137

Chapter 1

Introduction

This chapter provides an introduction to fluid simulation techniques and examines some features of these methods especially for the complex systems. We also identify the dissipative particle dynamics as a mesoscopic technique. Finally, we present the layout of the current work.

1.1 Complex flow Simulation Techniques

A complex flow system is one in which the observable properties and behaviors have significant dependency on the microscopic structure of the fluid. There exists a broad application of such systems especially in the field of biological and biomedical sciences (biochemical lab on chip systems, DNA separation devices, and drug delivery systems).

The rapid progress in the development of micro- and nano-electromechanical systems (MEMS/NEMS) is leading to the need for continuous improvements in the modeling approaches. Numerical simulation is a way to simulate these complex systems, which usually involves simulation of coupled electrical, mechanical, thermal and fluid domains. In addition there exists other features of geometrical complexity and suspension of different particles or polymers (DNA chains) in the domain. As device dimensions continue to decrease, conventional (macroscopic) theories are being challenged and often

new computational models are required. Accurate and reliable computational approaches are essential for the design of efficient and robust micro/nano-systems. In general there are three methods for the simulation of such systems, namely: molecular dynamics (MD), continuum methods (Navier-Stokes) and mesoscopic methods, and each of these may have their own characteristics, advantages and disadvantages.

A simple fluid can be described by continuum Navier-Stokes equations and sophisticated computational techniques have been developed over the years for the solution of these differential equations on macroscopic scales. In order to reduce the computational complexity, the employed numerical discretization should be both highly efficient as well as robust. Usually, discretization methods are based on finite-differences, finite-elements or finite volumes. There are also some other similar techniques like spectral element (high order finite-element), meshfree methods and the force coupling method, each of which are appropriate for different applications. However these methods can only include the macroscopic details of the fluid in a phenomenological manner and are thus not suited for many complex fluid applications.

On a microscopic scale, the MD method allows the simulation of very small volumes of liquid flow by following the position and the momentum of every atom/molecule in the fluid. On this level the order of dimensions in MD method are perhaps of 100nm or less, and the simulated phenomenon time is of the order of several nanoseconds. MD can deal effectively with nano-domains and is perhaps the only accurate approach in simulating flows involving very high shear where the continuum or the Newtonian hypothesis may not be valid. For dimensions less than approximately ten molecules the continuum hypothesis breaks down for liquids and MD should be employed to simulate the atomistic behavior of such a system [4]. Although MD approaches have become

increasingly successful in the simulation of a small number of atoms/molecules, it is not easy to apply these microscopic techniques to large complex fluid systems because of its huge computational cost.

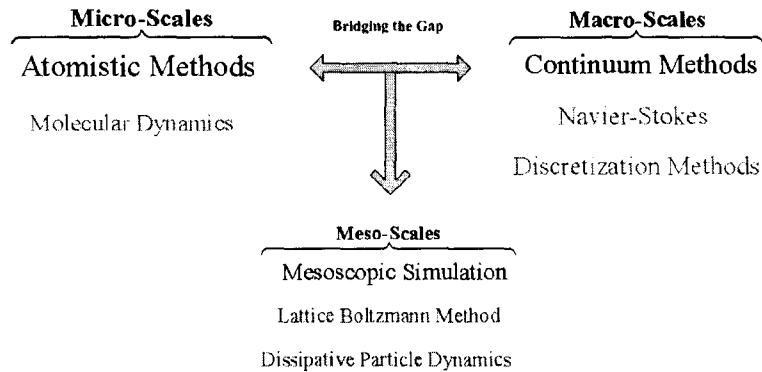


Figure 1.1 Dissipative Particle Dynamics: Bridging the gap between Micro-scale and Macro-scale.

To bridge the gap between atomistic simulations and macroscopic network simulations, we need an intermediary technique focused at a length scale larger than the atomistic scale, but smaller than the macroscopic connection scale [5, 6], as shown in Figure 1.1. Mesoscopic fluid simulations are methods which overcome the inherent difficulties faced by conventional methods when applied to complex fluids. Its aim is to identify characteristic physical lengths and times in the system in order to use them for simplification of the complex models.

1.2 Dissipative Particle Dynamics: A Coarse-Grained Technique

The dissipative particle dynamics (DPD) is a potentially very powerful and simple mesoscopic approach, which facilitates the simulation of the statics and dynamics of complex fluid systems at physically interesting length and time scales. Since 1990, when the method was first developed in Europe, DPD has been applied in the study of the

dynamical properties of a wide variety of systems and applications, including colloidal suspensions [7, 8], dilute polymer solutions [9, 10], block-copolymer melts [10, 11], surfactants [12, 13], biological membranes [5, 14] and DNA suspension [15]. We can perceive this method as grouping a number of molecules into single particle and the number of molecules per DPD particle is known as the coarse-graining parameter and is denoted by N_m . One of the most important issues is to find the upper limit for this coarse-graining parameter by which we could model the physical properties in an efficient manner. The vital role of N_m become more obvious when we find that it has a significant impact on the speed of simulation. According to [5] the DPD total speed up of simulation with respect to MD method is $1000 N_m^{8/3}$ for a given system volume. Thus, for $N_m = 3$ and 7 the speed-up factor is roughly about 2×10^4 and 2×10^5 , respectively.

1.3 Research Objectives

The three main objectives of this M.Eng research are:

- 1). Refinement of the DPD method so as to obtain the correct macroscopic flow properties. To achieve this, we aim to improve on the simulation model, such as the wall particle distribution and boundary reflection mechanism.
- 2). Optimizing the DPD coarse grained parameters (bead spring models) to achieve an accurate and efficient model for the rheology of polymers under various conditions, and to develop a proper DNA chain model to be coupled with the DPD method.
- 3). Following the development of a sufficiently refined DPD methodology, we will then apply it to study the process of DNA separation through entropic traps.

1.4 Thesis Outline

- In Chapter 2 the basics of the DPD algorithm is introduced and some of the theoretical aspects of this algorithm, especially the derivation of the Fokker-Planck equations are established. The objective of this chapter is to determine the detailed balance condition for DPD modeling.
- In Chapter 3 we provide a comprehensive literature review for DPD boundary models. In this chapter we also introduce and examine some of the main difficulties in implementing boundary conditions and introduce the well-known methods in applying the boundaries for the bulk flow and flow in confined geometries.
- In Chapter 4 we return to the DPD algorithm and introduce the optimum serial algorithms for implementation of DPD in computer programming. Then we study some algorithms for time evolution schemes in DPD. Finally we examine and determine suitable values for the DPD parameters.
- In Chapter 5 the techniques for data analysis, and the connection between microscopic and macroscopic properties, are introduced. The new bounce normal boundary condition is then proposed and it is subjected to various test cases. We examine different boundary conditions numerically for two cases of Poiseuille and Couette flow and study the effects of boundary models on macroscopic properties. Finally we employ the bounce normal reflection to explore lid driven cavity flow.
- In Chapter 6 we introduce the concept of an ideal chain and derive the basic relations for radius of gyration and end-to-end distance. Subsequently, by deriving the

Chapter 1: Introduction

entropic elasticity of the polymer chain, we find the Hookean spring definition for an ideal chain. Next, real chains and the excluded volume effects are explained briefly and the scaling laws for polymers are introduced. The worm-like chain (WLC) is studied in detail. In the last part of this chapter we introduce the coarse-grained DPD simulation for polymeric systems and finally investigate DPD scaling laws for the WLC in dilute solution.

- In Chapter 7, the entropic trap which is a new method for separation of DNA molecules is introduced and the process is simulated using the DPD method with WLCs to mimic the DNAs. As a result, motilities of different chain sizes are found and some of the main underlying physics that cause delay in migration of small chains are discussed.
- In Chapter 8, concluding remarks are made, and the major contributions of this thesis are highlighted. In addition, possible future works are proposed.

Chapter 2

Theoretical Aspects of DPD

The theoretical connection between Dissipative Particle Dynamics and continuum fluid mechanics can be demonstrated by deriving the Fokker-Planck equation. It is the essential formulism for derivation of kinetic and hydrodynamic equations [16]. The Fokker-Planck equation governs the N -particle distribution function that gives the probability density of the system position and momentum. It is related to DPD by the corresponding Langevin equations, which are the stochastic differential equations for the dynamics of particles subjected to conservative, dissipative, and random forces. Here we present the Marsh [17] derivation of the Fokker-Planck equation that corresponds to the stochastic differential for DPD, and proves an H-theorem for the DPD algorithm that ensures the Gibbs distribution is the inevitable equilibrium distribution.

2.1 The DPD Algorithm

The Dissipative Particle Dynamics (DPD) is an alternative method for mesoscopic fluid simulation, which was first introduced by Hoogerbrugge and Koelman [18], and was modified by Espanol and Warren [19]. The DPD algorithm is a combination of molecular dynamics, Brownian dynamics and lattice gas automata, and derives its static and dynamic properties according to the theory in statistical mechanics [16].

Chapter 2: Theoretical Aspects of DPD

Similar to molecular dynamics, the time evolution of each DPD particle, which represents a cluster of molecules/atoms, can be calculated by Newton's second law

$$\frac{d\mathbf{r}_i}{dt} = \mathbf{v}_i, \quad \frac{d\mathbf{p}_i}{dt} = \sum_{j \neq i} \mathbf{F}_{ij}, \quad (2.1)$$

where \mathbf{r}_i , \mathbf{v}_i and $\mathbf{p}_i = m\mathbf{v}_i$ are respectively the position, velocity and momentum vectors of particle i , and \mathbf{F}_{ij} is the total interparticle force exerting on particle i by particle j . In this work we assume the mass of each particle m_i , to be unity. The interparticle force is defined by three components that lie along their lines of centers and conserves linear and angular momentum: a purely repulsive conservative force \mathbf{F}_{ij}^C , a dissipative or frictional force \mathbf{F}_{ij}^D which represents the effects of viscosity and slows down the particles motion with respect to each other, and the random (stochastic) force \mathbf{F}_{ij}^R which represents the thermal or vibrational energy of system,

$$\mathbf{F}_{ij} = \mathbf{F}_{ij}^C + \mathbf{F}_{ij}^D + \mathbf{F}_{ij}^R, \quad (2.2)$$

$$\mathbf{F}_{ij}^C = w^C(r_{ij}) \mathbf{e}_{ij}, \quad (2.3)$$

$$\mathbf{F}_{ij}^D = -\gamma w^D(r_{ij}) [\mathbf{v}_{ij} \cdot \mathbf{e}_{ij}] \mathbf{e}_{ij}, \quad (2.4)$$

$$\mathbf{F}_{ij}^R = \sigma w^R(r_{ij}) \theta_{ij} \mathbf{e}_{ij}, \quad (2.5)$$

where $\mathbf{e}_{ij} = \mathbf{r}_{ij} / r_{ij}$, $\mathbf{r}_{ij} = \mathbf{r}_i - \mathbf{r}_j$, $r_{ij} = |\mathbf{r}_i - \mathbf{r}_j|$ and $\mathbf{v}_{ij} = (\mathbf{v}_i - \mathbf{v}_j)$. w^C , w^D and w^R are the conservative dissipative and random r dependent weight functions. The θ_{ij} term is a Gaussian white noise function with symmetry property $\theta_{ij} = \theta_{ji}$ to ensure the total conservation of momentum and has the following stochastic properties

$$\langle \theta_{ij}(t) \rangle = 0, \quad \langle \theta_{ij}(t) \theta_{kl}(t') \rangle = (\delta_{ik} \delta_{jl} + \delta_{il} \delta_{jk}) \delta(t - t') \quad (2.6)$$

Chapter 2: Theoretical Aspects of DPD

All of the above forces are acting within a sphere of interaction or cutoff radius r_c which is the length scale parameter of the system. The γ and σ are the coefficients of the dissipative and random forces respectively. Similar to the fluctuation-dissipation theorem [20], Espanol and Warren [19] obtained the detailed balanced condition for the DPD as

$$w^D(r) = [w^R(r)]^2, \quad \sigma^2 = 2\gamma k_B T / m, \quad (2.7)$$

where k_B is the Boltzmann constant and T the equilibrium temperature. The conservative force weight function is given by

$$w^C(r_{ij}) = \begin{cases} a_{ij} (1 - \frac{r_{ij}}{r_c}) & r_{ij} \leq r_c \\ 0 & r_{ij} > r_c \end{cases} \quad (2.8)$$

where $a_{ij} = \sqrt{a_i a_j}$ is the repulsion parameter. We can match the compressibility condition and determine the repulsion parameter as a function of DPD number density ρ and system temperature which is applicable for fluid-fluid interactions [5, 6]

$$a_f = a_{ff} = 75 k_B T / \rho \quad (2.9)$$

The dissipative and random weight functions takes the general form [15]

$$w^D(r_{ij}) = [w^R(r_{ij})]^2 = \begin{cases} (1 - \frac{r_{ij}}{r_c})^s & r_{ij} \leq r_c \\ 0 & r_{ij} > r_c \end{cases} \quad (2.10)$$

In the present work which involves conventional DPD systems, we set the exponent parameter to $s = 2$. The random force transforms to $\mathbf{F}_{ij}^R = \sigma w^R(r_{ij}) \frac{\zeta_{ij}}{\sqrt{dt}} \mathbf{e}_{ij}$, where ζ_{ij} represents an independent increment in a stochastic process, which is represented by a uniform distribution of random numbers whose mean is zero with unit variance, and chosen independently for different pairs of particles at each time step.

2.2 Derivation of Fokker-Planck Equation

It can be demonstrated that every set of stochastic differential equations of the form of (2.1) is equivalent to a Fokker-Planck equation [21]. This Fokker-Planck equation is the analogue of the Liouville equation which would be relevant for a classical system. The equations (2.1) show the evolution of the variables of particular system with time, and therefore describe a particular path in phase space. In deriving the Fokker-Planck equation we are interested in a differential equation governing a large ensemble of such systems by the probability density function of the phase space $\rho(\Gamma, t)$, where Γ represents all the variables of the system and here they are the positions and velocities.

We start with the Chapman-Kolmogorov equation written in phase space. It is the fundamental equation of the Markov process [22], which states that the course of the system at a time t depends only upon the instantaneous state of the system at the time t and is independent of its previous history. Consider Δt be a small time step, during which \mathbf{p} changes. We can derive $\rho(\mathbf{r} + \Delta \mathbf{r}, \mathbf{p}, t + \Delta t)$ from $\rho(\mathbf{r}, \mathbf{p}, t)$ and a knowledge of the transition probability $\Psi(\mathbf{p}; \Delta \mathbf{p})$. In mathematical order we can state this by writing

$$\rho(\mathbf{r} + \Delta \mathbf{r}, \mathbf{p}, t + \Delta t) = \int_{\Delta \mathbf{p}} \rho(\mathbf{r}, \mathbf{p} - \Delta \mathbf{p}, t) \Psi(\mathbf{r}, \mathbf{p} - \Delta \mathbf{p}; \Delta \mathbf{p}) d(\Delta \mathbf{p}), \quad (2.11)$$

where $\Psi(\mathbf{r}, \mathbf{p} - \Delta \mathbf{p}; \Delta \mathbf{p})$ is a transition probability that gives the probability that a particle at the position $(\mathbf{r}, \mathbf{p} - \Delta \mathbf{p})$ in phase space jumps in momentum by $\Delta \mathbf{p}$ in the interval of Δt . This equation means that the probability of finding a particle at position $\mathbf{r} + \Delta \mathbf{r}$ at time $t + \Delta t$ with the momentum \mathbf{p} is the same as the probability that it was at position \mathbf{r} with momentum $\mathbf{p} - \Delta \mathbf{p}$ at time t and jumped an amount $\Delta \mathbf{p}$, summed over all possible values of $\Delta \mathbf{p}$.

Chapter 2: Theoretical Aspects of DPD

We now expand $\rho(\mathbf{r} + \Delta\mathbf{r}, \mathbf{p}, t + \Delta t)$, $\rho(\mathbf{r}, \mathbf{p} - \Delta\mathbf{p}, t)$ and $\Psi(\mathbf{r}, \mathbf{p} - \Delta\mathbf{p}; \Delta\mathbf{p})$ in Taylor series

$$\begin{aligned} & \rho(\mathbf{r}, \mathbf{p}, t) + \frac{\partial \rho}{\partial t} \Delta t + \sum_i \frac{\partial \rho}{\partial \mathbf{r}_i} \cdot \Delta \mathbf{r}_i + O(\Delta t^2) \\ &= \int_{\Delta \mathbf{p}} \left[\rho(\mathbf{r}, \mathbf{p}, t) - \sum_j \frac{\partial \rho}{\partial \mathbf{p}_j} \cdot \Delta \mathbf{p}_j + \frac{1}{2} \sum_j \frac{\partial^2 \rho}{\partial \mathbf{p}_j^2} : \Delta \mathbf{p}_j^2 + \sum_{i < j} \frac{\partial^2 \rho}{\partial \mathbf{p}_i \partial \mathbf{p}_j} : \Delta \mathbf{p}_i \Delta \mathbf{p}_j + \dots \right] \\ & \times \left[\Psi(\mathbf{r}, \mathbf{p}; \Delta \mathbf{p}) - \sum_j \frac{\partial \Psi}{\partial \mathbf{p}_j} \cdot \Delta \mathbf{p}_j + \frac{1}{2} \sum_j \frac{\partial^2 \Psi}{\partial \mathbf{p}_j^2} : \Delta \mathbf{p}_j^2 + \sum_{i < j} \frac{\partial^2 \Psi}{\partial \mathbf{p}_i \partial \mathbf{p}_j} : \Delta \mathbf{p}_i \Delta \mathbf{p}_j + \dots \right] d(\Delta \mathbf{p}) \end{aligned} \quad (2.12)$$

Then we can define the below averages

$$\begin{aligned} \langle \Delta \mathbf{p}_i \rangle &= \int_{-\infty}^{\infty} \Delta \mathbf{p}_i \Psi(\mathbf{r}, \mathbf{p}; \Delta \mathbf{p}) d(\Delta \mathbf{p}) \\ \langle \Delta \mathbf{p}_i^2 \rangle &= \int_{-\infty}^{\infty} \Delta \mathbf{p}_i^2 \Psi(\mathbf{r}, \mathbf{p}; \Delta \mathbf{p}) d(\Delta \mathbf{p}) \\ \langle \Delta \mathbf{p}_i \Delta \mathbf{p}_j \rangle &= \int_{-\infty}^{\infty} \Delta \mathbf{p}_i \Delta \mathbf{p}_j \Psi(\mathbf{r}, \mathbf{p}; \Delta \mathbf{p}) d(\Delta \mathbf{p}) \end{aligned} \quad (2.13)$$

We use $\int \rho(\mathbf{r}, \mathbf{p}, t) \Psi(\mathbf{r}, \mathbf{p}; \Delta \mathbf{p}) d(\Delta \mathbf{p}) = \rho(\mathbf{r}, \mathbf{p}, t)$ which is true because the probability density is independent of the momentum jump $\Delta \mathbf{p}$, and $\Delta \mathbf{r}_i = \frac{\mathbf{p}_i}{m} \Delta t$, then equation (2.12)

becomes

$$\begin{aligned} \left[\frac{\partial \rho}{\partial t} + \sum_i \frac{\partial \rho}{\partial \mathbf{r}_i} \cdot \frac{\mathbf{p}_i}{m} \right] \Delta t + O(\Delta t^2) &= - \sum_j \frac{\partial \rho}{\partial \mathbf{p}_j} \langle \Delta \mathbf{p}_j \rangle + \frac{1}{2} \sum_j \frac{\partial^2 \rho}{\partial \mathbf{p}_j^2} \langle \Delta \mathbf{p}_j^2 \rangle \\ &+ \sum_{i < j} \frac{\partial^2 \rho}{\partial \mathbf{p}_i \partial \mathbf{p}_j} \langle \Delta \mathbf{p}_i \Delta \mathbf{p}_j \rangle - \sum_j \rho \frac{\partial \langle \Delta \mathbf{p}_j \rangle}{\partial \mathbf{p}_j} \\ &+ \sum_j \frac{\partial}{\partial \mathbf{p}_j} \langle \Delta \mathbf{p}_j^2 \rangle \frac{\partial \rho}{\partial \mathbf{p}_j} + \sum_{i < j} \frac{\partial \rho}{\partial \mathbf{p}_i} \frac{\partial \langle \Delta \mathbf{p}_i \Delta \mathbf{p}_j \rangle}{\partial \mathbf{p}_j} \\ &+ \frac{1}{2} \sum_j \frac{\partial^2}{\partial \mathbf{p}_j^2} \langle \Delta \mathbf{p}_j^2 \rangle \rho + \sum_{i < j} \rho \frac{\partial^2 \langle \Delta \mathbf{p}_i \Delta \mathbf{p}_j \rangle}{\partial \mathbf{p}_j \partial \mathbf{p}_j} + \dots, \end{aligned} \quad (2.14)$$

Chapter 2: Theoretical Aspects of DPD

where the remaining terms involve quantities $\langle \Delta \mathbf{p}_j^3 \rangle$, $\langle \Delta \mathbf{p}_i \Delta \mathbf{p}_j^2 \rangle$, $\langle \Delta \mathbf{p}_i \Delta \mathbf{p}_j \Delta \mathbf{p}_k \rangle$ and higher-order terms. By neglecting all higher-order terms we obtain

$$\begin{aligned} \left[\frac{\partial \rho}{\partial t} + \sum_i \frac{\partial \rho}{\partial \mathbf{r}_i} \cdot \frac{\mathbf{p}_i}{m} \right] \Delta t = & - \sum_j \frac{\partial}{\partial \mathbf{p}_j} \cdot (\rho \langle \Delta \mathbf{p}_j \rangle) + \sum_{i < j} \frac{\partial^2}{\partial \mathbf{p}_i \partial \mathbf{p}_j} : (\rho \langle \Delta \mathbf{p}_i \Delta \mathbf{p}_j \rangle) \\ & + \frac{1}{2} \sum_j \frac{\partial^2}{\partial \mathbf{p}_j^2} : (\rho \langle \Delta \mathbf{p}_j^2 \rangle) \end{aligned} \quad (2.15)$$

which can be simplified to

$$\left[\frac{\partial \rho}{\partial t} + \sum_i \frac{\partial \rho}{\partial \mathbf{r}_i} \cdot \frac{\mathbf{p}_i}{m} \right] \Delta t = - \sum_j \frac{\partial}{\partial \mathbf{p}_j} \cdot (\rho \langle \Delta \mathbf{p}_j \rangle) + \frac{1}{2} \sum_{i,j} \frac{\partial^2}{\partial \mathbf{p}_i \partial \mathbf{p}_j} : (\rho \langle \Delta \mathbf{p}_i \Delta \mathbf{p}_j \rangle) \quad (2.16)$$

Now consider the average quantities $\langle \Delta \mathbf{p}_i \rangle$, $\langle \Delta \mathbf{p}_i \Delta \mathbf{p}_j \rangle$. To obtain them, we can use the

time evolution differential equation $\Delta \mathbf{p}_i = \left[\sum_{j \neq i} \mathbf{F}_{ij}^C + \mathbf{F}_{ij}^D + \mathbf{F}_{ij}^R \right] \Delta t$ which was described in

previous section.

For conservative and dissipative forces there is no contribution to $\Delta \mathbf{p}_i \Delta \mathbf{p}_j$ because it is of second order $O(\Delta t^2)$, so these two forces just appear in the first term of right hand side of equation (2.16). The contribution from the random term for $\langle \Delta \mathbf{p}_i \rangle$ is zero because the mean $\langle \zeta_{ij} \rangle = 0$, but its contribution to $\langle \Delta \mathbf{p}_i \Delta \mathbf{p}_j \rangle$ is non-zero because the variance $\langle \zeta_{ij} \zeta_{ij} \rangle = 1$. After gathering all terms, we can express equation (2.16) in the form

$$\frac{\partial \rho(\mathbf{r}, \mathbf{p}, t)}{\partial t} = (L_C + L_D + L_R) \rho(\mathbf{r}, \mathbf{p}, t), \quad (2.17)$$

where L is the evolution operator which is defined for conservative, dissipative and random parts as

$$L_C = - \sum_{i=1}^N \frac{\mathbf{p}_i}{m} \cdot \frac{\partial}{\partial \mathbf{r}_i} - \sum_{i,j \neq i}^N \mathbf{F}_{ij}^C \cdot \frac{\partial}{\partial \mathbf{p}_i}, \quad (2.18)$$

Chapter 2: Theoretical Aspects of DPD

$$L_D = \sum_{i,j \neq i}^N \mathbf{e}_{ij} \cdot \frac{\partial}{\partial \mathbf{p}_i} (\gamma w^D(r_{ij}) [\mathbf{p}_{ij} \cdot \mathbf{e}_{ij}]), \quad (2.19)$$

$$L_R = \sum_{i,j \neq i}^N \mathbf{e}_{ij} \cdot \frac{\partial}{\partial \mathbf{p}_i} \left(\frac{m^2 \sigma^2}{2} w_R^2(r_{ij}) \mathbf{e}_{ij} \cdot \left(\frac{\partial}{\partial \mathbf{p}_i} - \frac{\partial}{\partial \mathbf{p}_j} \right) \right) \quad (2.20)$$

The equation (2.17) with the defined operator L is the Fokker-Planck equation for N -particle distribution function. This equation is very similar to Kramer's equation [23], which describes the single particle evolution of mass m ,

$$\frac{\partial \rho}{\partial t} + \mathbf{v} \cdot \frac{\partial}{\partial \mathbf{r}} \rho = -\frac{\mathbf{F}(r)}{m} \cdot \frac{\partial}{\partial \mathbf{v}} \rho + \gamma \frac{\partial}{\partial \mathbf{v}} \cdot \mathbf{v} \rho + \frac{\sigma^2}{2} \frac{\partial^2}{\partial \mathbf{v}^2} \rho. \quad (2.21)$$

$$\begin{cases} \dot{\mathbf{r}} = \mathbf{v} \\ \dot{\mathbf{p}} = \mathbf{F}(r) - \gamma \mathbf{v} + \sigma \theta. \end{cases}$$

It should be noted that by omitting the random noise and friction terms, the above mentioned (2.17) Fokker-Planck equation transforms into the Liouville equation which is the corresponding equation for the conservative system. The Fokker-Planck equation of DPD not only conserves the particle number N and total momentum \mathbf{p} of the system, but also satisfies the H-theorem by the mentioned constraints, and detailed balance condition (2.7) [24], which states that a free-energy-like functional always decreases in time.

The steady state solution of equation (2.17), $\partial_t \rho(\mathbf{r}, \mathbf{p}, t) = (L_C + L_D + L_R) \rho(\mathbf{r}, \mathbf{p}, t) = 0$, gives the equilibrium distribution $\rho^{eq}(\mathbf{r}, \mathbf{p}, t)$. In statistical mechanics of Hamiltonian systems any function of the dynamical invariants (such as energy or momentum) can be an equilibrium distribution to which the system evolves provided it is ergodic or mixing [19]. The question of which equilibrium ensemble is selected is dependent on the initial condition [25]. In contrast, the equilibrium distribution of equation (2.17) is unique, and no ergodic hypothesis is required since any initial distributions will relax towards the

steady state distribution [21]. The canonical ensemble is the equilibrium solution for the conservative system, i.e. $L_C \rho(\mathbf{r}, \mathbf{p}, t) = 0$. The corresponding solution for this conservative system is the Gibbs canonical ensemble [22]:

$$\rho^{eq}(\Gamma) = \frac{1}{Z} \exp\left(-\frac{H(\Gamma)}{k_B T_0}\right) = \frac{1}{Z} \exp\left(-\frac{1}{k_B T_0} \left(\sum_i^N \frac{\mathbf{p}_i^2}{2m} + \frac{1}{2} \sum_{i,j \neq i}^N \phi(r_{ij}) \right)\right), \quad (2.22)$$

where H is the Hamiltonian of the system, $\phi(r_{ij})$ the potential function which constructs the conservative force $\mathbf{F}_{ij}^C = -\partial\phi(r_{ij})/\partial\mathbf{r}_i$, T_0 the equilibrium temperature and Z the normalizing partition function, which is defined to normalize the probability distribution function, i.e. $Z^{-1} = \int \rho(\Gamma, t) d\Gamma$. In order to satisfy the remaining parts of equation (2.17) for the equilibrium state, $(L_D + L_R)\rho(\mathbf{r}, \mathbf{p}, t) = 0$, it is necessary to have equation (2.7), as a constraint. This is a modification to the original DPD algorithm of Hoogerbrugge [18] and Koelman and is discussed in next section.

2.3 DPD H-Theorem

In the previous section we presented the Fokker-Planck equation for the DPD model. Proof of an H-theorem is the fundamental result in statistical mechanics for a dynamical system and shows that DPD particles tend to migrate towards the equilibrium state, which yields the Gibbs distribution as the equilibrium solution [22]. The equilibrium solution is not obtained by solving the Fokker-Planck equation directly, but by a natural consequence of proving the H-theorem. The H-theorem guarantees that it is stable and that all states in phase space lead to equilibrium.

Chapter 2: Theoretical Aspects of DPD

In this section we present the procedure of Marsh et al. [16], that combined the first kind Lyapounov function [23] with Boltzmann H-theorem [26]. We define a functional $F[\rho]$ of N -particle distribution function $\rho(\Gamma, t)$ by

$$F[\rho] = \int d\Gamma \rho(\Gamma, t) \{H(\Gamma) + \theta_0 \ln \rho(\Gamma, t)\}, \quad (2.23)$$

where $\theta_0 = m\sigma^2 / 2\gamma = k_B T_0$ and $H(\Gamma)$ is the Hamiltonian of the associated conservative system, defined as

$$H(\Gamma) = \sum_i^N \frac{\mathbf{p}_i^2}{2m} + E_p = \sum_i^N \frac{\mathbf{p}_i^2}{2m} + \frac{1}{2} \sum_{i,j \neq i}^N \phi(r_{ij}) \quad (2.24)$$

with E_p being the total potential energy and $\phi(r_{ij})$ the pair conservative interaction. This functional can be interpreted as a sort of free energy $F = E - \theta_0 S$, where $E = \langle H \rangle$ is the average total energy and $S = -\langle \ln(\rho) \rangle$ yields the total entropy. Of interest here is to show that F is Lyapounov function with the property $\partial F / \partial t \leq 0$, and to investigate the implications of this on the equilibrium solution of the Fokker-Planck equation. By taking the time derivative of both sides of equation (2.23) and combined with equation (2.17), one obtains

$$\frac{\partial F}{\partial t} = \int d\Gamma \{H(\Gamma) + \theta_0 \ln \rho(\Gamma, t) + \theta_0\} (L_c + L_D + L_R) \rho(\Gamma, t) \quad (2.25)$$

The last term inside the curly brackets is zero due to total probability conservation,

$$\int d\Gamma \theta_0 (L_c + L_D + L_R) \rho(\Gamma, t) = \theta_0 \frac{\partial}{\partial t} \int d\Gamma \rho(\Gamma, t) = 0 \quad (2.26)$$

Now we shall demonstrate that the whole contribution of conservative operator L_c to equation (2.25) vanishes to zero. Partial differentiation with respect to Γ yields

$$\int d\Gamma \{H(\Gamma) + \theta_0 \ln \rho\} L_c \rho = \int d\Gamma L_c (H(\Gamma) \rho + \theta_0 \rho) - \int d\Gamma \{\rho L_c H(\Gamma) + \theta_0 L_c \rho\} \quad (2.27)$$

Chapter 2: Theoretical Aspects of DPD

The term $\int d\Gamma L_c(H(\Gamma)\rho + \theta_0\rho)$ can be converted to surface integrals by divergence theorem in phase space, and so it vanishes to zero. It is apparent from classical mechanics that $L_c H(\Gamma) = 0$ while the term $\int d\Gamma L_c \rho$ consists of surface terms and also vanishes.

Therefore there is no contribution of the L_c operator and equation (2.23) becomes

$$\frac{\partial F}{\partial t} = \int d\Gamma \{H(\Gamma) + \theta_0 \ln \rho(\Gamma, t)\} (L_D + L_R) \rho(\Gamma, t) \quad (2.28)$$

Substituting equations (2.19) and (2.20) to equation (2.28), and using the partial integration within $(L_D + L_R)$, yields

$$\begin{aligned} \frac{\partial F}{\partial t} = & - \int d\Gamma \sum_{i,j \neq i}^N \left[\mathbf{e}_{ij} \cdot \frac{\partial}{\partial \mathbf{p}_i} (H(\Gamma) + \theta_0 \ln \rho(\Gamma, t)) \right] \\ & \times \left[\gamma w^D(r_{ij}) [\mathbf{p}_{ij} \cdot \mathbf{e}_{ij}] + \left(\frac{m^2 \sigma^2}{2} w_R^2(r_{ij}) \mathbf{e}_{ij} \cdot \left(\frac{\partial}{\partial \mathbf{p}_i} - \frac{\partial}{\partial \mathbf{p}_j} \right) \right) \right] \rho(\Gamma, t). \end{aligned} \quad (2.29)$$

The last result is obtained by symmetrizing the first bracket:

$$\sum_{i,j \neq i}^N \left[\mathbf{e}_{ij} \cdot \frac{\partial}{\partial \mathbf{p}_i} (H(\Gamma) + \theta_0 \ln \rho(\Gamma, t)) \right] = \frac{1}{2} \sum_{i,j \neq i}^N \left[\mathbf{e}_{ij} \cdot \left(\frac{\partial}{\partial \mathbf{p}_i} - \frac{\partial}{\partial \mathbf{p}_j} \right) (H(\Gamma) + \theta_0 \ln \rho(\Gamma, t)) \right] \quad (2.30)$$

and substituting $(\partial/\partial \mathbf{p}_i - \partial/\partial \mathbf{p}_j)H = \mathbf{p}_i - \mathbf{p}_j$ into equation (2.29) yields

$$\begin{aligned} \frac{\partial F}{\partial t} = & - \frac{\gamma}{2} \int d\Gamma \sum_{i,j \neq i}^N \left[[\mathbf{p}_{ij} \cdot \mathbf{v}_{ij}] + \theta_0 \mathbf{e}_{ij} \cdot \left(\frac{\partial}{\partial \mathbf{p}_i} - \frac{\partial}{\partial \mathbf{p}_j} \right) \ln \rho \right] \\ & \times \left[w^D(r_{ij}) [\mathbf{p}_{ij} \cdot \mathbf{e}_{ij}] + \left(m \theta_0 w_R^2(r_{ij}) \mathbf{e}_{ij} \cdot \left(\frac{\partial}{\partial \mathbf{p}_i} - \frac{\partial}{\partial \mathbf{p}_j} \right) \right) \right] \rho(\Gamma, t) \end{aligned} \quad (2.31)$$

If we now constrain the weighting functions to obey the detailed balance condition in equation (2.7), it is possible to write the time derivative of the above functional in the form

Chapter 2: Theoretical Aspects of DPD

$$\frac{\partial F}{\partial t} = -\frac{m\gamma}{2} \int d\Gamma \rho \sum_{i,j \neq i}^N w^D(r_{ij}) \left[\mathbf{e}_{ij} \cdot \mathbf{v}_{ij} + \theta_0 \mathbf{e}_{ij} \cdot \left(\frac{\partial}{\partial \mathbf{p}_i} - \frac{\partial}{\partial \mathbf{p}_j} \right) \ln \rho \right]^2 \leq 0. \quad (2.32)$$

As this form consists of a sum of negative definite terms, it is apparent that the functional $F[\rho]$ is monotonically decreasing in time. Therefore the functional will either move towards the value associated with a zero of its time derivative or will decrease in an unbounded fashion. The latter is disallowed on physical grounds [27] and so we conclude that the system will evolve until it reaches some equilibrium state $\rho = \rho^{eq}$. At this equilibrium state $\partial F / \partial t = 0$ so that

$$\left[\frac{\mathbf{p}_{ij}}{m} + \theta_0 \left(\frac{\partial}{\partial \mathbf{p}_i} - \frac{\partial}{\partial \mathbf{p}_j} \right) \right] \rho^{eq} = 0 \quad (2.33)$$

Changing variables to relative momentum of the particles, it is straight forward to prove that the equilibrium distribution of the system has the general form

$$\rho^{eq}(\Gamma) = A(\mathbf{r}_1, \dots, \mathbf{r}_N) \exp \left[-\frac{1}{2m\theta_0} \sum_i^N (\mathbf{p}_i - \mathbf{p}_0)^2 \right], \quad (2.34)$$

where \mathbf{p}_0 is a constant independent of \mathbf{r}_i and t . We will only consider macroscopic systems which are not in uniform motion over long periods and consequently the limit $\mathbf{p}_0 = 0$ is applicable.

The equilibrium probability density function $\rho^{eq}(\Gamma)$ is also the stationary solution of the Fokker-Planck equation (2.17) if $A(\mathbf{r}_1, \dots, \mathbf{r}_N)$ satisfies $L_C A = 0$. This yields the Gibbsian distribution function for the associated conservative system, i.e. equation (2.22). We assumed that $\rho^{eq}(\Gamma)$ is uniquely determined by the requirement that it satisfies equation (2.7). What this means is that the DPD system will always reach the same equilibrium state if left undriven, independent of the volume and number of particles. The

Chapter 2: Theoretical Aspects of DPD

temperature of this equilibrium state is $\theta_0 = m\sigma^2/2\gamma$, which only depends on the parameters of the model.

In the process that proves the H-theorem, the constraints that are imposed are:

$$w_D(r) = \frac{\sigma^2 m}{2\gamma\theta_0} w_R^2(r) = w_R^2(r) \quad (2.35)$$

This is called the Fluctuation-Dissipation theorem or Detailed Balance condition for the DPD method, which has exactly the same condition as the one in conventional Brownian motion. If the Langevin equation represents a Brownian particle randomly moving about in thermal equilibrium, then the dissipative reaction is related to the fluctuations of the random force [22]. In other words, a change or fluctuation in the system will be dissipated as the system returns to equilibrium.

The vital consequence of deriving the H-theorem for DPD is that the Gibbs distribution is the stationary solution of the Fokker-Planck equation. The result of this requirement in deriving H-theorem is detailed balance, and if constraints are violated, no H-theorem can be derived and the Gibbs distribution is not a stationary solution of the Fokker-Planck equation for DPD.

Chapter 3

Boundary Models in DPD

3.1 Introduction

Dissipative particle dynamics (DPD) is an extremely effective mesoscopic simulation technique, especially due to low computational cost, in studying the hydrodynamic behavior of a complex field of fluid. Most studies, which use the DPD technique, simulate part of an infinite region using a system confined by periodic boundaries. These kinds of boundaries are capable of modeling macroscopic properties of the bulk flow very well, but difficulties arise if the flows are confined through wall-bounded regions, or when different boundaries simultaneously exist in the simulation domain. The desired behavior of solid wall, and hence the boundary conditions, depends on the point of view to the system and the scale at which a system is investigated. On an atomic level it is likely that a wall induces structure in the field, as well as locking and slip, influencing the properties in the order of nanometers from the boundary [28-31]. Nevertheless, when DPD is employed as a particle-based flow solver at a mesoscopic level of micrometers, the degree of coarse graining is too high to show such atomistic effects near the wall [32]. So construction of the solid wall models in this higher level of coarse graining is still a dilemma and no general mechanism is widely accepted for this mesoscopic level.

In this chapter, we first study different methods used in the literature to handle boundary conditions in confined geometries. Later in Chapter 5 we recognize some of their diagnostics and subsequently introduce a new method utilizing a kind of bounce back reflection which we call the “bounce-normal” reflection. The most important characteristic of this method is that it reduces density fluctuations near the boundaries without affecting the velocity and temperature profiles. This new method is easily applicable to any wall bounded problem with stationary boundaries and it has a very good consistency to macroscopic features. The simulation results of this bounce normal reflection are presented in Chapter 5.

3.2 DPD Boundary Conditions

Defining the correct boundary conditions, especially at solid boundaries, is one of the main issues for DPD simulation in wall-bounded geometries. For DPD, we can also employ the general implementation of boundary conditions that have been used in the lattice Boltzmann method (LBM) and molecular dynamics (MD) formulations. However, unlike the MD method, the soft repulsion between the DPD particles can not prevent fluid particles penetrating solid boundaries, and so we need appropriate mechanisms at the walls to prevent this penetration. We call the boundary well defined if the following main characteristics are observed, and these are the macroscopic properties which should not be violated by imposition of boundaries:

no-slip; the wall should impose the correct velocity profile through the whole flow field and also at the boundaries

impenetrability; no particles are allowed to enter the wall

Chapter 3: Boundary Models in DPD

consistency to macroscopic system properties; the temperature and density profiles should obey the thermal and continuum limits, specially near the boundaries

To maintain the above properties, we can generally classified the models of boundary conditions in DPD methods, similar to [33], as follows:

The Periodic boundary conditions

The Lees-Edward boundary conditions

Freezing particles in boundary regions to create a rigid body or rigid wall.

Reflecting particles with different reflection mechanisms combined with different types of particle layers.

3.3 The Periodic Boundary Conditions

In order to simulate the behavior of a bulk region, an infinite system, or to provide complete boundaries to minimize the surface effects, the periodic boundary condition is usually adopted [34, 35]. The central cubic box which contains N particles is replicated throughout space to form an infinite lattice. As a particle moves in the central cell, its periodic image in each of the neighboring boxes moves in exactly the same way. When a particle enters or leaves through one face of a cell, one of its images will enter or leave through the opposite face. Thus the total number of particles in the main cell, and hence in the entire system, is conserved. The two-dimensional sketch of such a periodic system is shown in Figure 3.1. In this figure the duplicated boxes are labeled A, B, C, etc., and the schematic movement of particle 1 and its images 1_A , 1_B , etc. are shown across their corresponding boundaries.

Chapter 3: Boundary Models in DPD

In order to handle the simulation it is not necessary to store the coordinates of all the images. Let us assume all the coordinates in the central box (with the edge dimension L), lie in the range $(-L/2, L/2)$; i.e. the coordinate system is at the center of the main cell. The following procedure is sufficient to adjust the periodic condition when the particle crosses the boundary

$$\begin{cases} r_i^x = r_i^x - L_x \left[\frac{r_i^x}{L_x} \right] \\ r_i^y = r_i^y - L_y \left[\frac{r_i^y}{L_y} \right] \\ r_i^z = r_i^z - L_z \left[\frac{r_i^z}{L_z} \right] \end{cases} \quad (3.1)$$

and after calculating a pair separation vector, the following statements should be applied to produce a correct neighboring distance

$$\begin{cases} r_{ij}^x = r_{ij}^x - L_x \left[\frac{r_{ij}^x}{L_x} \right] \\ r_{ij}^y = r_{ij}^y - L_y \left[\frac{r_{ij}^y}{L_y} \right] \\ r_{ij}^z = r_{ij}^z - L_z \left[\frac{r_{ij}^z}{L_z} \right] \end{cases} \quad (3.2)$$

where L_j is the j box dimension and $[Y]$ returns the nearest integer to Y ; thus

$[-0.49] = 0.0$, whereas $[-0.51] = -1.0$.

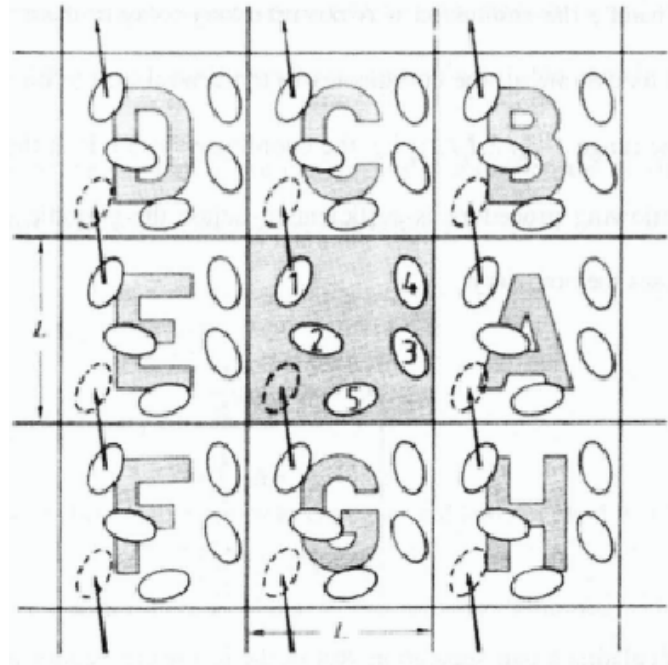


Figure 3.1 A two-dimensional periodic system. Particles can enter and leave each box across each of the four edges. In a three-dimensional case, particles would be free to cross any of the six cube faces [35].

Due to its geometrical simplicity, the most commonly used cells are cubic boxes, though other different shapes have been employed in related applications [36, 37]. In general, the use of periodic boundary condition restricts the simulation technique to studies of short-range and short-lived phenomena [38]. For equilibrium properties particularly thermodynamics and local structure, the effects of this boundary condition are negligible. However, the use of periodic boundary conditions inhibits the occurrence of long wavelength fluctuations. Another difficulty is the so-called quasi-ergodic problem [39] for small sample, which means the system can possibly be trapped in a small region of phase space.

3.4 The Lees-Edward Boundary Conditions

There are two versions of Lees-Edward boundary conditions. In the original method, Lees and Edward [40] proposed the boundary conditions for non-equilibrium molecular

Chapter 3: Boundary Models in DPD

dynamics simulation, which retain periodicity but alter the position and velocity of the periodic images. Here we provide its description according to [35]. The infinite periodic system is subjected to a uniform shear in the x - y plane. The simulation boxes and its images centered at $(x, y) = (\pm L, 0), (\pm 2L, 0)$, etc. are taken to be stationary. The boxes in the above layer are moving at a speed $\delta v_x = (dV_x / dr_y) L$ in the positive x direction, while the below layer move with the same speed but in the opposite direction, here the (dV_x / dr_y) is the imposed shear rate. A particle crossing the upper boundary of the box at time t is returned through the lower boundary with its x -coordinate shifted by $\delta v_x t$ and the x -velocity decreased by δv_x . This is also applied for the particle crossing the lower boundary but with the opposite signs. In Figure 3.2 the two-dimensional version of such replacements is shown. We can describe the algorithm for a particle that crosses the boundaries by defining $\Delta_y = [r_i^y / L_y]$,

$$\begin{cases} r_i^x = r_i^x - \delta v_x \Delta_y \\ r_i^x = r_i^x - L_x [\frac{r_i^x}{L_x}] \\ r_i^y = r_i^y - L_y \Delta_y \\ r_i^z = r_i^z - L_z [\frac{r_i^z}{L_z}] \\ v_i^x = v_i^x - \delta v_x \Delta_y \end{cases} \quad (3.3)$$

and we should update the calculated pair separations by

$$\begin{cases} r_{ij}^x = r_{ij}^x - \delta v_x \Delta_y \\ r_{ij}^x = r_{ij}^x - L_x [\frac{r_{ij}^x}{L_x}] \\ r_{ij}^y = r_{ij}^y - L_y \Delta_y \\ r_{ij}^z = r_{ij}^z - L_z [\frac{r_{ij}^z}{L_z}] \end{cases} \quad (3.4)$$

Chapter 3: Boundary Models in DPD

where $\Delta_y = [r_{ij}^y / L_y]$. In all of the above equations, the δr_x is the relative displacement of the upper layer to the central box, i.e. $\delta r_x = \delta v_x t$.

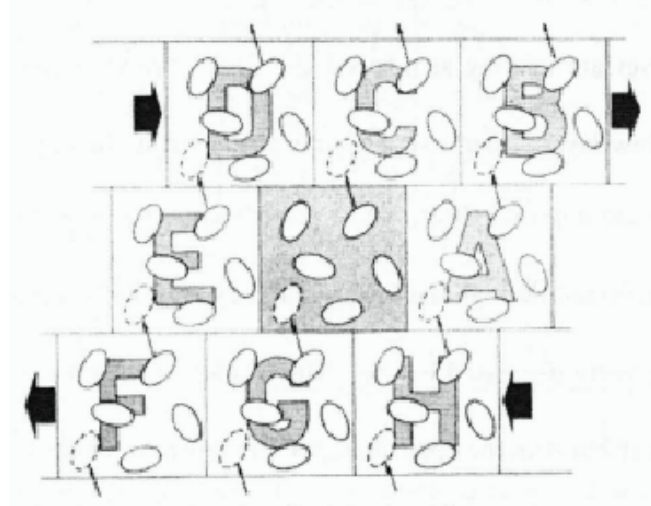


Figure 3.2 Homogeneous shear boundary conditions (Lees-Edward method) [35].

An important advantage of the original Lees-Edward method is the production of shear flow with the constant shear rate, which enables one to measure the viscosity of simulated flow due to the chosen technique. For example, the viscosity of a DPD model of a colloidal suspension was studied using this approach [7, 41]. This could be done by calculating and comparing the shear stress of the simulated fluid to the theoretical value. Another similar method was introduced by Backer et al. [42], which is based on using periodic boundary conditions to simulate counter-flowing Poiseuille flows without use of explicit boundaries. In this method a rectangular domain is doubled in size in the cross-flow x direction and the flow is sustained by applying the body force (in the y direction) to each particle, with the direction of the force being opposite in the two halves of the domains. This is schematically shown in Figure 3.3.

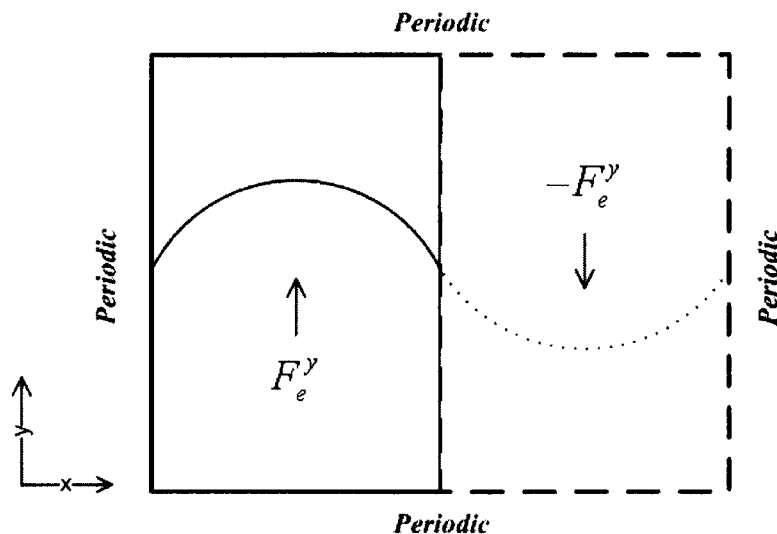


Figure 3.3 Schematic sketch of periodic Poiseuille flow method (a new kind of Lees-Edwards boundary conditions).

This periodic Poiseuille flow method is very useful to measure the viscosity of particle simulations, since it does not have the density artifacts and produces a flow with uniform density from wall-to-wall apart from the statistical fluctuations. Unlike the original Lees-Edward method, shear stress measurements are not required in this Poiseuille flow method and the system average of the velocity or the maximum in the flow direction directly provides the viscosity of the fluid.

3.5 Freezing and Reflecting Boundary Conditions

In the classification which we made in section 3.2 the third and the fourth categories are somehow broad and there are different published implementations of these methods. We review in some more detail the most representative works published so far that fall under categories (3) and (4). Freezing the particles inside the solid regions is one of the most important and applicable cases which have been combined with other different

Chapter 3: Boundary Models in DPD

reflections. Our new proposed method in Chapter 5 also employs frozen particle-layers as well as reflections.

The DPD particles are frozen in different patterns according to the system geometry and rheological complexity in order to create the solid or particulate boundaries. One way to do this is to put particles in structured lattices with layers of FCC lattice or regular lattice [43-47]. Another alternative is to distribute particles inside the boundary randomly [7, 41, 48-50]. The act of freezing in the latter case will be carried out after reaching the equilibrium state or particles could spread out initially due to uniform random distribution.

In [51] a layer of DPD particles is stuck on the boundary and by taking the continuum limit of this layer, and dissipative and stochastic forces on the fluid DPD particles are obtained analytically. However, reflections were found necessary to prevent wall penetration since the effective computed forces are not sufficient and particles should be reflected back to the fluid domain. A similar method to Revenga et al. [51] (getting effective forces for planar geometries), but for cylindrical and spherical geometries, was used by Colmenares and Rouse [52] in order to obtain explicit expressions for the effective random and dissipative forces for a point DPD particle. They found the dissipative and stochastic forces of a particle i with velocity \mathbf{v}_i located at \mathbf{r}_i from a given surface having a velocity \mathbf{V} by defining the matrix \mathbf{M} and the vector \mathbf{N} as

$$\begin{cases} \mathbf{F}_i^D = \mathbf{M}(r_i) \cdot (\mathbf{v}_i - \mathbf{V}), \\ \mathbf{F}_i^R = \mathbf{N}(r_i) \theta \end{cases} \quad (3.5)$$

and

$$\begin{cases} \mathbf{M}(r_i) = -\gamma \rho_w \int_s d\mathbf{r} w(|\mathbf{r} - \mathbf{r}_i|)^2 \mathbf{R}\mathbf{R}, \\ \mathbf{N}(r_i) = \sigma \rho_w \int_s d\mathbf{r} w(|\mathbf{r} - \mathbf{r}_i|) \mathbf{R} \end{cases} \quad (3.6)$$

where ρ_w is the wall density, $\mathbf{R} = \mathbf{r} - \mathbf{r}_i / |\mathbf{r} - \mathbf{r}_i|$ is a unity vector and \mathbf{r} is the distance from particle i to particles stuck on the surface.

In [33] the effect of different reflections (specular, Maxwellian and bounce back reflections) was investigated. In specular reflections the velocity component tangential to the wall does not change while the normal component is reversed. In bounce-back reflection both components are reversed. In Maxwellian reflection particles are introduced back to the flow with a velocity following a Maxwellian distribution which is centered around the velocity of the boundary. In [33] a crucial dimensionless parameter τ (friction coefficient), was identified that affects the wall slip velocity,

$$\tau = \frac{\gamma \lambda}{V_T d}, \quad (3.7)$$

where γ is the friction coefficient, λ the average distance between particles ($\lambda = \rho^{-\frac{1}{d}}$), d the spatial dimension and $V_T = \sqrt{k_B T / m}$ the thermal velocity scale. Large values of τ mean that the particles move very little in the time scale associated with the velocity decaying due to thermal fluctuations. In [33] the Couette flow was examined to measure the slip ratio due to different reflections and it was shown that for large values of τ all three reflection mechanisms result in an appropriate stick boundary condition. However for small values of τ , the specular and Maxwellian reflections produce excessive slip velocity at the wall while the bounce-back method still satisfies the no slip condition but it (bounce-back) shows an anomalous temperature behavior. This behavior is due to the fact that for small τ the interaction between fluid particles is small. Furthermore when $\tau = 0$, the DPD particles move in straight lines and the bounce-back boundary condition accelerates the particles without bound in each collision with the wall. The dispersion of the tangential component of the velocity therefore, increases without bound. At small but

Chapter 3: Boundary Models in DPD

finite τ the friction saturates this dispersion to a finite value. The main problem with the approaches in [33, 51] is that the computation of the force is just carried out for dissipative and random terms. However the more difficult case where the conservative forces are present was not considered. The conservative force is an important term which may result in large density fluctuations at the wall.

Kong et al. [53] studied the dynamics of a DPD polymer in a solution between two walls (without shear). Wall particles were kept in a “frozen” state, so that they do not move relative to each other. (This is an analogous procedure to that used to model dispersions). The density of the wall had to be chosen to be four times larger than that of the solution to achieve an impenetrable wall. This high density subsequently induces a depletion zone in the solution adjacent to the wall. Although such a depletion layer and further ordering phenomena are to be expected at the atomistic level, they must be seen as model artifacts in a coarse-grained model. A similar non-desired effect of the model is seen in the simulation of Jones et al. [54], who simulated the shearing of a liquid drop on a solid surface. They used the same density for the solid and liquid but added a strong repulsive interaction between both phases to keep them separated. Again, this leads to density distortions in the liquid. These distortions will be examined and removed in our new method that will be introduced later. Moreover, the flow profile shows the occurrence of large slip. Jones et al. [54] attempted to solve this problem by imposing a certain velocity on all particles within a close distance from the wall.

The problems mentioned above concerning density distortions and slip flow only play a role near the surface. If one is solely interested in the behavior of the system far away from any interfaces, these issues do not pose a problem. However, in many applications one is dealing with systems where the effect of surfaces cannot be neglected, for

example, in lubrication. In such confined geometries the conventional DPD method will easily give rise to unwanted artifacts.

Willemsen et al. [55] proposed a scheme to obtain a no-slip boundary condition in DPD without using high wall densities. Below we give a brief description of this algorithm. More details can be found in [55]. An extra particle-layer is included outside of the domain with the objective of constructing a correct velocity profile that continues beyond the wall boundary. These walls are assumed to be made up of “virtual” particles. The interactions between the real fluid particles (which can be either solvent particles or polymer segments) and these wall particles are determined by the same equations that describe the forces between two fluid particles. However, the positions and velocities of the wall particles are not updated using the time integrating Verlet or a similar algorithm. The positions and the velocities of particles inside the wall layer are determined from the layer of DPD particles adjacent to the boundary and within a distance r_c (the cutoff radius). At the beginning of each time step they are determined in such a way as to ensure a smooth distribution of fluid particles near the walls together with no-slip conditions. For each fluid particle whose distance to the wall is smaller than r_c , a wall particle is placed at the same distance from the boundary layer. The y and z components of the wall particle are determined by adding a random shift taken from the interval $(-r_c, r_c)$ to the position of the original fluid particle. The normal (x) and the z velocity components of the wall particle have the same magnitude as those of the original fluid particle, but the sign of these components is opposite to that of the fluid particle. The y -velocity component of the wall particle is taken as the average of the y -velocity component of the fluid particle and the wall velocity. This procedure ensures that there is a linear velocity profile across the wall boundary. The random and drag

Chapter 3: Boundary Models in DPD

forces exerted by the wall on nearby fluid particles (those at a distance smaller than r_c) are calculated by summing over all pair interactions between fluid and wall particles. This approach works very well in the absence of conservative forces but when conservative forces are applied density oscillations occur. The conservative forces are calculated from a different set of wall particle positions, as the interactions between the fluid particles directly adjacent to the wall and their own mirror images lead to an excessively large repulsion. Therefore, a second layer of DPD particles was created by shifting all fluid particles at a distance between r_c and $2r_c$ into the wall layer. These wall particles are then used to calculate the conservative force exerted by the wall on the fluid. It seems that the method of [55] is quite effective but it may not be easily implemented in complex-geometry flows, e.g. flow around a cube, as it is not clear how such “ghost” particle-layers can be constructed in such situations [45].

In order to study the effects of the conservative force on the density fluctuations, we calculated the effective force on a point particle. We assume the point particle is located at the centre line normal to the flat plane on which the wall particles are laid out. We assume continuum limit of wall particles and estimate the total repulsive force which is exerted by the wall to the point fluid particle. In Figure 3.4 the total force with different layer distance to the wall is shown. As we increase the layer distance the total effective force is decreased, whereas the force near the wall is increased. Also, in Figure 3.5, we assume two layers of particles where one of them is located exactly at the wall and the other one is shifted by different distances. Note that all of the estimated repulsive forces are normalized with respect to density and the repulsion parameter.

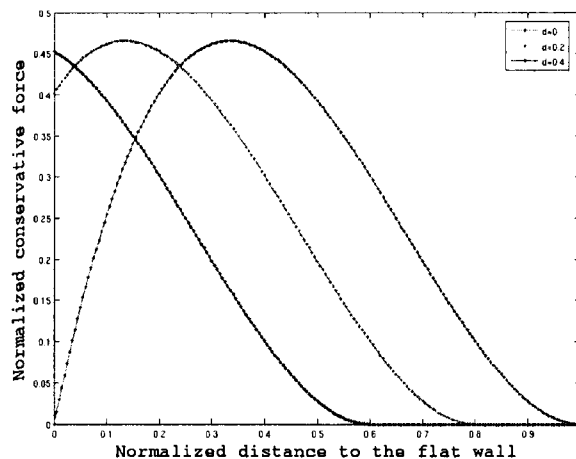


Figure 3.4 Total force exerted by wall particles to a point that moves on the center line of the flat wall.

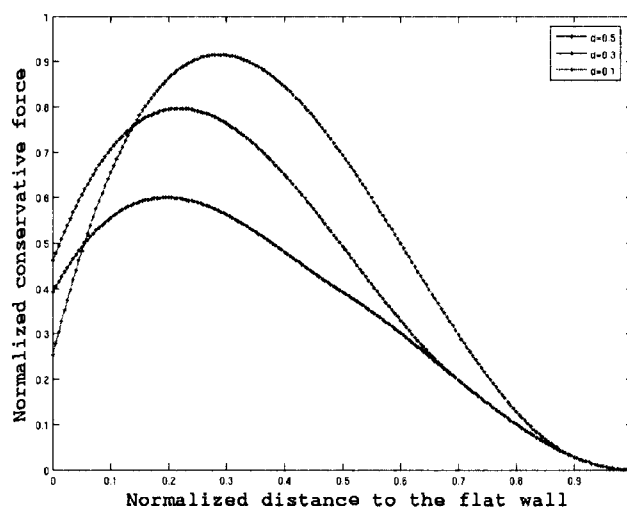


Figure 3.5 Total force exerted by two-layer wall particles to a point that moves on the center line of the flat wall.

These different profiles may lead to undesirable density oscillations near the wall regions. We can reduce these density oscillations by controlling the repulsion parameter and using different wall patterns with different densities. However it is not easy to obtain both no slip condition and zero oscillation. Effects of some of these parameters are examined more numerically and in real simulation in the Chapter 5.

Chapter 3: Boundary Models in DPD

Darias et al. [56] reported the flow of a biphasic (suspension) fluid through a cylinder under a pressure gradient. They found the expected Poiseuille velocity profile as well as packed structure density profiles near the wall as the result of the discrete nature of the formulation. This edge effect is important for distances of the order of the effective interaction range and is of no consequence to bulk properties.

More recently, Visser et al. [32] described a method to create impenetrable flat and cylindrical solid walls with no effect on the fluid properties such as the density profile. They introduced a new wall construction method that makes use of parallel twin systems which set up the wall by a back-to-back placement. This automatically generates a smooth particle and velocity distribution across the wall boundary as well as corrects interparticle correlations. Hence, they simulated a wall that meets the no-slip boundary condition without affecting the properties of the system. To make their new wall method applicable to curved boundaries, they developed a folding and scaling procedure to connect curved systems with their periodic image or the image of a parallel system. This allows one to model curved walls as well. A bounce-back reflection ensures the walls impenetrability, but it may introduce side effects. If the tangential displacement to the wall is left unaltered for particles that are reintroduced, the bounce-back method transforms into a bounce-forward method that shows the same no-slip but lacks these side effects. Both reflection methods leave the thermodynamics of the system intact when the direction of the acceleration of a particle is changed after a reflection. The new boundary method meets all requirements for solid walls at higher densities, but shows some velocity slip at low densities for non-ideal systems [32].

One of the most applicable methods of reflection, similar to Maxwellian reflection, was first introduced by Fan et al. [43] as a boundary condition, and was used in several other

Chapter 3: Boundary Models in DPD

publications for modeling flow in channels [47-50, 57, 58]. In this method frozen particles are used to represent the wall and in addition there is a thin layer of DPD particles near the wall where the no-slip boundary condition is obtainable. A random velocity distribution is enforced in this layer with zero mean corresponding to a given temperature and the velocity distribution induced by the movement of the boundary. When the particle is injected to this layer, it will leave with the corresponding velocity

$$\mathbf{v} = \mathbf{v}_R + \mathbf{n}(|\mathbf{n} \cdot \mathbf{v}_R| - \mathbf{n} \cdot \mathbf{v}_R) + \mathbf{V}_{wall}, \quad (3.8)$$

where \mathbf{v}_R is the random vector and \mathbf{n} is the unit vector normal to the wall and pointing towards the fluid and \mathbf{V}_{wall} is the wall velocity. The thickness of this layer and the strength of the repulsion between wall and fluid particles in this method are chosen to minimize the velocity and density distortion, and the authors of [43] recommended this to be minimum between 0.5% of channel width and $0.5r_c$ (half of cutoff radius). A thin layer is necessary to prevent the frozen wall from cooling down the fluid. However, significant density distortions and small levels of temperature drop near the wall boundaries are present in this method, which are undesirable.

Chapter 4

DPD Simulation Methods and Parameters

In this chapter first we examine the standard methods for decreasing the computational cost in DPD simulations for usual serial programming implementation. Then we study the effective time integration methods for the DPD algorithm. Finally we take a brief look at some of the important DPD parameters and also we introduce a simple uniform random number generator.

4.1 Neighbor List Method and Linear Scaling

The major computational cost for DPD algorithm is calculating the total DPD interactions in each time step. In DPD simulation, evaluation of inter particle distances and their relative forces account for most of the CPU time. The direct calculation of these interactions requires N^2 steps, where N is total number of particles. If we note the symmetry of pair interactions, i.e. $F_{ij} = F_{ji}$, the total calculation steps can be decreased to $N(N-1)/2$. Obviously it is very expensive to carry out such intensive calculations when the number of particles is large, and some methods to reduce the redundant computation related to evaluation of separation distances are essential. As DPD particles only interact with other particles less than a cutoff radius r_c away, the time for calculating DPD interactions offers the potential for linear scaling with N .

Chapter 4: DPD Simulation Methods and Parameters

The general way to reduce the number of interactions is to use a cutoff distance r_c , where all forces beyond the cutoff distance are zero. This treatment reduces the computing time significantly by neglecting all particles beyond the cutoff distance, since interactions between these particles are minimal and need not be considered. Thus, if each DPD particle interacts with N_{r_c} other particles (i.e., the number of particles within a distance r_c of a typical DPD particle is N_{r_c}), then the computation time for calculating DPD interactions scales as

$$t_F = O(N \times \frac{N_{r_c}}{2}). \quad (4.1)$$

A straightforward way to determine which particles are within cutoff distance is to evaluate all distances over all particles pairs, and this procedure would require $N(N-1)/2$ steps. A reduction of redundant calculation of interparticle distances can be accomplished by the conventional Verlet table algorithm and cell-linked list algorithm. The basic idea of Verlet table method is to construct and maintain a list of neighboring particles for every particle in the system. During the simulation, this neighbor list will be updated periodically for a fixed interval or reconstruct itself automatically when some particles move too much and the list becomes out-of-date. During the interval of neighbor list updating, each atom is assumed to interact only with those in its neighbor list. Of course constructing of the Verlet table requires $N(N-1)/2$ times of inter particle distance evaluation. The Verlet table method has been proven to be efficient when a system contains a relatively small number of particles and the particles move slowly (this may be effective for less than thousand particles [35]). However, the main drawback is that as the number of particles increases, the memory requirement for maintaining the neighbor lists becomes excessive, and the time to construct a Verlet table increases as the

Chapter 4: DPD Simulation Methods and Parameters

order $O(N^2)$. Moreover, as the particles move more quickly, either the “skin” (largest distance allowable of an atom that keeps it in the neighbor list) must be increased, or the frequency of reconstructing Verlet table must be increased. Both of these requirements make the CPU time required to maintain the Verlet table increase dramatically, and the whole simulation becomes inefficient.

The resolution to this difficulty is to eliminate the need to calculate the distance between every pair of particle at each time step. We accomplish this goal by dividing the periodic cell of our DPD simulations into subdomains. The cell-linked list algorithm [35] (neighbor-list method [59]) which is an effective method to reduce the calculation of pair distances is employed. This approach partitions the simulation domain into small cells and each particle is assigned to these cells by their coordinates. Since the neighborhood cells of each cell is known and will not change during the simulation, and the lengths of the three edges (for three-dimensional simulation domain) of the cells can be selected to be equal to r_c , then neighborhood particles of an atom can be listed by enumerating all atoms in all neighborhood cells and the cell itself. The implementation of a cell-linked list algorithm is usually to first construct a cell neighbor list table, and then assign each particle to the cells before calculating DPD interactions. This process requires little CPU time and needs to be carried out only once. If the number of subdomains is N_{sub} , then the time t_{dist} to calculate the required separation between particles is reduced from $N(N-1)/2$ to

$$t_{dist} = O\left(\frac{N^2}{2N_{sub}}\right). \quad (4.2)$$

For large enough values of N_{sub} , the reduction in t_{dist} is sufficient to render t_F the dominant contributor to computation time, $t_F \gg t_{dist}$, and linear scaling with the total

Chapter 4: DPD Simulation Methods and Parameters

number of particles is achieved. This is somewhat similar to the fast multipole method of Greengard and Rokhlin [60], which greatly accelerates the calculation of multipole interactions between particles.

Let us consider the three-dimensional periodic box, whose dimension is $L \times L \times L$. The number of subdomains with the defined r_c is

$$N_{sub} = \frac{L^3}{r_c^3} = \frac{N}{\rho r_c^3}, \quad (4.3)$$

where ρ is the average number density of the whole particles. By substitution of equation (4.3) into equation (4.2) we obtain

$$t_{dist} = O\left(\frac{\rho r_c^3 N}{2}\right). \quad (4.4)$$

This equation shows the linear dependency of time with respect to the total number of particles. Another important consequence of equation (4.4) is the cubic dependence of time to the cutoff radius, for instance if we increase the cutoff radius by 25% the computational cost will double. This shows the efficiency of link-list neighbor algorithm for short range interactions.

We assigned to each of these subdomains an identification number (ID) from 0 to $N_{sub} - 1$. Up to 26 neighboring subdomains are attached to each subdomain, only if the IDs of the neighboring subdomains are smaller than the ID of the subdomain. This is to avoid calculating the same interaction twice. Every subdomain may have 0 to 26 neighboring subdomains.

In order to examine the computational cost we choose the fixed number of 40,000 time steps, and measure the CPU time for different number of particles, similar to the work of Kim [61]. The tests are run on a PC Intel Pentium IV 3,000 MHz CPU with SUSE

Chapter 4: DPD Simulation Methods and Parameters

Linux 10.0 operating system. The comparison of results for two algorithms are shown in Figure 4.1, where linear scaling and computational cost improvement of the neighbor-list method is significantly better compared to the Verlet-table algorithm.

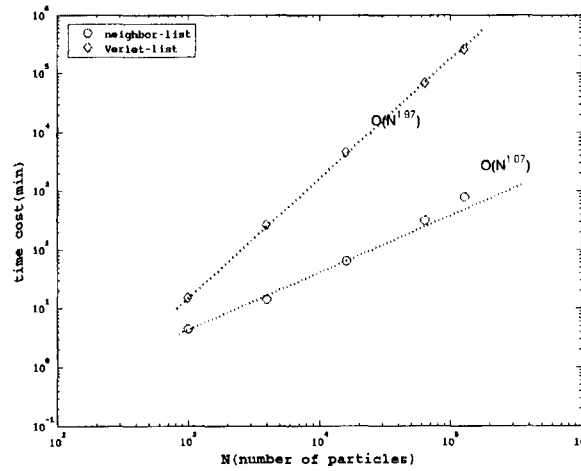


Figure 4.1 Plot of computational cost (time in minutes), comparison between the neighbor-list and Verlet-list methods.

It is obvious from the Figure 4.1 that for small number of particles it is not efficient to use the neighbor-list method. This is because of the tradeoff between overheads for maintaining the neighbor-list table and reduction of calculation of unnecessary inter-particle distance. The current scheme of saving computational time can be compared to the work of Boryczko et al. [61, 62], who devised an algorithm that divides the simulation domain into several subdomains in order to use it for parallel algorithm capable of using multiple processes. This kind of subdomain approach is also helpful in limiting communication requirements in our future parallel implementation of the DPD.

4.2 Numerical Time Integration Schemes

Unlike MD (molecular dynamics), the DPD equations are stochastic, and this represents an extra degree of difficulty. In addition, the dissipative force depends on the velocity,

Chapter 4: DPD Simulation Methods and Parameters

which in turn depends on the force, so there is nonlinear coupling. In this section we introduce the simple Euler and velocity-Verlet algorithms that have been typically used to integrate the DPD equations. Various other finite time-step implementations of DPD have been suggested, which will follow the phase space path of the particles more accurately and therefore better represent the stochastic differential equations. Such algorithms are often based on analogies to higher-order solvers for conservative systems, such as the Verlet or leap-frog algorithms and would be expected to follow the evolution up to the second-order in the time-step. However, care must be taken in the implementation to take account of the stochastic nature of the underlying equations, and an analysis of these methods for DPD can be found in [63]. Recently there are also other complex integration schemes such as the Shardlow's splitting Method [64], Lowe's approach [65], self consistent Verlet [66], etc., which a detailed comparison of the performance of these integrators is given in [67].

The simple explicit Euler-type integrator is used not frequently but it helps to set the notation for the more complicated algorithms and also as starter for multistep integrators of higher-order. It is assumed that we know the solution at time t and wish to obtain the solution at time $t + dt$. Both the velocities and the positions of all particles are updated in a straightforward manner as

$$\begin{aligned}\mathbf{r}_i^{t+dt} &= \mathbf{r}_i^t + dt \mathbf{v}_i^t \\ \mathbf{v}_i^{t+dt} &= \mathbf{v}_i^t + dt \mathbf{f}_i^t \\ \mathbf{f}_i^{t+dt} &= \mathbf{f}_i(\mathbf{r}_i^{t+dt}, \mathbf{v}_i^{t+dt})\end{aligned}\tag{4.5}$$

For the DPD system we do not expect the system to blow-up because of the thermostating nature of the dissipative and random forces. However we should note the random force $\mathbf{F}_{ij}^R = \sigma w^R(r_{ij}) \zeta_{ij} dt^{-1/2} \mathbf{e}_{ij}$ and the appearance of $dt^{-1/2}$ as discussed in more detail in [6].

Chapter 4: DPD Simulation Methods and Parameters

The velocity-Verlet algorithm is based on the classical MD velocity-Verlet method [35, 38], but we use a modified version of this method for calculating the evolution of DPD particles

$$\begin{aligned}
 \mathbf{r}_i^{t+dt} &= \mathbf{r}_i^t + dt \mathbf{v}_i^t + \frac{1}{2} dt^2 \mathbf{f}_i^t \\
 \tilde{\mathbf{v}}_i^{t+dt} &= \mathbf{v}_i^t + \lambda dt \mathbf{f}_i^t \\
 \mathbf{f}_i^{t+dt} &= \mathbf{f}_i(\mathbf{r}_i^{t+dt}, \tilde{\mathbf{v}}_i^{t+dt}) \\
 \mathbf{v}_i^{t+dt} &= \mathbf{v}_i^t + \frac{1}{2} dt (\mathbf{f}_i^t + \mathbf{f}_i^{t+dt}).
 \end{aligned} \tag{4.6}$$

If the forces were independent of velocity (like in MD), the actual velocity-Verlet algorithm would be recovered for $\lambda = 1/2$. As the force does depend on velocity, we make a prediction for the new velocity, which we denote by $\tilde{\mathbf{v}}$, and correct for this afterwards in the last step. In this more sophisticated algorithm, the force is updated once per iteration (after the second step) and is thus unlike the self-consistence method of Pagonabarraga et al. [66]. Also, there is virtually no increase in computational cost. If there were no random or dissipative force, this algorithm would scale exactly to $O(dt^2)$ with $\lambda = 1/2$. Due to the stochastic nature of process, the order of the algorithm becomes unclear [6]. The variable factor λ , introduced empirically, appears to account for some of the additional effects of the stochastic interactions.

In this section we employ the simple Euler and velocity-Verlet algorithms, and we compare these methods and determine appropriate values of the parameter λ for future applications. The simulation is conducted in a 3D fully periodic box of size $10 \times 10 \times 10$, where the length scale is defined by $r_c = 1$. The particle number density is chosen $\rho = 3$ (i.e. total number of particles is $N = 3,000$). The random force strength is set to $\sigma = 3$, and the dissipative force amplitude becomes $\gamma = 4.5$ if we choose the unit of energy as

Chapter 4: DPD Simulation Methods and Parameters

$k_B T = 1$. Also the repulsion parameter set to $a = 25$. The measured physical quantity in these simulations is the average kinetic temperature defined by assuming unit mass for all particles as

$$\langle k_B T \rangle = \frac{1}{3N-1} \left\langle \sum_{i=1}^N \mathbf{v}_i^2 \right\rangle. \quad (4.7)$$

We run the simulations for the total time of $t = 400$ and obtain the average temperature after equilibrium or after time passes around $t = 40$. Initially the particles are distributed randomly at rest. Figure 4.2 shows the effect of timestep size on temperature for the three methods. It is observed that by increasing the timestep size the amount of artificial rise in temperature correspondingly increases. The optimum λ parameter for the Verlet method is obtained after several runs. We see negligible temperature rises for the Verlet algorithm with timestep sizes smaller than $dt < 0.04$, where for the simple Verlet method ($\lambda = 0.5$) the error is less than 3%, and for the optimum Verlet ($\lambda = 0.65$) method the rise is less than 0.8 %. However in the Euler algorithm with stepsize of $dt \approx 0.01$ there is more than 40% of artificial temperature increase. Thus for all subsequent simulations, we select the optimum Verlet algorithm with arbitrary time-step sizes of $dt < 0.04$.

Chapter 4: DPD Simulation Methods and Parameters

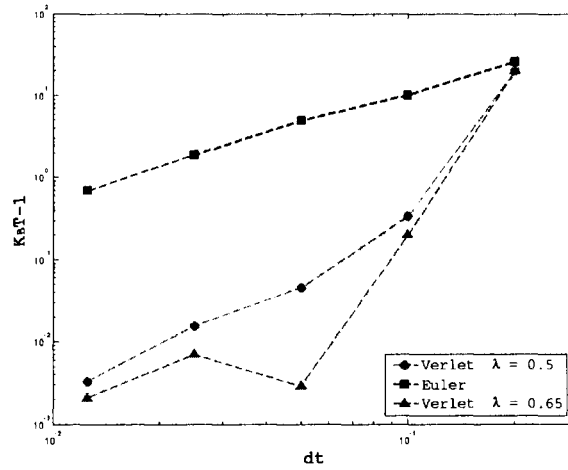


Figure 4.2 Temperature deviations versus size of time step for Euler method, simple Verlet method and Verlet method with optimum λ parameter.

4.3 The Noise Amplitude and Maxwellian Distribution

First we investigate the effects of finite time step on the equilibrium distribution function as the other criterion for the accuracy of numerical results. The DPD parameters are set similar to the previous section. For time integration we use the optimum Verlet algorithm with three different time-step sizes. The distribution is calculated after reaching the full equilibrium state. The theoretical DPD equilibrium distribution which is similar to the Maxwell-Boltzmann distribution is given by

$$f(\mathbf{v}_x) = \left(\frac{m}{2\pi k_B T}\right)^{1/2} \exp\left(\frac{-m\mathbf{v}_x^2}{2k_B T}\right). \quad (4.8)$$

In Figure 4.3 the comparison between theoretical values of the probability distribution against numerical results is shown. The results show that even up to time-step size of $dt = 0.06$ the equilibrium distribution function does not vary significantly from the Maxwell-Boltzmann distribution. Therefore the use of optimum Verlet algorithm with time step sizes of $dt < 0.04$ is again acceptable, and we see that it has very comparable numerical outcomes with optimum computational cost.

Chapter 4: DPD Simulation Methods and Parameters

Another important parameter in DPD simulation is the noise amplitude which also determines the friction coefficient according to the detailed balance condition. These two factors are chosen to yield an efficient and numerically stable DPD simulation. Here we demonstrate the effects of this random coefficient and adjust the appropriate value for it. When the noise amplitude is increased, the time-step range over which the system is stable does not change by much, but the speed at which the system reacts due to temperature variations is increased [6]. This leads to efficient temperature equilibration. However the upper limit is determined by the time integration scheme, time-step and the equilibrium temperature. Some of these effects are shown in Figure 4.4 where the simulations are run using the Verlet algorithm with $dt = 0.04$ for the unit equilibrium temperature. After several investigations for different values of equilibrium temperature, $k_B T$, we came into conclusion that in order to obtain a fast and stable simulation the appropriate random coefficient should be a number below 4.5 for the minimum temperature of 0.1.

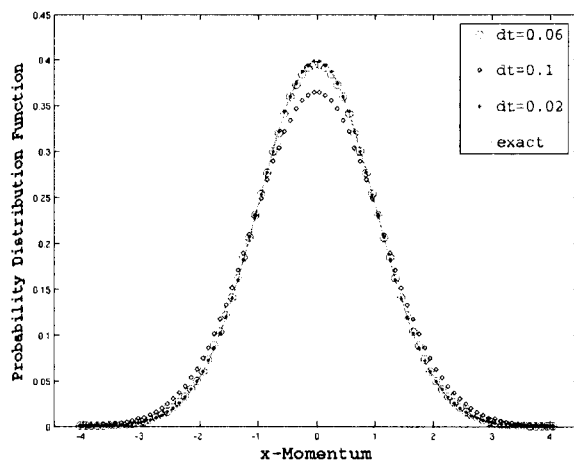


Figure 4.3 Results of momentum distribution for different timestep sizes.

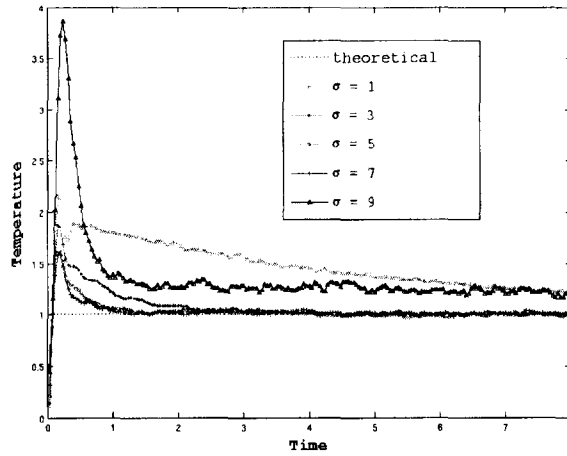


Figure 4.4 Plot of temperature variation against the time for different values of noise amplitude.

4.4 Random Generator and Choice of Random Numbers

Initialization of the positions of DPD particles and DPD interactions require the use of random numbers. In all simulations in this work, uniformly distributed random numbers $u \in U(0,1)$ are used such that $\zeta_{ij} = \sqrt{3}(2u-1)$, where ζ_{ij} represents an independent increment in a stochastic process as discussed in implementing DPD interactions in Chapter 2. This approach is highly efficient since uniform random numbers take less CPU time to generate than Gaussian random numbers, and the results from uniform random numbers are also indistinguishable from those generated by Gaussian random numbers [6]. The seed method is a typical method to generate random numbers, and if we define u_i as a random number, then the form of the equation to generate random numbers that employed is (a multiplicative congruential generator [68])

$$u_i = a u_{i-1} \bmod m, \quad (4.9)$$

where u_i is the i^{th} member of the sequence of pseudorandom numbers, a a multiplier, m the nonzero modulus and the \bmod operator means that $a u_{i-1} \bmod m$ is the least

Chapter 4: DPD Simulation Methods and Parameters

nonnegative remainder from dividing au_{i-1} by m . Careful observation revealed that only certain combination of values of multiplier and m would give good uniformly distributed random numbers. Regardless of how long or short their periods are, congruential generators are deterministic difference equations and phase diagrams can be used to examine their behavior. The points produced by a congruential generator in two or more dimensions lie on hyperplanes. The distance between these hyperplanes varies with the multiplier, which means that some multipliers are better than others [68]. It is more convenient to choose m close to the maximum value that an integer can have in a C program ($2^{31}-1$), and the multiplier is chosen such that u_i can cover all the numbers between 0 and u_i . If the multiplier and m are not set up correctly, the integer random numbers would go through only a limited cycle and result in a bad set of random numbers. The selection of these parameters can be obtained from several references, and we chose the same parameters as the work of [61].

Chapter 5

Simulation Results

In this chapter we study some of the natural difficulties encountered in the implementation of the DPD algorithm for confined fields. Also, we explain the formulas which relate the measured data in the simulations to the macroscopic transport properties. We examine the association between controlling density fluctuations and no slip condition in the cases of Poiseuille and Couette flows. In this chapter we apply our new boundary condition and compare the results with other methods and theoretical Navier-Stokes solutions for the cases of Poiseuille and Couette flows.

5.1 Macroscopic Transport Properties (Data Analysis)

DPD simulation is similar to MD simulation which generates the trajectories of all the particles in the system. To obtain a deeper insight into the system being studied, we need to analyze the trajectories obtained during DPD simulation. In this section, we summarize in the same manner as [4], some of the most commonly performed data analysis in the simulation of fluid transport.

5.1.1 Density Profiles and Diffusion Coefficient

To investigate nanoflows in channels and pores, where the fluid density is inhomogeneous, and also to explore the level of density distortion near boundaries, it is useful to compute the spatial distribution of fluid density, e.g., density profiles along the channel width in Poiseuille flow. This is usually performed using the “binning method” [35]. In this scheme the relevant spatial domain (i.e., the domain where the density distribution of the species needs to be computed) is partitioned into a number of cells, which are identified as the “bins”. The number of particles in each bin is computed from the knowledge of the positions of the particles. In order to obtain a better statistical analysis of the number density in a bin, we add the number of particles in the bin for a number of steps and divide the total number of particles in the bin by the number of steps and the volume of the bin. Thus, the number density, ρ_i , of the i^{th} bin, averaged over s steps, is given by

$$\rho_i = \left\langle \frac{n_i}{VOL_i} \right\rangle_s, \quad (5.1)$$

where n_i is the total number of particles in the i^{th} bin during each step and VOL_i is the volume of the i^{th} bin. Diffusion transport is typically important in most of especially nanofluidic systems. This can be understood by calculating the Peclet number, $P_e = UL/D$, which measures the ratio of bulk transport (convection) to the diffusion transport, or the Schmidt, $S_c = \nu/D$, which approximates the ratio of momentum diffusivity (viscosity) and mass diffusivity. The diffusion coefficient must be generalized in order to describe transport phenomena. For homogenous and equilibrium systems, the diffusion coefficient can be calculated using either the Green-Kubo [69, 70]

$$D = \frac{1}{3} \int_0^\infty \langle \mathbf{v}_i(0) \cdot \mathbf{v}_i(t) \rangle dt, \quad (5.2)$$

where \mathbf{v}_i is the velocity of single particle, or by the Einstein equation [71]

$$2tD = \frac{1}{3} \langle |\mathbf{r}_i(t) - \mathbf{r}_i(0)|^2 \rangle, \quad (5.3)$$

where $\mathbf{r}_i(t)$ is the particle position, which is obtainable from the trajectories generated by the DPD simulation. It should be emphasized here that equations (5.2) and (5.3) are strictly valid only for homogeneous and equilibrium systems.

5.1.2 Velocity and Temperature Profiles

The velocity profile is one of the most important measurables for fluid transport, and can be computed in a similar manner as the density profile. Usually, the simulation system is partitioned into n bins, and the statistics of the fluid velocity are gathered separately in each bin [72]. Assuming that during a s -step simulation, at each step k , there are $n_{k,i}$ particles in the i^{th} bin, and the velocity of each of these particles (denoted by j) is given by $\mathbf{v}_{k,i}^j$, then the average fluid velocity \mathbf{u}_i in the i^{th} bin can be computed by

$$\mathbf{u}_i = \frac{\sum_{k=1}^s \sum_{j=1}^{n_{k,i}} \mathbf{v}_{k,i}^j}{\sum_{k=1}^s n_{k,i}} \quad (5.4)$$

Equation (5.4) is used to compute the steady-state velocity profile. If one is interested in the transient behavior of the velocity profile, an ensemble of simulations will need to be performed. In this case, the velocity profile can still be analyzed using equation (5.4), and the only difference is that the parameter s now denotes the different simulation rather than different time steps. Also, after calculation of streaming velocity in each bin, \mathbf{u}_i , we can compute the temperature of particles in the i^{th} bin by

$$3k_B T_i = \left\langle \left(\frac{1}{n_i} \sum_{j=1, j \in \text{bin}}^{n_i} \mathbf{v}_j^2 \right) \right\rangle - \mathbf{u}_i^2, \quad (5.5)$$

where n_i is the total number of particles in the i^{th} bin during each step.

5.1.3 Stress Tensor

The stress or pressure tensor of an atomic fluid, denoted by $\boldsymbol{\sigma}$, is often defined as the infinitesimal force $d\mathbf{F}$ felt across an infinitesimal area $d\mathbf{A}$, which moves with the local streaming velocity $\mathbf{u}(\mathbf{r}, t)$ of the fluid [73]

$$d\mathbf{F} = d\mathbf{A} \cdot \boldsymbol{\sigma}. \quad (5.6)$$

The pressure tensor can be written as a linear sum of kinetic, $\boldsymbol{\sigma}^k$, and potential, $\boldsymbol{\sigma}^p$, components.

In equation (5.6), at an arbitrary time t , if a particle moves through (or across) the surface, then the kinetic component is deemed to be across the surface $d\mathbf{A}$. The potential component $\boldsymbol{\sigma}^p$, due to inter molecular forces is however, not as easily defined [73]. An interatomic (interparticle) force between two atoms is often said to be “across” the surface if the line between the centers of mass of the two atoms cuts through (or across) the surface defined by $d\mathbf{A}$. This is so-called Irving-Kirkwood convention [74]. However, there is no unambiguous definition of “across” for either the kinetic or the potential contributions to the pressure tensor. For example, there are obvious difficulties that arise in handling many-body force contributions to the potential part of the pressure tensor. Even for pair forces there is no unique way to determine exactly which molecular pairs contribute to $d\mathbf{F}$ [74-76]. Several different techniques have been developed to calculate the potential component of the pressure tensor, and here we present the Irving-Kirkwood expression for the stress tensor at time t [74, 77]

$$\boldsymbol{\sigma}(\mathbf{r}, t) = -\frac{1}{VOL} \left[\sum_i m_i [\mathbf{v}_i(t) - \mathbf{u}(\mathbf{r}_i, t)] [\mathbf{v}_i(t) - \mathbf{u}(\mathbf{r}_i, t)] + \frac{1}{2} \sum_{ij} \mathbf{r}_{ij}(t) O_{ij}(t) \mathbf{f}_{ij}(t) \big|_{\mathbf{r}_i(t)=\mathbf{r}} \right], \quad (5.7)$$

where \mathbf{v}_i is the total particle velocity, \mathbf{u} the streaming velocity of the fluid, VOL the volume of the system, \mathbf{f}_{ij} the force on particle i due to particle j , and $O_{ij}(t)$ the differential operator

$$O_{ij} = 1 - \frac{1}{2!} \mathbf{r}_{ij} \cdot \frac{\partial}{\partial \mathbf{r}} + \dots + \frac{1}{n!} \left[-\mathbf{r}_{ij} \cdot \frac{\partial}{\partial \mathbf{r}} \right]^{n-1} + \dots. \quad (5.8)$$

Thus, from the knowledge of the positions of the particles, velocities of particles, and forces acting on the atoms obtained from a typical DPD run, the stress (or pressure) tensor in the fluid medium can be computed. By assuming only the first term and neglecting the higher-order terms in the above differential operator, we can simplify the Irving-Kirkwood expression for estimating the stress tensor in each bin (for the steady flow field)

$$\boldsymbol{\sigma}_{bin} = -\frac{1}{VOL_{bin}} \left\langle \sum_{i \in bin} (\mathbf{v}_i - \mathbf{u}(\mathbf{r}_i)) (\mathbf{v}_i - \mathbf{u}(\mathbf{r}_i)) + \frac{1}{2} \sum_{ij \in bin} \mathbf{r}_{ij} \mathbf{f}_{ij} \right\rangle. \quad (5.9)$$

Also, the constitutive pressure, p , and the first and second normal stress differences can be respectively defined as

$$\begin{aligned} p &= -\frac{1}{3} \text{tr} \boldsymbol{\sigma} = -(\sigma_{xx} + \sigma_{yy} + \sigma_{zz}) \\ N_1 &= \sigma_{yy} - \sigma_{xx} \\ N_2 &= \sigma_{xx} - \sigma_{zz}. \end{aligned} \quad (5.10)$$

5.1.4 Shear Viscosity

Each molecular-dynamics (MD) method similar to the DPD method for calculating the shear viscosity of fluids will fall into one of two main categories: equilibrium molecular dynamics (EMD) or nonequilibrium molecular dynamics (NEMD) techniques [4]. The EMD techniques involve either the calculation of time correlation functions by measuring the decay of near-equilibrium fluctuations in properties of fluid (Green-Kubo methods) or by accumulating displacements in properties over time (Einstein methods). For example, the Green-Kubo relation for shear viscosity, η , is given by [78]

$$\eta = \frac{VOL}{k_B T} \int_0^\infty \langle \sigma_{xz}(0) \sigma_{xz}(t) \rangle, \quad (5.11)$$

where σ_{xz} is the xz component of the stress tensor $\boldsymbol{\sigma}$ given by equation (5.7) at equilibrium. As the system is in equilibrium, simple periodic boundary conditions are adequate. An alternative EMD method, proposed by Palmer [79], is based on the transverse current autocorrelation function. Hess [80] has compared these two equilibrium methods to nonequilibrium methods in MD simulation.

The NEMD techniques usually involve measuring the macroscopic steady-state response of the system to a perturbing field that may be constant or temporarily varying, and relating the linear response to a transport coefficient. The properties of nonequilibrium steady-state or the decay to the equilibrated state are then related to the viscosity. One of the earliest NEMD techniques, which maintained conventional periodic boundary conditions, involved imposing a spatially periodic external force on the particles to generate an oscillatory velocity profile [78]. The amplitude of this velocity profile at steady state is inversely related to the shear viscosity, and hence the viscosity can be calculated. The more successful NEMD techniques involve imposing the planar Couette

flow velocity profile. One of the most efficient NEMD algorithms for shear viscosity is the Sllod algorithm [77, 81]. The Sllod algorithm has been shown to be exact for arbitrary large shear rates $\dot{\gamma}$, and therefore appropriate for studying non-Newtonian regimes. The strain-rate dependent shear viscosity is obtained from the constitutive equation

$$\eta(\dot{\gamma}) = \frac{\langle \sigma_{xz} \rangle}{\dot{\gamma}}. \quad (5.12)$$

There exists another technique which we have described it in section 3.4 and which we will use them later in our simulations. Both EMD and NEMD methods give similar values for the Newtonian shear viscosities. However, an advantage of the NEMD method is that the shear rate dependence of the viscosity is obtained directly from the NEMD, while EMD provides the zero shear rate value only. Although the NEMD runs can be parallelized for different shear rates, the computation time required to obtain the viscosity is limited by those long simulation runs at low shear rates. Refinements to the traditional NEMD methods been developed that reduce the computational costs by improving the signal-to-noise ratio at small fields [78, 80].

5.2 Bounce Normal Reflection

We have classified and investigated different kinds of boundary conditions in the Chapter 3. In this section we introduce a new reflecting mechanism similar to the other known reflections (bounce-back and specular). In specular reflections the normal component of the momentum of the particles is reversed while the parallel component is conserved

$$\begin{aligned} \mathbf{v}_i^{new} \cdot \mathbf{n}_{wall} &= -\mathbf{v}_i^{old} \cdot \mathbf{n}_{wall} + 2\mathbf{v}_{wall} \cdot \mathbf{n}_{wall} \\ \mathbf{v}_i^{new} \cdot (\mathbf{I} - \mathbf{n}_{wall} \mathbf{n}_{wall}) &= \mathbf{v}_i^{old} \cdot (\mathbf{I} - \mathbf{n}_{wall} \mathbf{n}_{wall}) \end{aligned} \quad (5.13)$$

Chapter 5: Simulation Results

In the bounce-back reflections both components are reversed

$$\mathbf{v}_i^{new} = -\mathbf{v}_i^{old} + 2\mathbf{v}_{wall}, \quad (5.14)$$

where \mathbf{n}_{wall} is the boundary normal unit vector pointed outwards of the boundary, \mathbf{v}_{wall} the velocity of the wall and \mathbf{I} identity dyadic tensor. According to [32, 82] the above reflections have similar temperature and density effects, that we will see later, but the bounce-back may results in better no slip results in low density conditions.

We now define our new bounce-normal reflection as

$$\begin{aligned} \mathbf{E}_1 &= |\mathbf{v}_i^{old} \cdot \mathbf{n}_{vel}| \mathbf{n}_{vel}, \\ \mathbf{E}_2 &= |\mathbf{v}_i^{old} - \mathbf{E}_1| \mathbf{n}_{wall}, \\ \mathbf{v}_i^{new} &= \mathbf{E}_2 - \mathbf{E}_1 + 2\mathbf{v}_{wall}, \end{aligned} \quad (5.15)$$

where \mathbf{n}_{vel} is the unit vector parallel to the boundary velocity. The aim of this reflection form is to prevent accumulation of particles near the wall and push the particles away from the boundary so that it reduces density fluctuation especially in the case of stationary walls. The density distortion near the wall influences the whole domain. It should be noted that these distortions are not an effect of time step size and occur also at other equilibrium temperatures. Although the distortions decrease for higher particle densities in the system, they are still not negligible up to a depth of $0.5r_c$ from the wall for even 3 times the density of the wall particles. To reach a level at which the wall effects can be neglected, either the system must be enlarged to impractical dimensions, or restricted to very high densities. Both these options are computationally costly and undesirable [32]. We will examine some of these effects in subsequent simulation results. In all mentioned cases we may also have different reflections in displacements. For instance the bounce-forward is the same as bounce-back in velocity components but different in the position (See Figure 5.1).

In Figure 5.1, the schematic diagram of different reflections is shown. The particle which has an initial velocity of \mathbf{V}_i is at \mathbf{r}_i^t before it hits the boundary at the time t . If there is no wall boundary and the total effective force from all the surrounding particles (wall and fluid particles) is not sufficient to prevent the impact, the particle will penetrate into the wall region and be positioned at \mathbf{r}_i^{t+dt} within the boundary. It has been illustrated [32] that the specular and bounce-back reflections for the position (as shown in Figure 5.1) have virtually the same slip effects and there is thus not much difference in using either. The velocity of particle at position \mathbf{r}_i^{t+dt} can be derived using any of the mentioned reflection mechanisms.

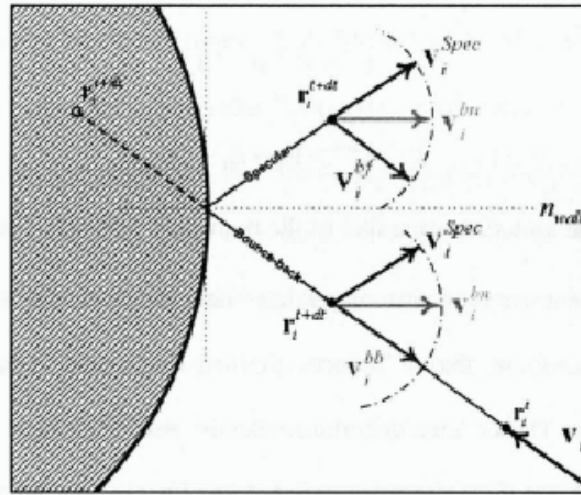


Figure 5.1 Schematic diagram of bounce-back (bb), bounce-forward (bf), specular (Spec) and bounce-normal (bn) for particle that penetrates into the stationary wall region.

5.3 Diagnostic DPD Simulations

5.3.1 Poiseuille Flow

In order to appreciate the degree of difficulty when imposing no-slip boundary conditions with the DPD method and to identify the most influential parameters especially on density fluctuations, we first perform some diagnostic DPD simulations for Poiseuille flow in a channel, similar in some extent to the work of Pivkin-Karniadakis

Chapter 5: Simulation Results

[45]. 13500 fluid particles are randomly distributed into the channel box of size $x:15 \times y:15 \times z:15$ which results in an average number density of $\rho_f = 4.0$. The periodic boundary conditions are imposed along y and z directions. The frozen particles which are distributed randomly from the beginning were used to represent two channel walls in the y - z plane (see Figure 5.2). The randomly scattered wall particles could somewhat represent the local effect of roughness of surfaces in micro/nano applications and it shows smaller slips comparing to other combinations. The values of $\sigma = 3.0$, $\gamma = 4.5$, $k_B T = 1.0$ and $a_{ff} = 18.75$ are assigned to the coefficients of the DPD equations. In order to sustain the flow an external body force of $F_e = 0.02$ is imposed in the y direction. To investigate the effect of wall density, we will use different values for the number density of the walls, ρ_w . In addition, we will vary the conservative force parameter for the fluid-wall particles, a_{fw} . The simulation domain is partitioned into 300 bins along the y direction and statistics of the fluid parameters (density, velocity, temperature, stress tensor...) are computed separately in each bin. A large number of bins is selected in order to examine the fluctuations correctly. The time step is set to $\Delta t = 0.02$ and simulations were run for $t = 5000$ (250,000 time steps) and all the steady profiles are averaged after $t = 4000$ (the last 50,000 time steps). The stress tensor σ , constitutive pressure p and other parameters can be estimated in each bin with the expressions given earlier in section 5.1.

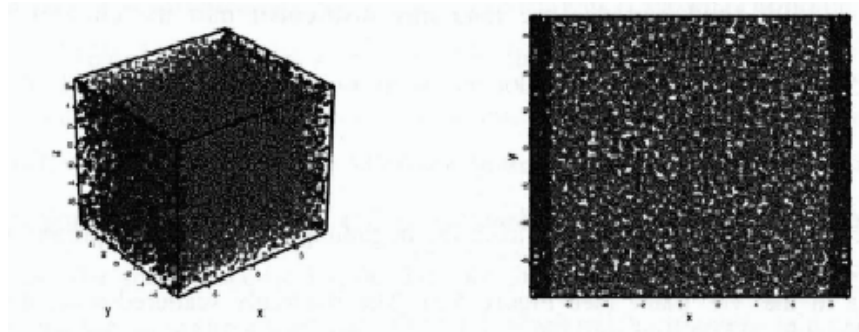


Figure 5.2 The 3D and 2D position of the wall (blue balls) and the fluid (green small balls) DPD particles distribution in the simulation box.

First, we examine the model with the simple random distribution of particles inside the wall regions. 900 particles are located randomly inside each wall domain with the thickness of $r_c = 1$, and this leads to the same density of wall and fluid particles, $\rho_w = \rho_f = 4.0$. We also set the same conservative parameter for the wall-fluid and the fluid-fluid interactions, $a_{wf} = a_{ff} = 18.75$. The simulation results are shown in Figure 5.3, and it is obvious from this figure that the soft repulsion between particles pushes the fluid particles into the wall regions. As discussed before one way to avoid this penetration is by increasing the wall density or by strengthening the conservative repulsion parameter. Thus we increase the wall density to two times larger than fluid particles density $\rho_w = 2\rho_f = 8$. The results of this simulation are shown in Figure 5.4, and it is seen that the penetration is reduced; however, there exist large density fluctuations which are propagated across the channel. Next we increase the repulsion parameter between fluid and wall particles and keep the wall density equal to that of the fluid, $a_{wf} = 2a_{ff} = 37.5$. Figure 5.5 shows the result of this increase and it is observed that there is a slightly smaller slip; however there exists penetration of fluid particles to the walls. Unlike the method of Pivkin-Karniadakis [45], which simulated the wall particles the structured patterns and there existed large amounts of slip for these cases,

Chapter 5: Simulation Results

using the current random combinations results in smaller slip compared to the structured models. According to these results we can also conclude that increasing the density or repulsion parameter are not appropriate ways to prevent particle-penetration into the boundary regions. Also it is important that in the case of random distribution of particles inside the walls, changing the conservative parameter does not significantly affect the slip factor.

Chapter 5: Simulation Results

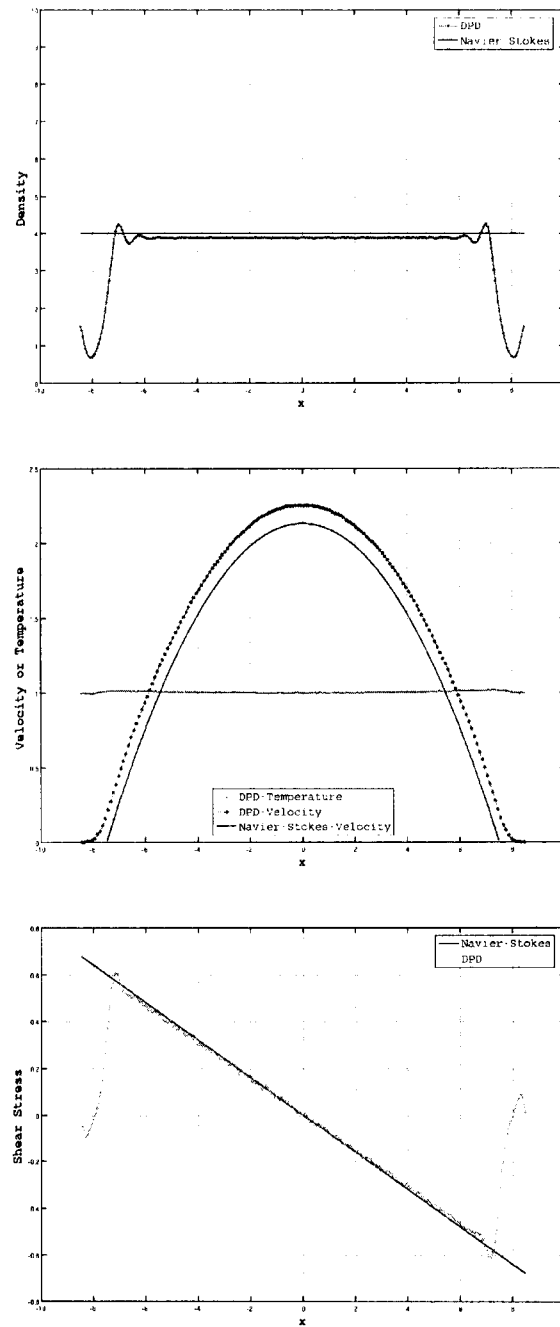


Figure 5.3 Top: Density profile. Middle: Temperature and Velocity profiles. Bottom: Shear Stress Profile. The Navier-Stokes solutions are shown with solid lines. Model with walls of random frozen particles ($\rho_w = \rho_f$; $a_{wf} = a_{ff}$).

Chapter 5: Simulation Results

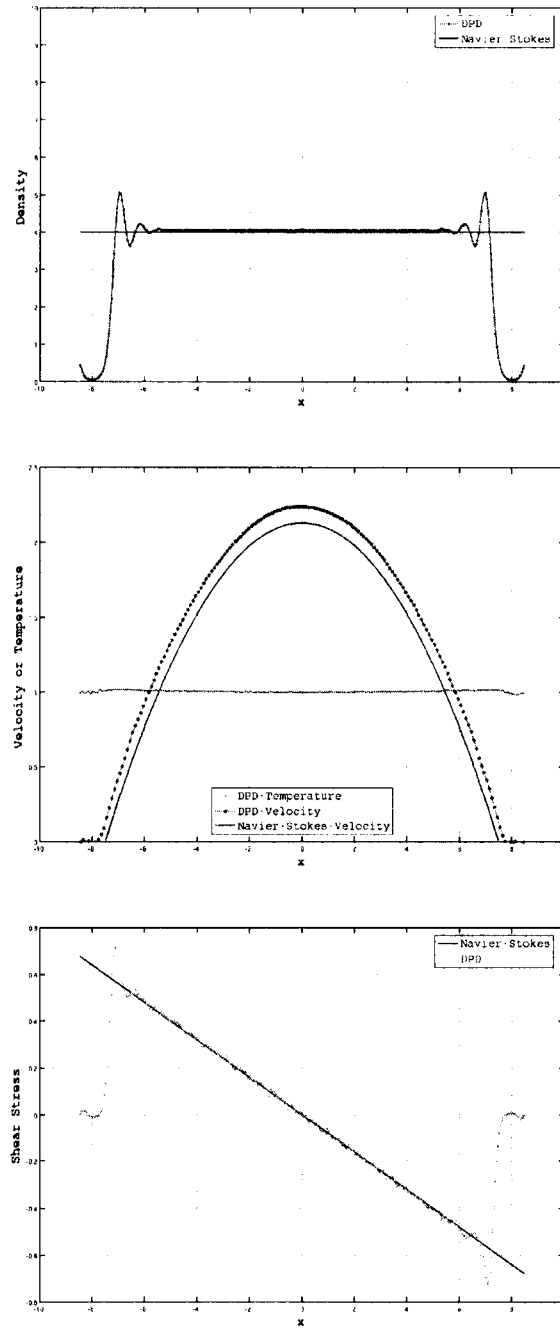


Figure 5.4 Top: Density profile. Middle: Temperature and Velocity profiles. Bottom: Shear Stress Profile. The Navier-Stokes solutions are shown with solid lines. Model with walls of random frozen particles ($\rho_w = 2\rho_f$; $a_{wf} = a_{ff}$).

Chapter 5: Simulation Results

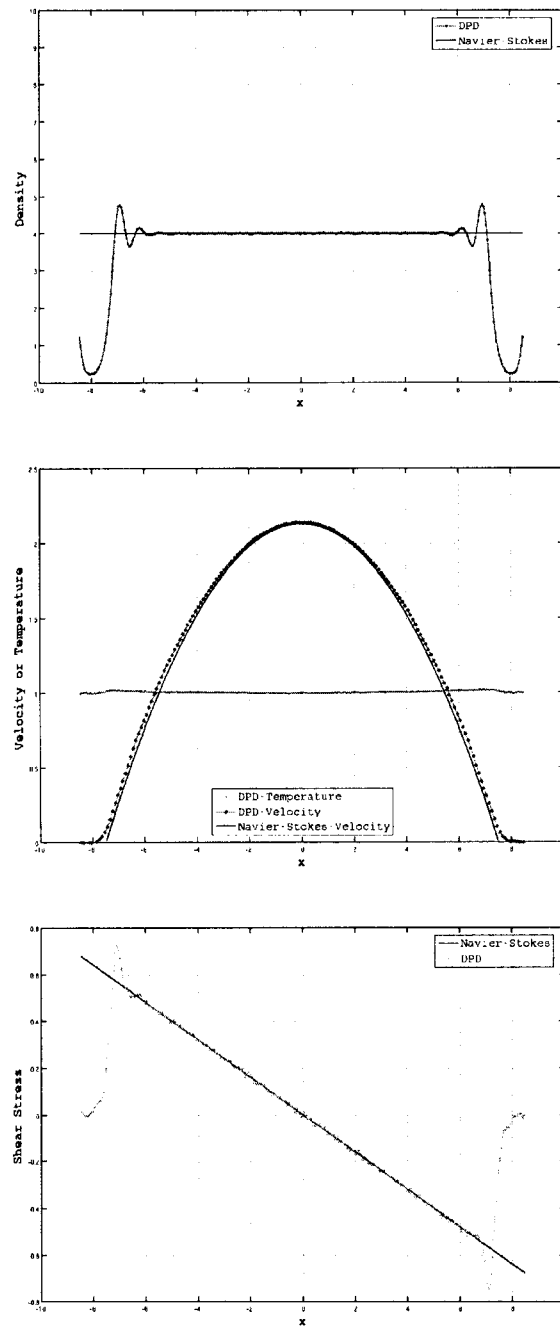


Figure 5.5 Top: Density profile. Middle: Temperature and Velocity profiles. Bottom: Shear Stress Profile. The Navier-Stokes solutions are shown with solid lines. Model with walls of random frozen particles ($\rho_w = \rho_f$; $a_{wf} = 2a_{ff}$).

Now in order to prevent penetration of fluid particle into the walls, we employ reflecting boundary conditions. To test the effects of the different reflections we first apply the bounce-back reflection. Figure 5.6 shows the results for the same density of wall and fluid particles, and the wall particles are scattered inside the wall randomly. Also in order to have a scale to compare our new boundary condition with, we employ the method of Pivkin-Karniadakis [45], i.e. using the structured boundary condition and estimating the repulsion parameter with the following formula. The results are shown in Figure 5.7.

$$a_{wf} = \frac{0.39(\rho_f k_B T + 0.1 a_{ff} \rho_f^2)}{0.0303 \rho_w^2 + 0.5617 \rho_w - 0.8536} \quad (5.16)$$

According to Figure 5.6 and Figure 5.7 we find that by applying these methods we may satisfy the no slip condition but there are large fluctuations in the density profiles. This density distortion leads to significant fluctuations in pressure and shear stress. In Figure 5.8 the total constitutive pressure and first and second normal stress differences are shown. In this figure we observe large amount of fluctuation which is originated from the density distortion.

Pivkin and Karniadakis introduced a general adaptive method in order to make density profile flat [83]. Their method is not easily applicable to complex geometries, incurs additional computational cost, and there also exists some temperature rise close to the wall.

Next we apply our new method which uses the combination of randomly distributed wall particles and the new bounce-normal reflection. This combination is easy to implement without additional computational cost and without causing much distortions in macroscopic properties. The results of this method are shown in Figure 5.9 and Figure 5.10. As can be observed from the figures, in the case of bounce-normal reflection there

Chapter 5: Simulation Results

exists a very small amount of slip near to the wall (less than 3%). In addition, the density fluctuations are negligible compared to the other methods and as such this method demonstrates its clear advantages. We can also decrease the amount of slip by decreasing the wall repulsion parameter. However, by doing so, the fluctuations in the other flow parameters would be increased significantly.

Another important effect of wall is the distortion in the temperature profiles very close to the wall, which is not avoidable in all simulated cases (this is also clearly apparent in other publications). However this distortion is negligible because it is very small and near the wall, and it also does not have significant effects in simulations which do not involve thermal phenomena.

Chapter 5: Simulation Results

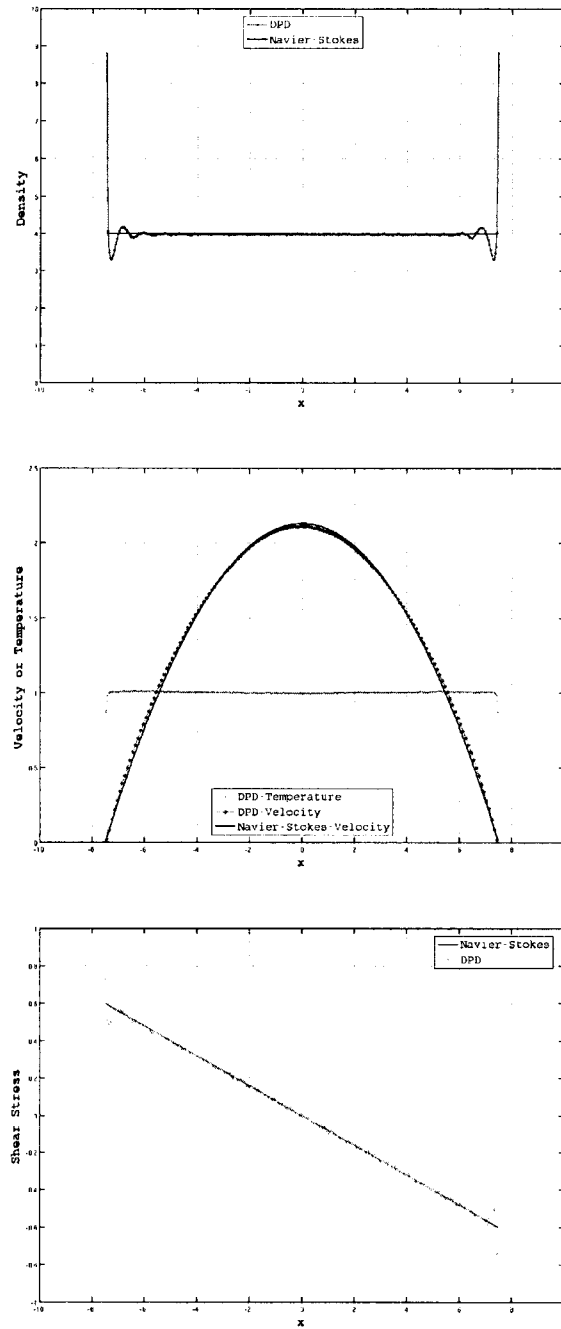


Figure 5.6 Top: Density profile. Middle: Temperature and Velocity profiles. Bottom: Shear Stress Profile. The Navier-Stokes solutions are shown with solid lines. Model with walls of random frozen particles combined with bounce-back reflection ($\rho_w = \rho_f$; $a_{wf} = a_{ff}$).

Chapter 5: Simulation Results

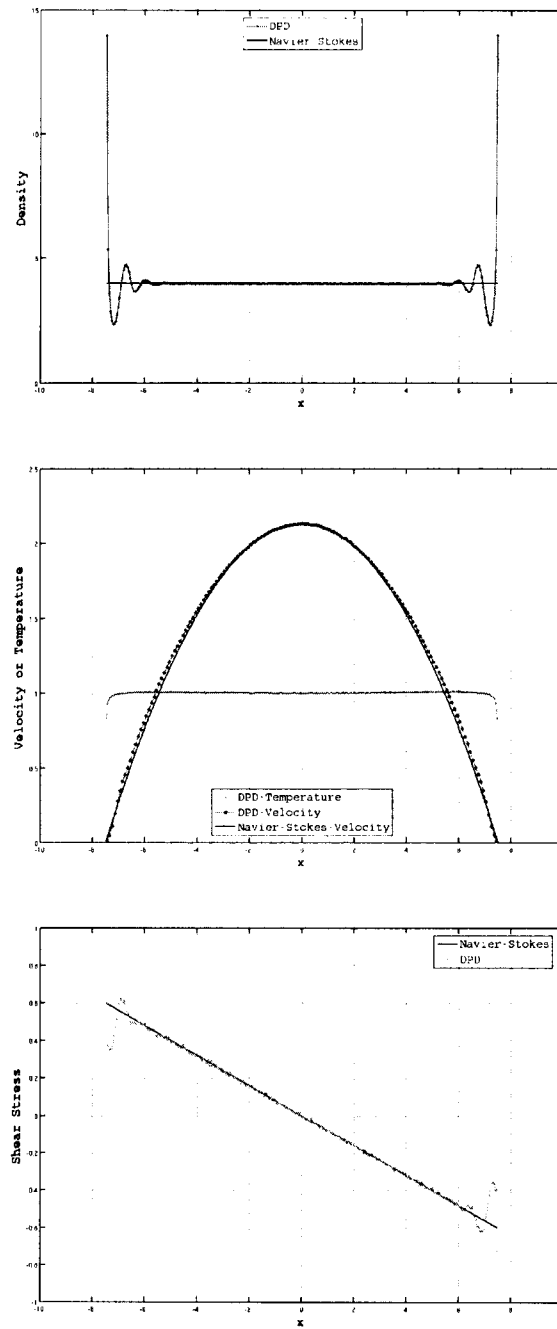


Figure 5.7 Top: Density profile. Middle: Temperature and Velocity profiles. Bottom: Shear Stress Profile. The Navier-Stokes solutions are shown with solid lines. Model with walls of two layer structured particles combined with bounce-back reflection ($\rho_w = \rho_f$; $a_{wf} = 0.3766 a_H$).

Chapter 5: Simulation Results

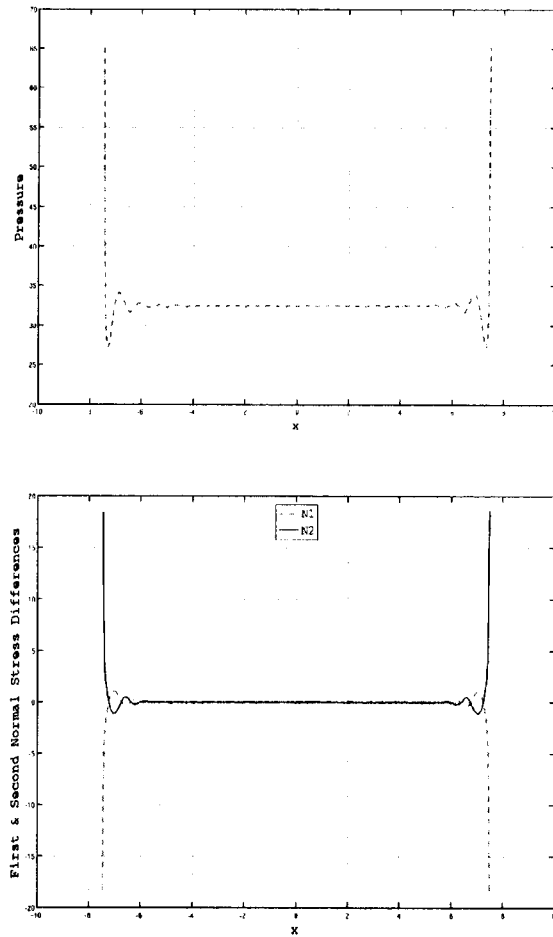


Figure 5.8 Top: Pressure profile. Bottom: First and second normal stress differences profiles. Model with walls of random frozen particles combined with bounce-back reflection ($\rho_w = \rho_f$; $a_{wf} = a_{ff}$).

Chapter 5: Simulation Results

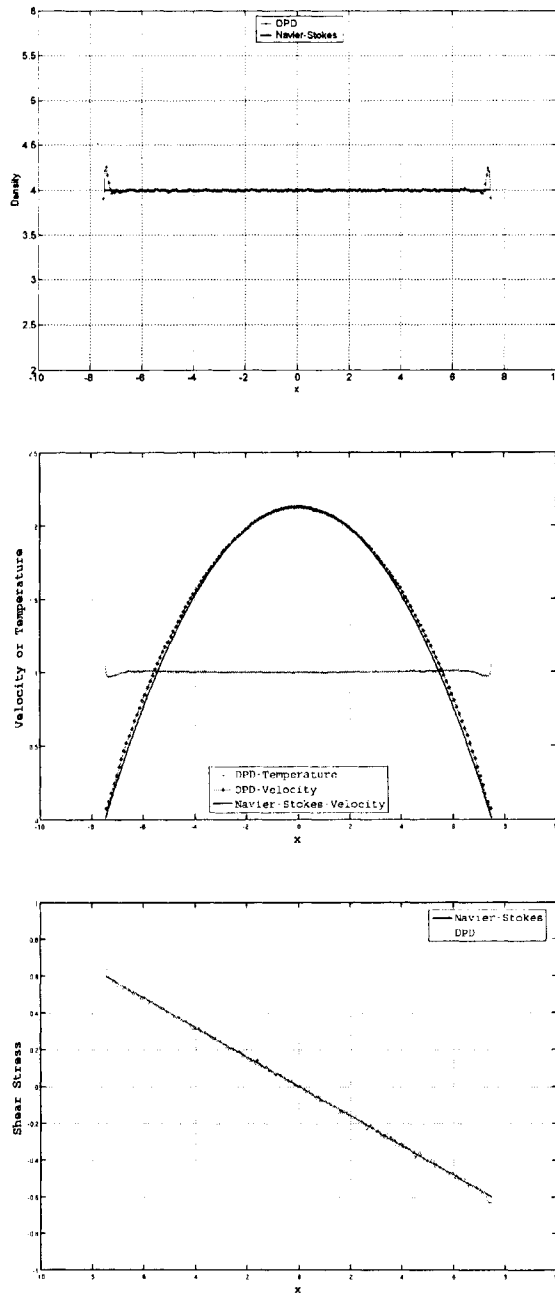


Figure 5.9 Top: Density profile. Middle: Temperature and Velocity profiles. Bottom: Shear Stress Profile. The Navier-Stokes solutions are shown with solid lines. Model with walls of random frozen particles combined with bounce-normal reflection ($\rho_w = \rho_f$; $a_{wf} = a_{ff}$).

Chapter 5: Simulation Results

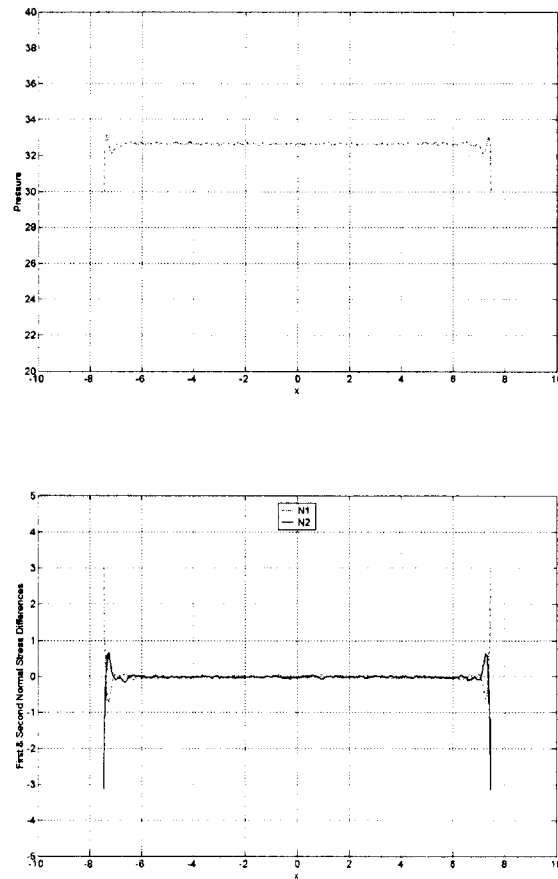


Figure 5.10 Top: Pressure profile. Bottom: First and second normal stress differences profiles. Model with walls of random frozen particles combined with bounce-normal reflection ($\rho_w = \rho_f$; $a_{wf} = a_{ff}$).

Chapter 5: Simulation Results

Also in order to verify our new method for the case of Poiseuille flow we implement the method for higher density of particles, $\rho_w = \rho_f = 9.0$ and $a_{wf} = a_{ff} = 8.33$. As shown in Figure 5.11, for higher densities the results are similar (the small difference in the velocity profile is due to small number of time steps and the profile would be similar if we run simulation with more time steps).

We can also estimate the viscosity of the simulation by comparing the results with the Navier-Stokes solution. By simplifying the Navier-Stokes equations with the appropriate boundary condition related to Poiseuille flow, one obtains

$$\begin{aligned} u_y(x) &= \frac{\rho F_e h^2}{2\eta} \left(1 - \left(\frac{x}{h}\right)^2\right), \\ \sigma_{xy} &= \eta \frac{\partial u_y(x)}{\partial x} = -\rho F_e x, \end{aligned} \quad (5.17)$$

where x is the distance from the middle of the channel, $h = 7.5$ is half the channel width, η is the apparent viscosity and $F_e = 0.02$ is the external field force in the y direction applied to the fluid. Also σ_{xy} is the shear stress along the channel width. There are two ways to estimate the apparent viscosity of the simulation. One is to compare the maximum velocity with the related Navier-stokes maximum velocity and determine the viscosity as

$$\eta = \frac{\rho F_e h^2}{2u_{\max}} \quad (5.18)$$

The other involves the calculation of the average simulated velocity, \bar{u} , and compare it with the theoretical value. If we use this method

$$\eta = \frac{\rho F_e h^2}{3\bar{u}}. \quad (5.19)$$

Chapter 5: Simulation Results

We applied both these two methods and calculated the apparent viscosity for each, the results are $\eta = 1.055$ and $\eta = 1.0352$ from the first and second methods respectively.

Chapter 5: Simulation Results

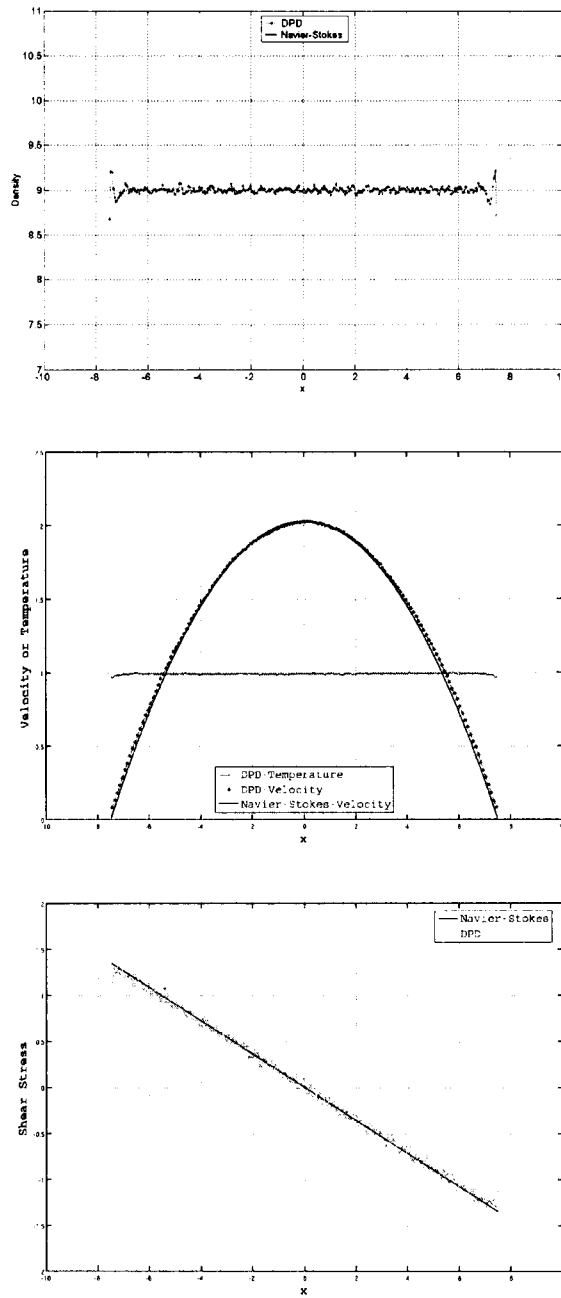


Figure 5.11 Top: Density profile. Middle: Temperature and Velocity profiles. Bottom: Shear Stress Profile. The Navier-Stokes solutions are shown with solid lines. Model with walls of random frozen particles combined with bounce-normal reflection ($\rho_w = \rho_f = 9$; $a_{wf} = a_{ff}$).

5.3.2 Couette Flow

In order to further validate the new boundary bounce-normal reflection, we now apply it to pure shear flow. For simulating the shear flow, we remove all the external body forces. In order to impose arbitrary shear rate we move the right wall with the velocity of \mathbf{v}_{wall} and the left wall with the opposite velocity of $-\mathbf{v}_{wall}$ both in the y direction. The relative velocity profile is obtained by dividing the velocity by \mathbf{v}_{wall} . It should be noted that as the temperature sets the energy scale, the imposed shear rate should be applied such that its maximum velocity is at most of the order of the thermal velocity [66].

We use the same parameters of the Poiseuille flow except for the wall density and repulsion parameter between the wall and the fluid DPD particles. It was observed that if we use the same repulsion parameter, we would incur large amount of slip near the wall regions. Thus we decrease the repulsion parameter of wall particles to $a_{wf} = 0.7 a_{ff}$. As it is demonstrated in Figure 5.12, the amount of slip is now in acceptable order, but again there exist density distortion. In order to obtain smaller slip we may further lower the wall repulsion. Here we suggest using equation (5.16) for estimating and decreasing the repulsion parameter. The results of this are shown in Figure 5.13. From this figure we observe that the no slip condition is achieved however there exists large fluctuation in the other parameters.

To overcome this problem, we not only have to decrease the repulsion parameter, but also increase the wall density. The reduction in repulsion parameter causes the accumulation of fluid particles near the walls and resulting in the density fluctuation. By increasing the wall density and using the bounce-normal reflection mechanism we effectively push the particles towards the fluid domain. After several trial simulations we

Chapter 5: Simulation Results

set the repulsion parameter to $a_{fw} = 7.06$ and increase the wall density to $\rho_w = 10.0$. The results are shown in Figure 5.14. Now we observe that the fluctuation and the slip are both more appropriate and matching the macroscopic properties. Also we find that the advantage of using randomly distributed particles over structured ones for the boundary regions, is that as we increase the wall density the no-slip condition is satisfied to some extent.

In addition we can estimate the apparent viscosity also for the shear flow by comparing the shear stress with the theoretical value. The Navier-Stokes solution for the Couette flow is

$$\begin{aligned} u &= u_{\max} \frac{x}{h} \\ \sigma_{xy} &= \eta \frac{\partial u_y(x)}{\partial x} = \frac{\eta}{h} u_{\max} \end{aligned} \quad (5.20)$$

Here $u_{\max} = 1$ and by using the above equation we find the apparent viscosity $\eta = 1.0312$, which is close to the estimated values of Poiseuille simulations. Also the results of the normal stress differences and pressure are shown in Figure 5.15.

Chapter 5: Simulation Results

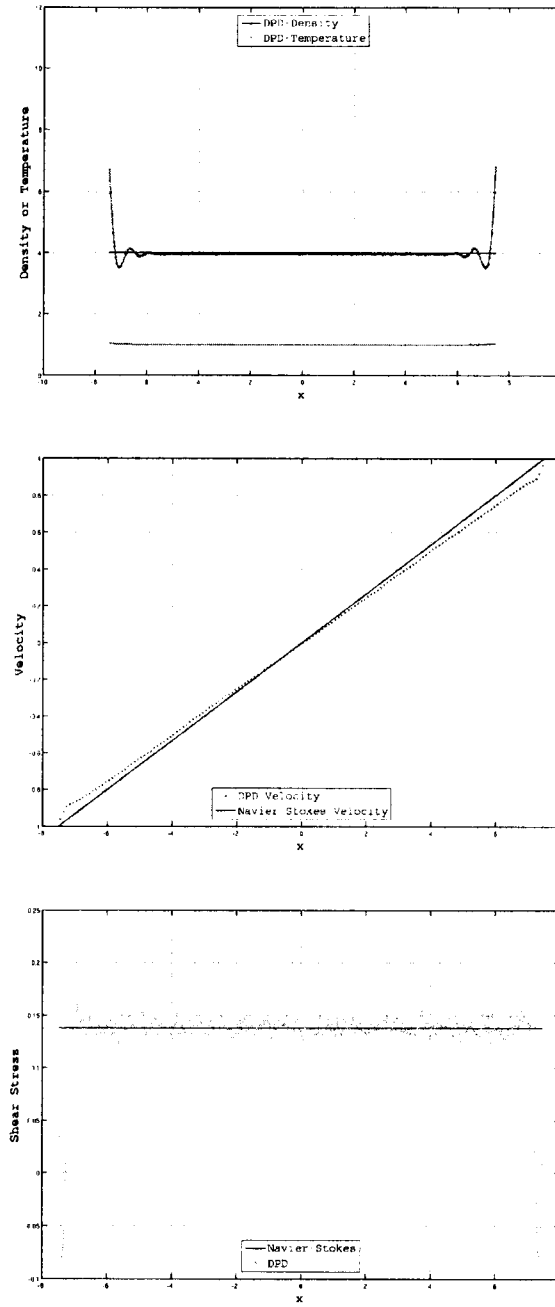


Figure 5.12 Couette flow. Top: Density and Temperature profiles. Middle: Velocity profile. Bottom: Shear Stress Profile. The Navier-Stokes solutions are shown with solid lines. Model with walls of random frozen particles combined with bounce-normal reflection ($\rho_w = \rho_f = 4$; $a_{w/f} = 0.7a_B$).

Chapter 5: Simulation Results

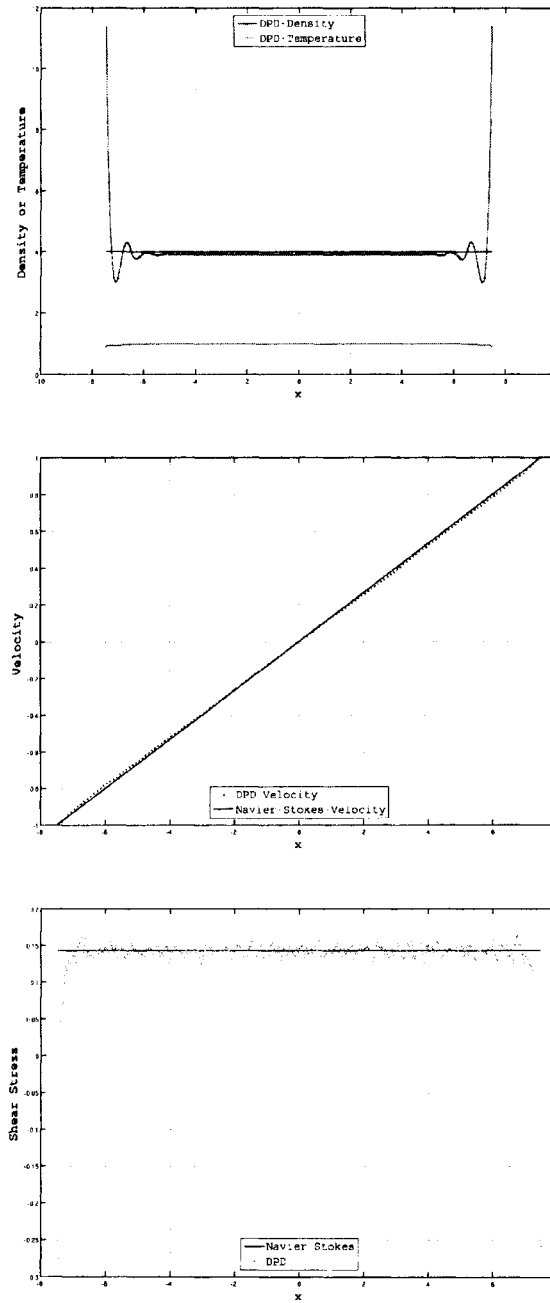


Figure 5.13 Couette flow. Top: Density and Temperature profiles. Middle: Velocity profile. Bottom: Shear Stress Profile. The Navier-Stokes solutions are shown with solid lines. Model with walls of random frozen particles combined with bounce-normal reflection ($\rho_w = \rho_f = 4$; $a_{wf} = 0.3766a_{ff}$).

Chapter 5: Simulation Results

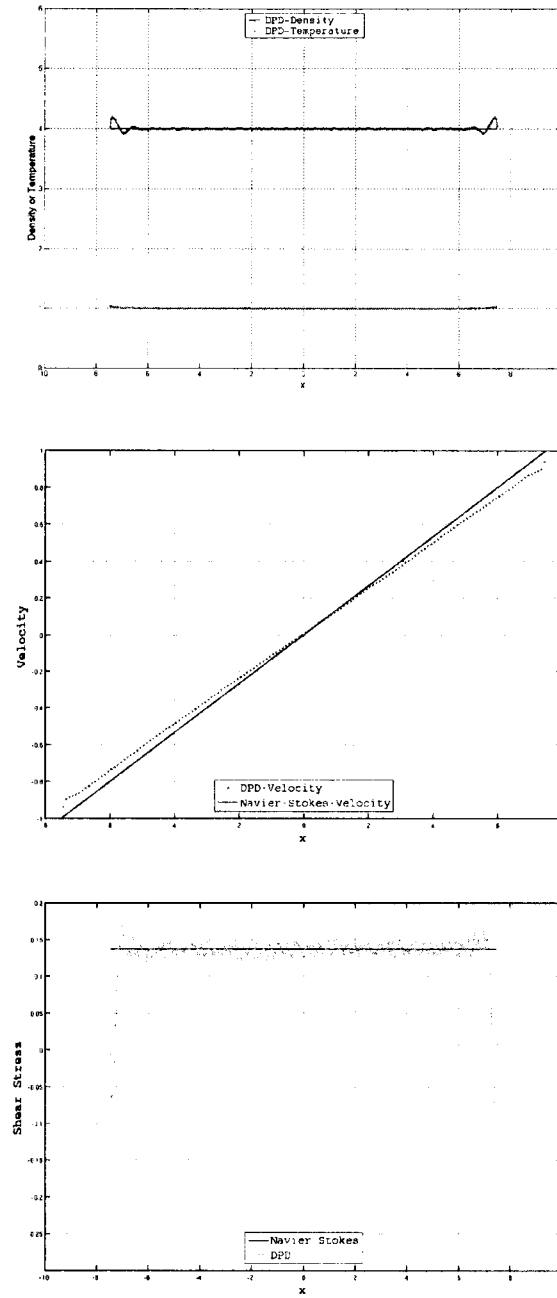


Figure 5.14 Couette flow. Top: Density and Temperature profiles. Middle: Velocity profile. Bottom: Shear Stress Profile. The Navier-Stokes solutions are shown with solid lines. Model with walls of random frozen particles combined with bounce-normal reflection ($\rho_w = 10$; $a_{wf} = 0.3766a_{ff}$).

Chapter 5: Simulation Results

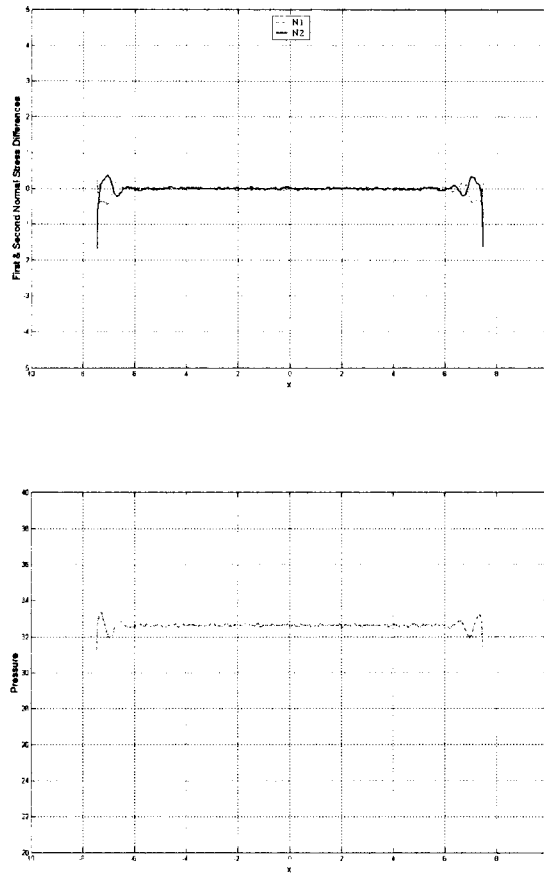


Figure 5.15 Couette flow. Top: Pressure profile. Bottom: First and second normal stress differences profiles. Model with walls of random frozen particles combined with bounce-normal reflection ($\rho_w = 10; a_{wf} = 0.3766a_{ff}$).

5.4 Lid-Driven Cavity with Low Reynolds Number

Finally, we simulate Lid-driven Cavity flow as it has been regularly used to test or validate new codes or new solution methods. The particles are distributed in the box size of $x:10 \times y:10 \times z:10$ and the density of the both DPD fluid and wall particles are set at $\rho_f = \rho_w = 10.0$. We have selected the values of $k_b T = 1/3$, $\sigma = \sqrt{3}$, $\gamma = 4.5$ for the temperature, random and dissipative force coefficients respectively. The four surrounding walls are again modeled with the random distribution of particles in combination with bounce-normal reflection and we assume the periodic condition in the z -direction. The conservative parameter is set to $a_{wf} = a_{ff} = 3.0$ for the interaction between particles. The left wall is a moving lid with constant velocity and other three walls are at rest. We calculated the conservative force coefficient from equation (5.16) as $a_{wf} = 1.67$, for the interaction of fluid particles with the moving wall. In order to calculate the Reynolds number, we estimate the dynamic viscosity of the fluid from Poiseuille flow simulation and the results are $\eta = 2.069$ and $\eta = 2.03$ from the average and maximum methods respectively. To estimate the Reynolds number, we assume the apparent viscosity to be $\eta = 2.05$. We run the simulation for 250,000 time steps and the final velocity profiles are averaged over the last 50,000 steps in 200 bins. The left lid is moving with the constant velocity of $V = 0.41$ which leads to a Reynolds number of

$$\text{Re} = \frac{\rho V L}{\eta} = 20.0. \quad (5.21)$$

In order to validate our results, we compare with corresponding results obtained by the FLUENT CFD package, which is based on discretization of Navier-Stokes equation. We selected the 2D grid size of 160×160 which provided mesh independent results, and

Chapter 5: Simulation Results

chose other parameters to achieve a Reynolds number of 20. In FLUENT we fix the 10×10 box size and select the density and viscosity as $\rho = 1$ and $\eta = 1$ respectively. Thus, for a Reynolds number of 20.0, we require $V = 2$ for the lid velocity. Also for both DPD and Navier-Stokes, we normalized the coordinates and the velocity profiles by the domain size of 1×1 and the lid velocity of $V = 1$.

We compare results of DPD and Navier-Stokes calculations in Figure 5.16 to Figure 5.18. In these figures, we present the contour fields of different velocity components. These figures show overall excellent agreement of DPD results with bounce-normal reflection, when compared to the Navier-Stokes simulations.

Additionally and in order to investigate and compare the DPD results more precisely, the velocity profiles along the horizontal and vertical cut lines in different positions of domain ($x = 0.25, 0.5, 0.75$ and $y = 0.25, 0.5, 0.75$) are depicted in Figure 5.19 to Figure 5.21. We observe an excellent agreement between the two methods. We only see some inconsistency of velocity contours at the corner point which is due to different treatment of boundary condition at these points and is unavoidable. In addition for the DPD density profiles, we obtained almost flat profiles except for some small fluctuation near the left moving wall.

Chapter 5: Simulation Results

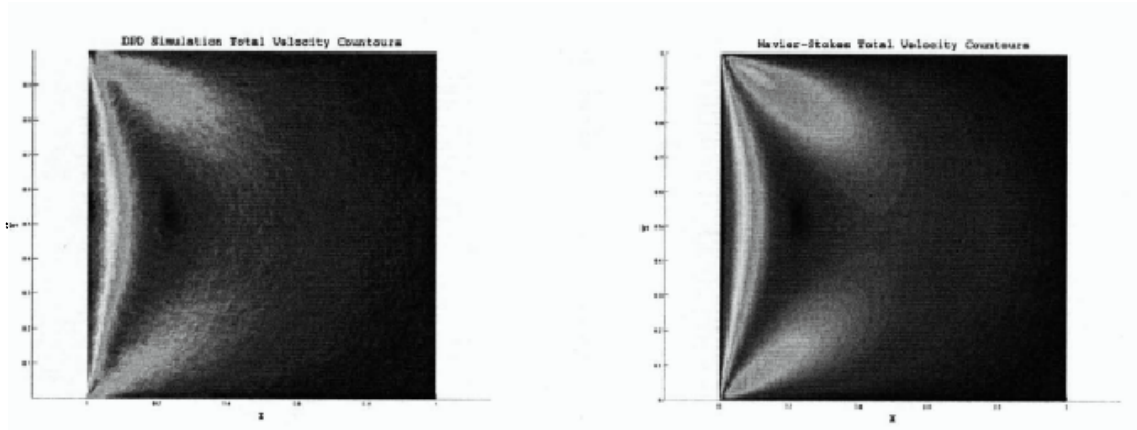


Figure 5.16 Contour plot of lid-driven cavity flow. Left: Total velocity of DPD simulation. Right: Total velocity of Navier-Stokes simulation.

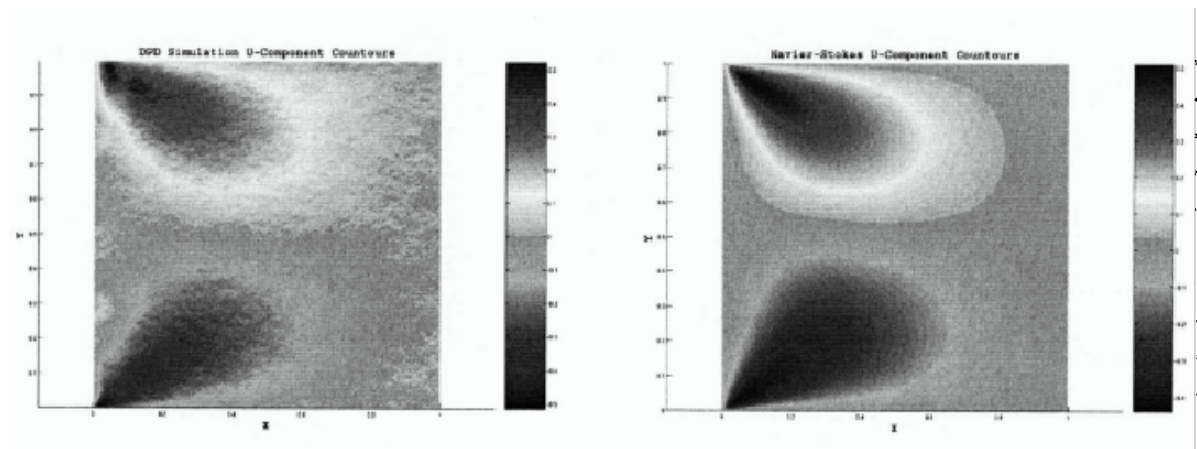


Figure 5.17 Contour plot of lid-driven cavity flow. Left: V-component velocity of DPD simulation. Right: V-component velocity of Navier-Stokes simulation.

Chapter 5: Simulation Results

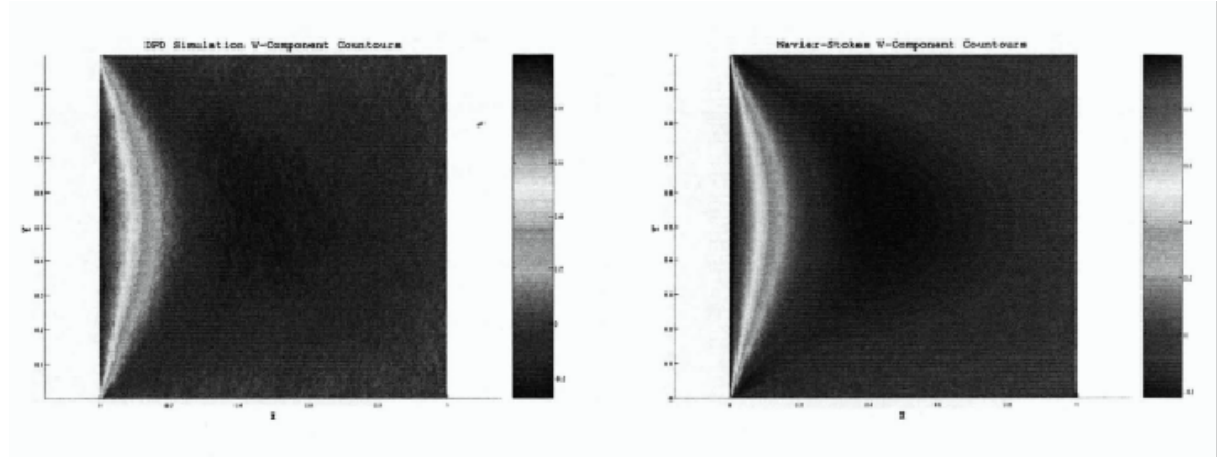


Figure 5.18 Contour plot of lid-driven cavity flow. Left: U-component velocity of DPD simulation. Right: U-component velocity of Navier-Stokes simulation.

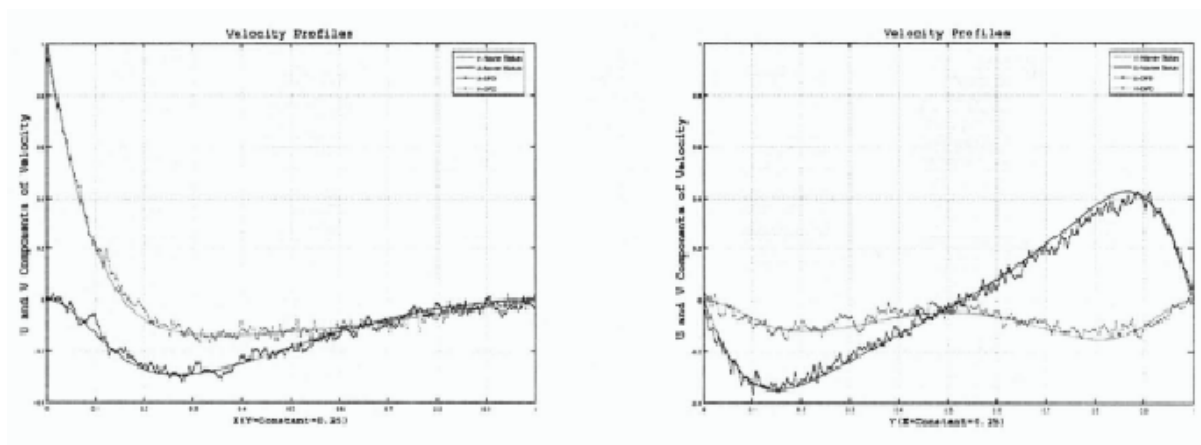


Figure 5.19 DPD and Navier-Stokes comparison of velocity profiles. Left: U and V profiles along the horizontal line at $y=0.25$. Right: U and V profiles along the vertical line at $x=0.25$. (DPD Results are shown with dotted lines)

Chapter 5: Simulation Results

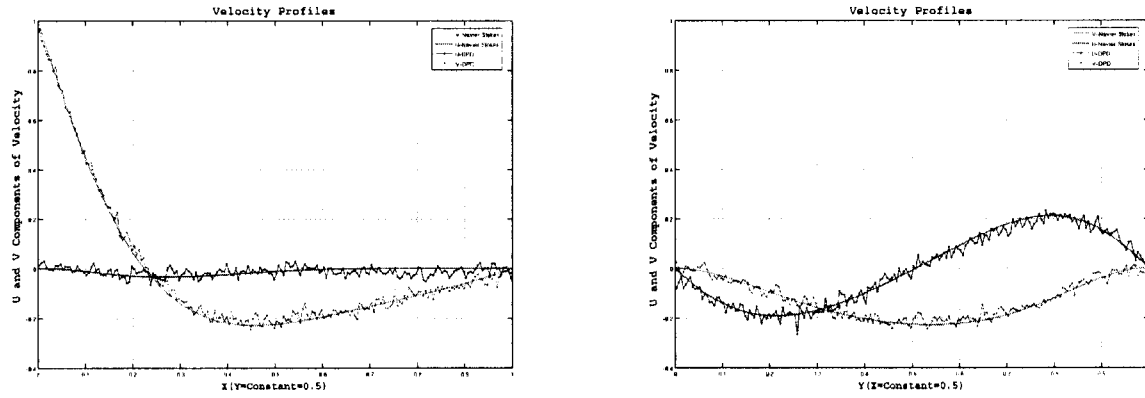


Figure 5.20 DPD and Navier-Stokes comparison of velocity profiles. Left: U and V profiles along the horizontal line at $y=0.5$. Right: U and V profiles along the vertical line at $x=0.5$. (DPD Results are shown with dotted lines)

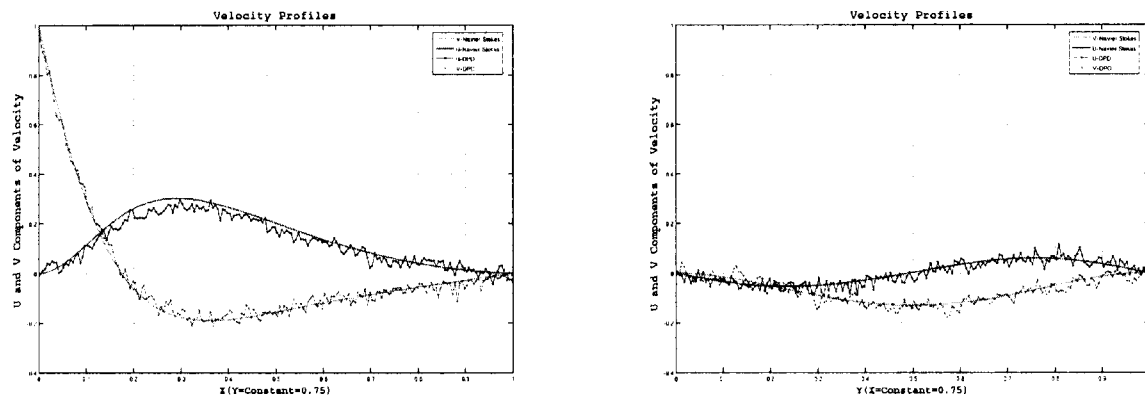


Figure 5.21 DPD and Navier-Stokes comparison of velocity profiles. Left: U and V profiles along the horizontal line at $y=0.75$. Right: U and V profiles along the vertical line at $x=0.75$. (DPD Results are shown with dotted lines)

5.5 Conclusions

In terms of DPD refinement, we have managed to attain significant reduction in fluctuations in important parameters such as the density and shear stress distributions which affect the macroscopic flow properties. This was achieved by the following:

- Establishing a new bounce-normal reflection mechanism.
- Deploying a random wall particle distribution and enforcing non-penetration.

The density and shear stress fluctuations are thus controlled by the general mechanism of this new reflection, which adds to the thermal fluctuations and pushes the particles due to this thermal energy normally toward the bulk flow. This effectively prevents accumulation of particles near the walls and flattens the density profile.

At this juncture, we are ready to progress to model the entropic trap geometries, and also investigate the various particle chain models to simulate the DNA chains as they traverse through the trap arrays.

Chapter 6

Polymer Physics Theory, Basic Concepts and DPD

6.1 Ideal Chains

We can define an ideal chain as the simplest chain without any interactions between monomers. The polymer chain is constructed from many internal atomistic links with each of bond length l that can be assumed as an almost constant parameter. For each $X-X$ atomic bound, there exists rotational freedom which is the main source of flexibility in polymers. This flexibility is due to the variation of torsion angles and causes the polymer to be thought of as a long piece of string (see Figure 6.1). If there is no variation in torsion angle of all bonds in the chain, and the torsion angle has the trans state, then the chain attains its longest end-to-end distance or contour length of $R_{\max} = nl \cos(\theta/2)$, where n is the number of bonds and θ is the angle between bonds.

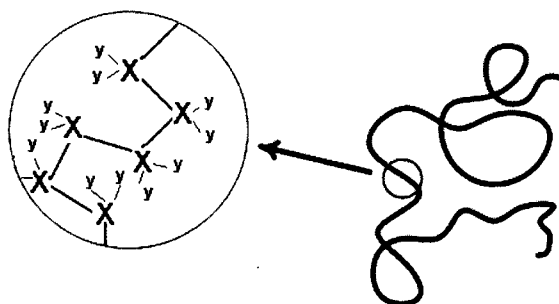


Figure 6.1 The atomic and overall structure of sample polymer chain.

Chapter 6: Polymer Physics Theory, Basic Concepts and DPD

First we assume an ideal or freely-jointed chain where there is no correlation between the directions that different bonds take. In this case there are no net interactions between the atoms associated with each bond, and all directions have the same probability and we are thus able to map every possible conformation of an ideal chain onto a random walk and apply all statistical properties of random walk theory to our model of a freely-jointed chain. In this very simple approach where no interactions between monomers are considered, the energy of the polymer is taken to be independent of its shape, which means that at thermodynamic equilibrium, all of its possible shape configurations are equally likely to occur as the polymer fluctuates in time, according to the Maxwell-Boltzmann distribution. As it is shown in Figure 6.2, the end-to-end vector is the sum of all n bond vectors in the chain, $\vec{R}_n = \sum_{i=1}^n \vec{r}_i$. The ensemble average of this vector is zero $\langle \vec{R}_n \rangle = 0$, since there is an equal probability to walk in every direction. To estimate the length of the chain, we shall calculate the average mean-square end-to-end distance:

$$\begin{aligned} \langle \vec{R}_n^2 \rangle &= \langle \vec{R}_n \cdot \vec{R}_n \rangle = \sum_{i=1}^n \sum_{j=1}^n \langle \vec{r}_i \cdot \vec{r}_j \rangle = l^2 \sum_{i=1}^n \sum_{j=1}^n \langle \cos \theta_{ij} \rangle \\ &= nl^2. \end{aligned} \quad (6.1)$$

The main assumption for the derivation of equation (6.1) is the freely jointed chain model, i.e. a constant bond length, $l = |\vec{r}_i|$ and no correlations between the directions of different bond vectors, $\langle \cos \theta_{ij} \rangle = 0$ for $i \neq j$. We can define the Flory's characteristic ratio, C_n in order to include short range interactions. This ratio depends on distances and limits which polymer segments can interact with each other

$$\langle \vec{R}_n^2 \rangle = C_n nl^2 = Nb^2. \quad (6.2)$$

Chapter 6: Polymer Physics Theory, Basic Concepts and DPD

Generally the main properties of an ideal chain are described by equation (6.2). Thus a description of all ideal polymers can be provided by an equivalent freely jointed chain which has the same mean-square end-to-end distance $\langle \bar{R}^2 \rangle$ and the same maximum end-to-end distance $R_{\max} = Nb$ as the actual polymer, with N freely-jointed effective bonds of length b , which is called the Kuhn length.

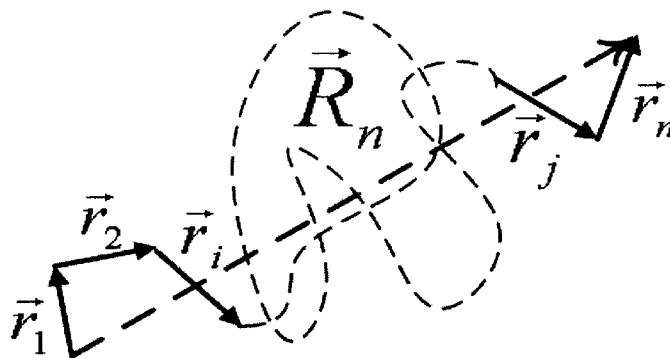


Figure 6.2 Schematic of end-to-end distance of one conformation of a flexible polymer. The vector lines represent sample actual links in the chain and the rest of the contour of the chain is represented by curved dotted line.

6.1.1 Radius of Gyration

Usually it is more convenient, especially for branched or ring polymers, to express the size of polymer by the radius of gyration R_g rather than the end-to-end distance. The

R_g^2 is the average square distance between monomers

$$R_g^2 = \frac{1}{N} \sum_{i=1}^N (\bar{R}_i - \bar{R}_{CM})^2 \quad (6.3)$$

where the polymer's centre of mass is

$$\bar{R}_{CM} = \frac{1}{N} \sum_{i=1}^N \bar{R}_i. \quad (6.4)$$

We can average the square radius of gyration over the ensemble of different allowed conformations and calculate the mean-square radius of gyration as

$$\langle R_g^2 \rangle = \frac{1}{N} \sum_{i=1}^N \langle (\vec{R}_i - \vec{R}_{CM})^2 \rangle = \frac{1}{N^2} \sum_{i=1}^N \sum_{j=1}^N \langle (\vec{R}_i - \vec{R}_j)^2 \rangle. \quad (6.5)$$

Converting the summations into integration and using equation (6.5) for an ideal-linear chain, $\langle (\vec{R}(u) - \vec{R}(v))^2 \rangle = (v-u)b^2$, one obtains the mean-square end-to-end distance of an ideal linear chain as

$$\begin{aligned} \langle R_g^2 \rangle &= \frac{1}{N^2} \int_0^N \int_u^N \langle (\vec{R}(u) - \vec{R}(v))^2 \rangle dv du = \frac{b^2}{N^2} \int_0^N \int_u^N (v-u) dv du \\ &= \frac{Nb^2}{6} = \frac{\langle \vec{R}^2 \rangle}{6}. \end{aligned} \quad (6.6)$$

6.1.2 Freely Rotating and Worm-Like Chain Models

A freely rotating chain model assumes that all bond lengths and bond angles are fixed and all torsion angles are equally likely and independent of each other. The correlations of bond vector \vec{r}_j at bond vector \vec{r}_i are reduced by the factor $(\cos \theta)^{|j-i|}$ due to independent free rotations of $|j-i|$ torsion angles between these two vectors such that $\langle \vec{r}_i \cdot \vec{r}_j \rangle = l^2 (\cos \theta)^{|j-i|}$. We are able to estimate the fast decay of $(\cos \theta)^{|j-i|}$ with the exponential function

$$(\cos \theta)^{|j-i|} = \exp(|j-i| \ln(\cos \theta)) = \exp\left(-\frac{|j-i|}{S_p}\right) \quad (6.7)$$

where $S_p = -1/\ln(\cos \theta)$, is the number of main chain bonds in a persistence segment, which is the scale at which local correlations between bonds vectors decay [84]. Due to steric hindrance to bond rotation, polymer chains are never as flexible as a freely rotating chain model. Assuming a described rapid decay, one can obtain the mean square end-to-end distance of freely rotating chain as

$$\langle \vec{R}_n^2 \rangle = C_n n l^2 = \frac{1 + \cos \theta}{1 - \cos \theta} n l^2. \quad (6.8)$$

Chapter 6: Polymer Physics Theory, Basic Concepts and DPD

The worm-like chain model is a special case of a freely rotating chain model for very small values of the bond angle. This is an appropriate model for very stiff polymers like double stranded DNA for which the flexibility is dependent on the fluctuations of the contour of the chain from a straight line rather than the rotation of bond angles. Estimating $\cos\theta$ for small values of bond angle ($\theta \ll 1$) with the first two terms of the Taylor series, one could find the persistence length or the length of the persistence segment

$$l_p = S_p l \approx l \frac{2}{\theta^2}. \quad (6.9)$$

We can also calculate the corresponding Flory characteristic ratio and Kuhn length for worm-like chain:

$$\begin{aligned} C_n &= \frac{1 + \cos\theta}{1 - \cos\theta} \approx \frac{4}{\theta^2} \\ b &= \frac{l C_n}{\cos\theta/2} \approx l \frac{4}{\theta^2} = 2l_p. \end{aligned} \quad (6.10)$$

For instance the persistence length of double-helical DNA can be $l_p \approx 50\text{ nm}$ and its Kuhn length is $b \approx 100\text{ nm}$ [85, 86]. The worm-like chain is defined as the limits $l \rightarrow 0$ and $\theta \rightarrow 0$ at constant persistence length l_p (constant l/θ^2) and constant chain contour length $R_{\max} = nl \cos(\theta/2) \approx nl$. Using the exponential decay of correlations of bond angles, we can estimate the mean square end-to-end distance of worm-like chain

$$\langle \tilde{R}_n^2 \rangle = 2l_p R_{\max} - 2l_p^2 \left(1 - \exp\left(-\frac{R_{\max}}{l_p}\right) \right). \quad (6.11)$$

Two limits for equation (6.11) can be characterized, namely the ideal chain and rod-like limits.

$$\begin{cases} \langle \bar{R}_n^2 \rangle \approx 2l_p R_{\max} = bR_{\max} & R_{\max} \gg l_p \\ \langle \bar{R}_n^2 \rangle \approx R_{\max}^2 & R_{\max} \ll l_p \end{cases} \quad (6.12)$$

The important difference between freely jointed chains and worm-like chains is the rigidity of the chains in scales smaller than the Kuhn length b , i.e. the worm-like chain is not completely rigid and can fluctuate and bend at length scales shorter than b .

6.1.3 Probability Distribution of End-to-End Distance of an Ideal

Chain

Every possible conformation of an ideal chain can be mapped onto a random walk. A particle making random steps defines a random walk. If the length of each step is constant and the direction of each step is independent of all previous steps, the trajectory of this random walk is one conformation of a freely jointed chain. Hence, random walk statistics and ideal chain statistics are similar [84]. Knowing this similarity, we can easily obtain the one-dimensional probability distribution function for the components of a random walk along each of the three axes in space

$$\begin{aligned} P_{1D}(N, \bar{R}_x) &= \frac{1}{\sqrt{2\pi \langle \bar{R}_x^2 \rangle}} \exp\left(-\frac{\bar{R}_x^2}{2\langle \bar{R}_x^2 \rangle}\right) \\ &= \sqrt{\frac{3}{2\pi Nb^2}} \exp\left(-\frac{3\bar{R}_x^2}{2Nb^2}\right). \end{aligned} \quad (6.13)$$

The above equation is obtained by assuming $\langle \bar{R}^2 \rangle = \langle \bar{R}_x^2 \rangle + \langle \bar{R}_y^2 \rangle + \langle \bar{R}_z^2 \rangle = Nb^2$ and the equivalence of the three Cartesian axes, $\langle \bar{R}_x^2 \rangle = \langle \bar{R}_y^2 \rangle = \langle \bar{R}_z^2 \rangle = Nb^2/3$. Also, it is important to note that in extracting equation (6.13), some approximations are used, and we shall term this equation a Gaussian approximation. Since the three components of a three-dimensional random walk along the three Cartesian coordinates are independent of

Chapter 6: Polymer Physics Theory, Basic Concepts and DPD

each other, the three-dimensional probability distribution function is the product of the three one-dimensional distribution functions

$$P_{3D}(N, \vec{R}) = \left(\frac{3}{2\pi Nb^2} \right)^{3/2} \exp \left(-\frac{3\vec{R}^2}{2Nb^2} \right). \quad (6.14)$$

The above equation shows the possibility of finding polymer of N segment to achieve the conformation with end-to-end vector of \vec{R} (also see Figure 6.3). It is obvious that the probability distribution of \vec{R} is Gaussian which is natural result of random walk theory. We can also derive the equation (6.14) using the central limit theorem that defines the normal distribution (Gaussian distribution) of end-to-end vector.

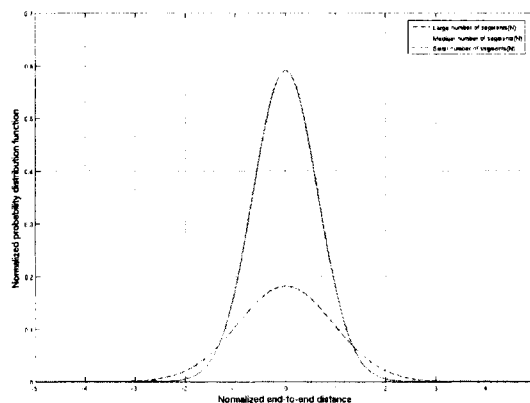


Figure 6.3 Normalized distribution function of end-to-end distances of an ideal chain with different number of segments.

6.1.4 Free Energy and Entropic Elasticity of an Ideal Chain

The entropy of a freely jointed chain of N monomers with end-to-end vector \vec{R} is

$$S(N, \vec{R}) = k_B \ln \Omega(N, \vec{R}) \quad (6.15)$$

Chapter 6: Polymer Physics Theory, Basic Concepts and DPD

where k is the Boltzmann constant and $\Omega(N, \vec{R})$ is the number of configurations of the chain with N monomers which has the end-to-end vector of \vec{R} . Using the definition of the probability distribution function

$$\Omega(N, \vec{R}) = P_{3D}(N, \vec{R}) \int \Omega(N, \vec{R}) d\vec{R} \quad (6.16)$$

and substituting equation (6.14) to equations (6.15) and (6.16), one can obtain the entropy of an ideal chain

$$\begin{aligned} S(N, \vec{R}) &= -\frac{3}{2} k_B \frac{\vec{R}^2}{Nb^2} + S(N, 0), \\ S(N, 0) &= \frac{3}{2} k_B \ln \left(\frac{3}{2\pi nb^2} \right) + k_B \ln \left(\int \Omega(N, \vec{R}) d\vec{R} \right). \end{aligned} \quad (6.17)$$

We can find the Helmholtz free energy of the chain which is $F(N, \vec{R}) = U(N, \vec{R}) - TS(N, \vec{R})$, where T is the absolute temperature and U is the energy of an ideal chain which is independent of the end-to-end vector because the monomers have no interaction energy. The free energy can be simplified to

$$F(N, \vec{R}) = \frac{3}{2} k_B T \frac{\vec{R}^2}{Nb^2} + F(N, 0) \quad (6.18)$$

where $F(N, 0) = U(N, 0) - TS(N, 0)$ is the free energy of the chain when both ends are at the same point. It is crucial to note that the largest number of chain configurations corresponds to zero end-to-end vector. The number of conformations decreases with increasing end-to-end vector, leading to the decrease of polymer entropy and increase of its free energy [84]. The quadratic dependence of free energy with end-to-end vector implies that the entropic elasticity of an ideal chain satisfies Hooke's law. This means that if we want to hold a chain at a fixed end-to-end vector \vec{R} we would need a force of

$$\vec{f} = \frac{\partial F(N, \vec{R})}{\partial \vec{R}} = \frac{3k_B T}{Nb^2} \vec{R}. \quad (6.19)$$

Chapter 6: Polymer Physics Theory, Basic Concepts and DPD

The above equation is the Hooke's law for an ideal chain and the term $3kT/Nb^2$ is called the entropic spring constant coefficient of linear dependence of entropic force with respect to end-to-end vector. It becomes harder to elongate polymers when they are stretched because there are fewer possible conformations for larger end-to-end distances. Although other materials like metals and ceramics become softer as temperature is raised (their deformations are due to atomic displacement, i.e. energetic elasticity), polymers become stiffer with increase of temperature due to the entropic nature of their elasticity.

It should be noted that in the derivation of equation (6.19) we use the Gaussian approximation of probability density function which is only valid for $\langle \vec{R} \rangle \ll (R_{\max} = bN)$. Additionally we can adjust the limit of force to be of order of $k_b T / b$ so that Hooke's law is applicable. Considering the effects of non-linearities will result in more complex formulations. For instance, in a freely jointed chain, the average end-to-end distance corresponding to a given force is [84]

$$\langle \vec{R} \rangle = bN \left[\coth\left(\frac{fb}{k_b T}\right) - \frac{1}{fb / k_b T} \right]. \quad (6.20)$$

It should be noted that the existence of random process in chain models leads to there being no simple analytical solution for the worm-like chain model at all extensions, and finding an accurate solution usually requires computer simulations. The best and earliest model was introduced by Marko and Siggia [87]

$$\frac{fb}{2k_b T} = \frac{\langle \vec{R} \rangle}{R_{\max}} + \frac{1}{4(1 - \langle \vec{R} \rangle / R_{\max})^2} - \frac{1}{4}. \quad (6.21)$$

The Marko-Siggia expression shows convergence to a good solution as $\langle \vec{R} \rangle \rightarrow 0$ or $\langle \vec{R} \rangle \rightarrow R_{\max}$. However, Bouchiat et al. [88] subtracted the Marko-Siggia interpolation formula from the exact numerical solution of the worm-like chain model

Chapter 6: Polymer Physics Theory, Basic Concepts and DPD

and expressed the residual as a seventh-order polynomial leading to an accuracy better than 0.01%

$$\frac{fb}{2k_B T} = \frac{\langle \vec{R} \rangle}{R_{\max}} + \frac{1}{4(1 - \langle \vec{R} \rangle / R_{\max})^2} - \frac{1}{4} + \sum_{i=2}^7 \alpha_i \frac{\langle \vec{R} \rangle}{R_{\max}} \quad (6.22)$$

where the coefficients α_i are $\alpha_2 = -0.5164228$, $\alpha_3 = -2.737418$, $\alpha_4 = 16.07497$, $\alpha_5 = -38.87607$, $\alpha_6 = 39.49944$, and $\alpha_7 = -14.17718$. In Figure 6.4 we have plotted the normalized stretching force ($fb/(k_B T)$) versus the normalized average end-to-end distance $\langle \vec{R} \rangle / R_{\max}$ for a Gaussian chain [equation (6.19)], freely jointed chain [equation (6.20)], and three models of worm-like chain. Also, for a worm-like chain, the exact numerical solution is shown in Figure 6.4 which is obtained from [88]. From this figure we find that for very small extensions, all the models predict the linear elastic characteristics of the Gaussian chain model (Hookean spring). For larger extensions there is significant divergence between the different models. Another criterion which can be observed from Figure 6.4 is that the largest divergence of Marko-Siggia expression from exact solution occurs when $\langle \vec{R} \rangle / R_{\max} \approx 0.5$ and it is around 10%.

Chapter 6: Polymer Physics Theory, Basic Concepts and DPD

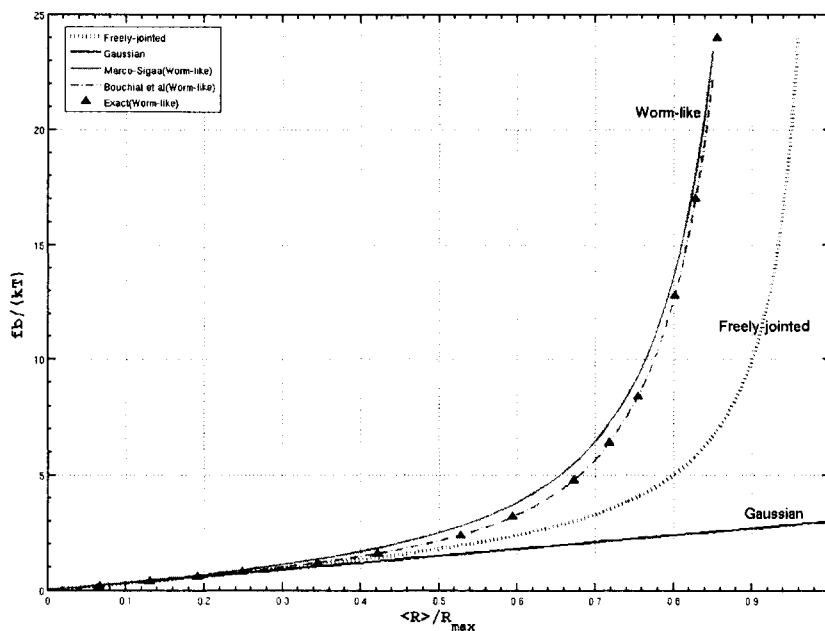


Figure 6.4 Plot of normalized stretching force versus normalized average end-to-end distance for a Gaussian chain equation (6.19), freely jointed chain equation (6.20), and three models of worm-like chain. The data for exact worm-like chain (\blacktriangle) are from [88].

6.2 Non-Ideal Chains (More Realistic Polymers)

In the ideal chain model we assume that the chain is able to fold over itself so that the segments which are far away can occupy the same volume and this is due to the assumption of random walk (flight) motion of monomers without any limitations. This model of ideal chain is not completely true and physically impossible since each monomer occupies only its own position in the space. If we impose the limitation such that each monomer can move randomly but cannot visit the same position more than once, we attain the real chain's conformation. The restraint that real chains cannot cross each other is called self-avoiding walk and the polymer thus represented is often called the excluded volume chain. Assuming no overlapping restriction we would expect the end-to-end distance distribution to be shifted to larger values. The excluded volume

Chapter 6: Polymer Physics Theory, Basic Concepts and DPD

effects and correspondingly the type of liquid in which the polymer is dissolved cause the ends of a polymer chain in a solution to be further apart (on average) or less away (shrunk) than they would be were there no excluded volume effects.

The formulation for the size of the real chains can be derived with some corrections in probability distribution function as in [89] for simple cases, or using more complicated mean-field calculations of Flory [90]. The derivation of these distributions is beyond the scope of current work and here we just summarize the most important final results for different cases from [84]. Following we consider five cases for different conditions of solvents which directly affect the chain conformation.

$$\text{Athermal solvents} \Rightarrow R = bN^{1/2}$$

$$\text{Good solvents} \Rightarrow R = b \left(\frac{EV}{b^3} \right)^{2\nu-1} N^\nu$$

$$\theta\text{-solvents} \Rightarrow R = bN^\nu$$

$$\text{Poor solvents} \Rightarrow R = |EV|^{-1/3} b^2 N^{1/3}$$

$$\text{Non-solvents} \Rightarrow R = bN^{1/3}$$

We can have the exact same situation as the ideal chain conformation when the attraction between monomers exactly balances the whole effects of hard core repulsion. Thus the net excluded volume effect is zero, $EV=0$, and the coil size behaves like its ideal conformation and this corresponds to cases involving θ -solvents. The temperature at which the solvent adjusts the polymer to its ideal size is called the θ -temperature. The chain size is defined as in equation (6.2), i.e. $R = bN^{1/2}$.

Chapter 6: Polymer Physics Theory, Basic Concepts and DPD

In the situation where the attraction between the monomers is unable to overcome the hard core repulsion, we will have the positive excluded effects and the chain will tend to expand more than its ideal conformation. This usually occurs when the temperature is higher than the θ -temperature, where the chain is at its ideal adjustment

$$R = b \left(\frac{EV}{b^3} \right)^{2\nu-1} N^\nu. \quad (6.23)$$

In an athermal solvent the interactions between monomers of the chain are identical to their interactions with the surrounding solvent and as a consequence the net interactions between the monomers are zero but there remains hard core repulsion between the monomers. In this situation the excluded volume is independent of temperature and is constant, $EV = b^3$, and the chain only has the condition of self-avoiding walk of the monomers. The size of the chain can be thus estimated by

$$R = bN^\nu. \quad (6.24)$$

In the case of poor solvent and below the θ -temperature, the attraction between the monomers is so strong compared to hard-core repulsion, and the excluded volume is negative such that the chain collapses into a small globule of size

$$R = |EV|^{-1/3} b^2 N^{1/3}. \quad (6.25)$$

If the temperature goes far below the θ -temperature, we will have the pure attraction the between monomers and the excluded volume is in its higher negative value $EV = -b^3$. This lowest limiting case is termed non-solvent and the chain takes its fully collapsed conformation in this condition

$$R = bN^{1/3}. \quad (6.26)$$

We note from the results that the good and poor solvents are better suited for very long chains, while for the short chains it is the ideal chain condition that is better suited.

Chapter 6: Polymer Physics Theory, Basic Concepts and DPD

If we look at all the above formulations for different solvent conditions we see the contribution of the exponent parameter ν which is usually termed the characteristic critical exponent. The scaling theory for polymer solutions states that all physical properties and especially the polymer size can be expressed by the simple power law $R \approx N^\nu$. For the case of good solvent, Flory [91] found the exponent value using statistical scaling arguments, and obtained

$$\nu = \frac{3}{d+2} \quad (6.27)$$

where d is the spatial dimension. Equation (6.27) shows a good agreement with other simulation and experimental techniques. In Table 6-1 we summarize the most important exponent values for two and three dimensional chain conformation under two solvent conditions. Also, for θ -solvents we can use the same exponent as the good solvent.

Table 6-1 Two and three dimensional critical exponent for different solvent conditions.

Solvent condition	Athermal solvents	Good solvents (Flory's Formula)	Good solvents (Simulation [92])
Exponent value ν 2D	0.5	0.75	0.77
Exponent value ν 3D	0.5	0.6	0.588

6.3 Coarse-Grained DPD Simulation of Polymer Chain

When investigating more into polymeric systems and especially biological ones like DNA strands, we find that both micro and macro dimensions are involved in the evolution of these systems. For instance the contour length of λ -phage DNA is $L = 21 \mu m$ while its diameter is only few nanometers (around $2 nm$). There are thus different length and time scales involved. This complexity requires a coarse-grained

Chapter 6: Polymer Physics Theory, Basic Concepts and DPD

approach which ignores details of the polymer's conformation under a certain length (for example the Kuhn length), to efficiently simulate the conformational changes. There are two methods for modeling chains in the coarse level; one is the bead-rod chain which models each segment of polymer with rigid links of fixed length (Kuhn length) and the other is the bead-spring chain. In the following section we introduce the bead-spring chain model which is a coarser model for polymer chains and has more flexibility than the bead-rod model.

6.3.1 DPD Polymeric Models

An attractive method for the simulation of polymers is the DPD. Though this methodology has a good consistency with available experimental data, there still exists certain difficulties when simulating the polymer's rheology with DPD. In [9] the DPD was applied for studying the polymer's static exponent where the polymer was modeled as a stiff and Hookean linear spring and the exponent value was found to be $\nu = 0.52$. Later in [93], effects of solvent quality on the scaling of the polymer radius of gyration and its dynamical relaxation time were investigated and for a three dimensional situation, the static exponent was found to be $\nu = 0.6$. Groot and Warren [6] mapped the DPD parameters to real water using the velocity Verlet algorithm with $\Delta t = 0.04$ and in addition they obtained the Flory-Huggins parameter for different polymer sizes using the Hookean spring model. Employing the same time integrating scheme of [6], Groot et al. [11] simulated block co-polymer separation using DPD. In [94], the Hookean spring force was used to find the diffusion coefficient and the scaling exponent for two conditions of polymers in dilute solution and polymers in melt.

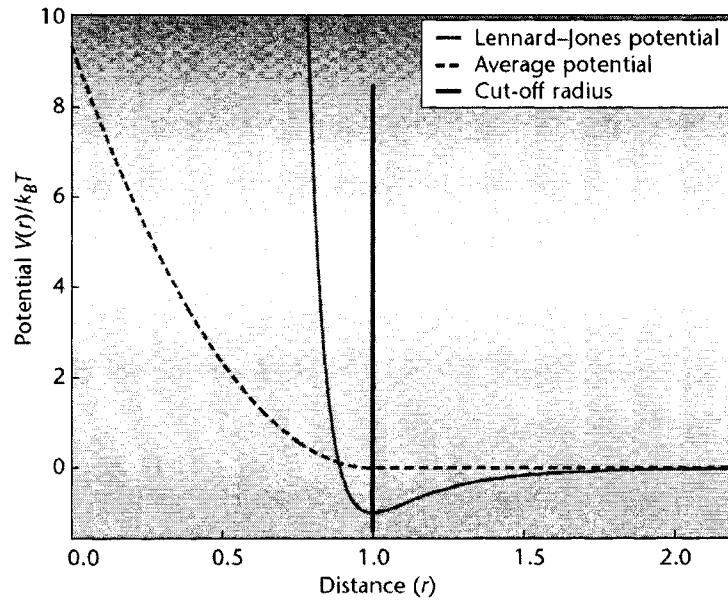


Figure 6.5 Lennard-Jones potential and the soft-repulsive potential after averaging. Figure extracted from [95].

As we have mentioned in Chapter 4, the DPD equations are stochastic and nonlinear because of the velocity dependence of the dissipative force. In addition to the difficulties of finding appropriate time integrating scheme for this stochastic nature of the DPD algorithm, we may face other problems when simulating complex fluids. In particular, the use of the Lennard-Jones potential for each bead pair requires smaller time step compared to soft repulsion of typical DPD particles (see Figure 6.5). Due to the presence of both soft and hard potentials, Symeonidis et al. [95] proposed the use of time-staggered algorithms to study the polymeric physical quantities (such as end-to-end distance or radius of gyration) efficiently.

In addition to the conservative, dissipative and random standard DPD interactions for every particle in the flow, the polymer chains are subjected to intra-polymer forces (for each bead pair). The literature [96] suggests that we can model these forces using

Chapter 6: Polymer Physics Theory, Basic Concepts and DPD

combinations of the following potential types U , and accordingly find the pairwise forces by $F_{bead}(r_{ij}) = -\nabla U(r_{ij})$.

Lennard-Jones

$$\frac{U_{LJ}}{4k_B T} = \begin{cases} \left(\left(L/r_{ij} \right)^{12} - \left(L/r_{ij} \right)^6 + 1/4 \right) & : \text{for } (L/r_{ij})^6 < 2 \\ 0 & : \text{otherwise.} \end{cases} \quad (6.28)$$

Hookean spring

$$U_{Hooke} = \frac{\kappa}{2} |\mathbf{r}_{i+1} - \mathbf{r}_i|^2 \quad \text{for } i = 1, 2, \dots, N-1. \quad (6.29)$$

Fraenkel stiff spring

$$U_{STIFF} = \frac{\kappa}{2} (|\mathbf{r}_{i+1} - \mathbf{r}_i| - r_{eq})^2 \quad \text{for } i = 1, 2, \dots, N-1. \quad (6.30)$$

Finitely extensible nonlinear elastic (FENE) spring

$$U_{FENE} = -\frac{\kappa}{2} r_m^2 \ln \left(1 - \frac{|\mathbf{r}_{i+1} - \mathbf{r}_i|^2}{r_m^2} \right) \quad \text{for } i = 1, 2, \dots, N-1. \quad (6.31)$$

Worm-like chain (WLC)

$$\mathbf{F}_{ij}^{WLC} = -\frac{k_B T}{4\lambda_p^{eff}} \left[\left(1 - \frac{r_{ij}}{L_{sp}} \right)^{-2} + \frac{4r_{ij}}{L_{sp}} - 1 \right] \mathbf{e}_{ij}. \quad (6.32)$$

The Lennard-Jones potential cannot be used solely for interbead interactions since it creates pure repulsive force which causes the chain to break, so we need to combine it with other attractive potentials. It is interesting to note that when using the combined Lennard-Jones potential with some other spring forces, we may capture the excluded volume effects solely through the pairwise chain interactions without direct interference of the solution. In all of the above equations, κ is the spring constant which has the unit of $k_B T / r_c^2$, taking different proportionality factors of this unit for different problems.

Chapter 6: Polymer Physics Theory, Basic Concepts and DPD

The Fraenkel spring has a finite equilibrium length r_{eq} below which the spring will exert a repulsive force, and above which the spring exerts an attractive force. This is in contrast to the Hookean spring potential which always produces a pure attractive interbead force. The r_m in the FENE spring potential, see equation (6.31), is the maximum extension length of the chain beyond which the attraction becomes infinite. Equation (6.32) describes the worm-like chain pairwise interaction as it was described earlier in more detail in section 6.1.2. Here similar to l_p , λ_p^{eff} is the effective persistence length which is the measure of chain's stiffness and L_{sp} is the maximum length of each chain segment. It is interesting to note the similarity in form of equation (6.22) for a comprehensive polymer stretching model and equation (6.32) for the bead-spring model. The analogy of these two equations comes from replacing the long chain to smaller chains extracted by the relation of each of the beads with the entire contour length, i.e.

$$\frac{r_{ij}}{L_{sp}} \approx \frac{\langle \vec{R} \rangle}{R_{max}}.$$

We can implement any of the above mentioned potentials at simple equilibrium state and investigate the scaling laws. Selecting the appropriate model which matches well with the experimental data of our application is essential. Figure 6.6 shows the freely suspended chain in a typical solvent using the DPD simulation with the WLC bead spring forces.

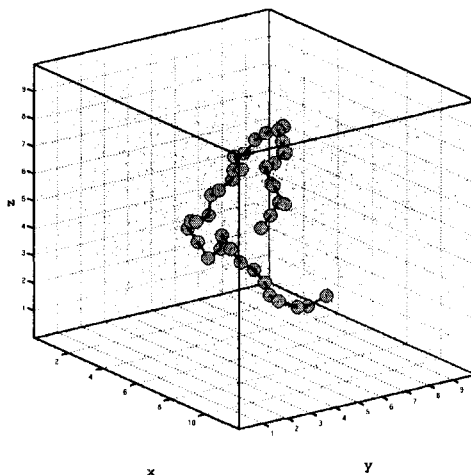


Figure 6.6 A 40 bead 3D polymer chain at equilibrium state in a periodic box of solution.

6.3.2 DPD Simulation of Worm-Like Chain in a Dilute Solution and Scaling Laws

In this section we investigate the dynamics of single polymer chains of different sizes in a dilute solution. We used the DPD to simulate two dimensional cases and different parameters are explored to determine the scaling exponent as a measure of excluded volume effects. Also, different solvent conditions are examined in order to achieve real chains behaviors. Since our application in the next chapter is related to DNA migration we are more interested in the simulation of WLC which is one of the best models that can capture DNA physical conformations.

Since all the simulations we carried out involve the WLC and no LJ potential is involved, there is no need to use any time staggered scheme. For time integration and especially choice of time step, we may face difficulties if it is not properly selected mainly during the initialization of the chain and also for fast changing field phenomenon, which may arise in our DNA application in the next chapter. As we are using the WLC force of equation (6.32) and when each segment length approaches near maximum spring

Chapter 6: Polymer Physics Theory, Basic Concepts and DPD

length L_{sp} , the spring force may become too large such that the net exerted force by the surrounding particles is unable to compensate in kind. In this situation if the time step is not decreased the distance between the beads of the chain would drastically increase and the chain may break. In order to overcome this, we select a main time step of $(\Delta t)_{main} = 0.02$ and dynamically refine it according to the current chain segment length r_{ij} , in the following manner:

If $r_{ij} \leq 0.85 L_{sp}$ then $\Delta t = (\Delta t)_{main}$.

If $0.85 < r_{ij} \leq 0.9 L_{sp}$ then $\Delta t = (\Delta t)_{main} / 2$.

If $0.9 < r_{ij} \leq 0.95 L_{sp}$ then $\Delta t = (\Delta t)_{main} / 4$.

If $0.95 L_{sp} < r_{ij}$ then $\Delta t = (\Delta t)_{main} / 8$ and $F_{ij}^{WLC} = F_{ij}^{WLC} |_{(r_{ij}=0.95 L_{sp})}$.

We track the length of every segment of the chain and we use the time step associated with the longest segment for calculating the evolution of all particles in the system.

Another issue is proper application of the periodic conditions for the chain beads and how these beads interact with each other and other solvent particles. This issue can be handled by storing the position of the chain beads in two different coordinates. The first is the unmapped or real chain coordinate which allows us to calculate the interbead forces. The second is the coordinate similar to the coordinate of all other particles which the polymer beads can freely move in and can have the periodic conditions similar to the solvent particles. The latter is helpful for estimating the interactions of polymer beads with solvent particles and we shall term these beads as ghost particles. It should be noted that both mentioned coordinates are identical when the chain beads are in dimensions

Chapter 6: Polymer Physics Theory, Basic Concepts and DPD

less than the box sizes. In Figure 6.7 the schematic representation of both real and ghost chain particles is shown.

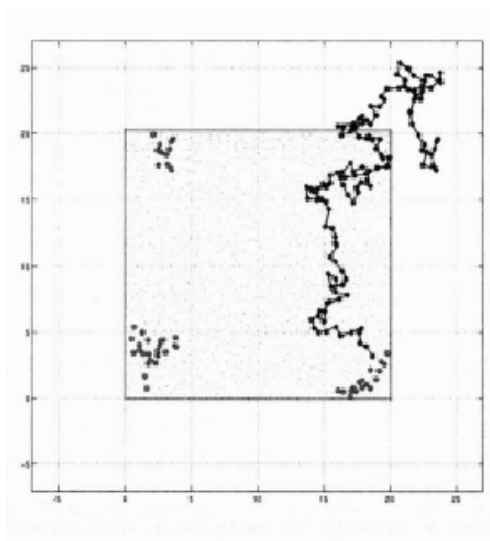


Figure 6.7 The 2D representation of a 128 bead chain (blue balls) in a 20×20 simulation box. The yellow crossed circles show the positions of the ghost chain beads. The small green dots represent the solvent particles.

To explore the effects of different parameters on the scaling of the chain, we shall examine two dimensional cases since it takes significantly less computational time than 3D simulations. The dilute solution condition is mimicked by immersing the single chains in ocean of DPD particles within a periodic box of size 10 in each direction. Using the described periodic chain methodology, the effect of box size is negligible. We choose the WLC of equation (6.32) in all of the cases and the corresponding static exponent values ν for both radius of gyration and end-to-end distance, are computed for each case, using 5, 10, 20, 50 and 100 bead chains. The main DPD simulation parameters (the 2D run parameters) are listed in Table 6-2. We run simulations for 250,000 time steps and average all quantities over the last 10,000 steps. This large integration time is not necessary for short chains but it is essential for longer chains (100 beads or longer) where the relaxation times are much longer. The scaling exponent is

Chapter 6: Polymer Physics Theory, Basic Concepts and DPD

estimated by fitting a line to first four or five points in log-log plot. We eventually used a 4 point fitting (for 5, 10, 20 and 50 bead chains) since larger simulation time is required for complete relaxation of a 100 bead chain. In addition, the chain temperature absolute error, the ratio $\langle R^2 \rangle / \langle R_g^2 \rangle$ and the chain average contour length per bead L_c are computed. In the following, the 5 point line fitting of radius of gyration is discussed unless otherwise stated.

In order to verify our DPD source code we simulate one 3D case with parameters similar to [96] and the results are shown in Figure 6.8. We obtained the exponent value of $\nu = 0.5521$ which is in a very good agreement to the value $\nu = 0.5516$ in [96].

First we increase the persistence length from $\lambda_p^{eff} = 0.05$ to $\lambda_p^{eff} = 0.15$ to obtain better scaling exponent values as represented in Figure 6.9 and Figure 6.10. Increasing the persistence length causes a rise in chain temperature so we correspondingly increased the maximum segment length to $L_{sp} = 1.5$ (see Figure 6.11 and Figure 6.12). We analyzed Figure 6.9 to Figure 6.12 and found a very logical trend that increasing maximum segment length L_{sp} or persistence length λ_p^{eff} caused the chain beads to have more space to interact with solvent particles and this results in better excluded volume effects as the exponent values rise from $\nu = 0.6994$ to $\nu = 0.7304$.

Next we examined the solvent quality by altering the polymer fluid repulsion parameter from $a_{pf} = 0.5a_{ff}$ to $a_{pf} = 1.25a_{ff}$. From the results in Figure 6.13 to Figure 6.15 we observe that the scaling of radius of gyration decreases from $\nu = 0.7425$ to $\nu = 0.4720$ for 4 points line fittings. This is due to the fact that as we increase a_{pf} the solvent particles are repulsed from the chain and the chain tends to fold over itself and collapse.

Chapter 6: Polymer Physics Theory, Basic Concepts and DPD

On the other hand, decreasing a_{pf} leads to more attraction of the chain segments toward the solvent and thus better expansion of the polymer segments into the fluid and this enhances the excluded volume effects.

Table 6-2 DPD simulation parameters for 2D simulation.

$k_B T$	ρ_f	a_{ff}	r_c	σ	dt
1	4	18.75	1	3	0.02

Finally we define S as the minimum number of neighboring polymer beads that could sense the original conservative bead-bead force, i.e. when $|i - j|_{pp} \geq S$, we set different values for the polymer-polymer repulsion parameter a_{pp} . This allows us to alter the bead-bead interaction for different distances along the chain segments and as a result the neighboring segments may be able to fold softly while remote beads expel each other strongly. For instance, in the case of Figure 6.16, setting $S = 2$ and $a_{pp} = 2a_{ff}$ result in better scaling laws $\nu = 0.7685$ for 4 point radius gyration fitting.

One remarkable observation from all above results is the ratio $\langle R^2 \rangle / \langle R_g^2 \rangle$ which apparently can be used as another measure of chain discrepancy from the ideal chain condition where $\langle R^2 \rangle / \langle R_g^2 \rangle = 6$ according to equation (6.6). From the results we observe that when the scaling laws exponent values are improved, the values of this ratio are greater than 6.

Chapter 6: Polymer Physics Theory, Basic Concepts and DPD

5 points $\langle \hat{R}^2 \rangle$ base	4 points $\langle \hat{R}^2 \rangle$ base	5 points $\langle \hat{R}^2 \rangle$ base	4 points $\langle \hat{R}^2 \rangle$ base
0.5521	0.5439	0.5759	0.5707

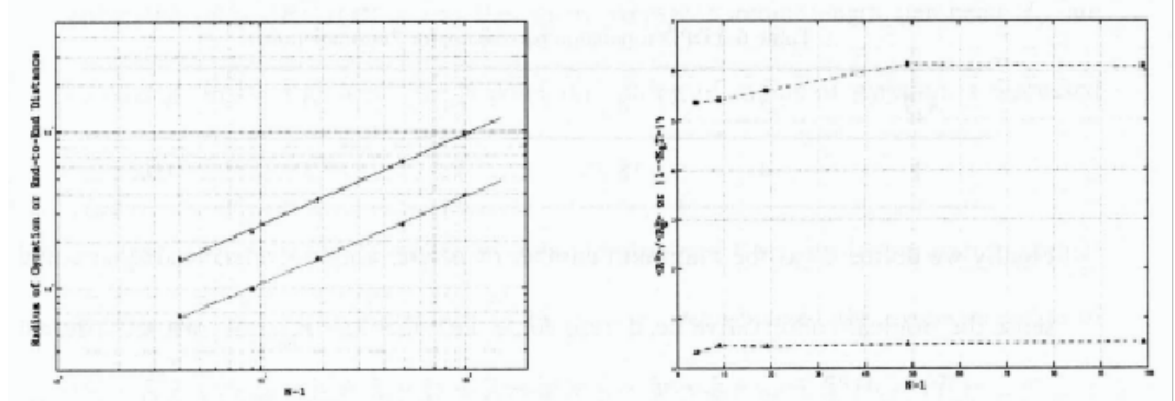


Figure 6.8 Left: Scaling of radius of gyration (red) or end-to-end distance (blue). Right: Ratio $\frac{\langle R^2 \rangle}{\langle R_g^2 \rangle}$ (red) and the chain temperature absolute error (blue). 3D Simulation parameters: $L_{sp} = 2$, $\lambda_p^{eff} = 1/7$, $a_{pf} = a_{ff}$, $k_B T = 0.2$, $L_c = 0.695$.

5 points $\langle \hat{R}^2 \rangle$ base	4 points $\langle \hat{R}^2 \rangle$ base	5 points $\langle \hat{R}^2 \rangle$ base	4 points $\langle \hat{R}^2 \rangle$ base
0.6994	0.7325	0.6313	0.6827

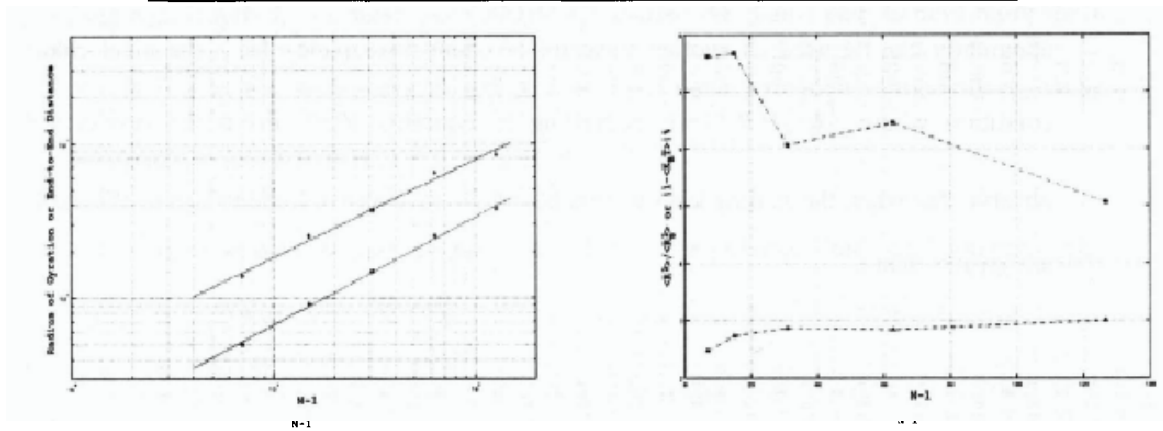
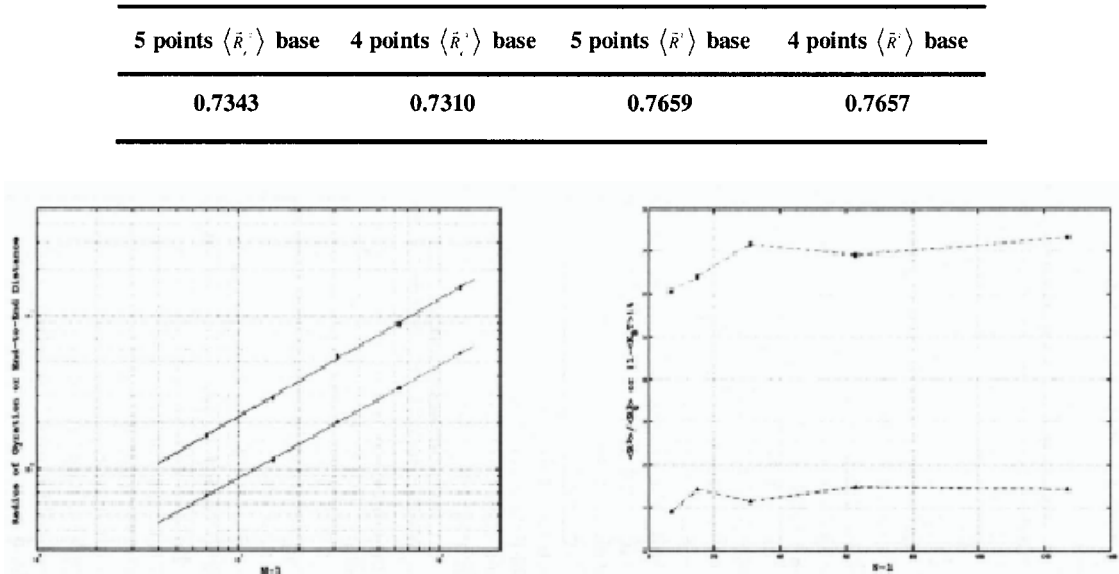
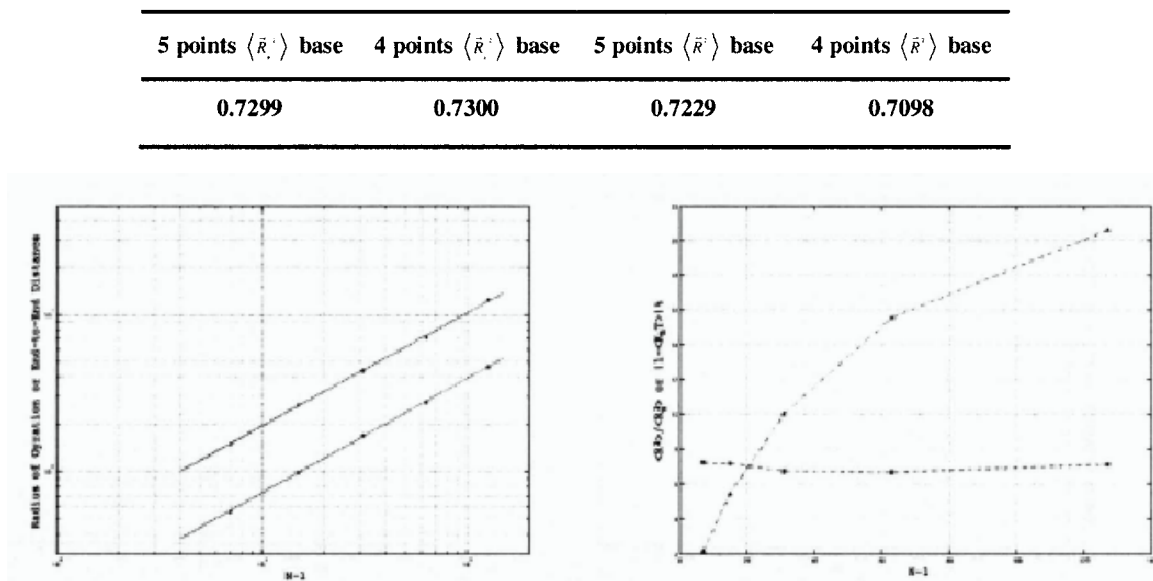


Figure 6.9 Left: Scaling of radius of gyration (red) or end-to-end distance (blue). Right: Ratio $\frac{\langle R^2 \rangle}{\langle R_g^2 \rangle}$ (red) and the chain temperature absolute error (blue). Simulation parameters: $L_{sp} = 0.5$, $\lambda_p^{eff} = 0.05$, $a_{pf} = a_{ff}$, $L_c = 0.253$.

Chapter 6: Polymer Physics Theory, Basic Concepts and DPD



Chapter 6: Polymer Physics Theory, Basic Concepts and DPD

5 points $\langle \bar{R}_g^2 \rangle$ base	4 points $\langle \bar{R}_g^2 \rangle$ base	5 points $\langle \bar{R}^2 \rangle$ base	4 points $\langle \bar{R}^2 \rangle$ base
0.7304	0.7196	0.7673	0.772

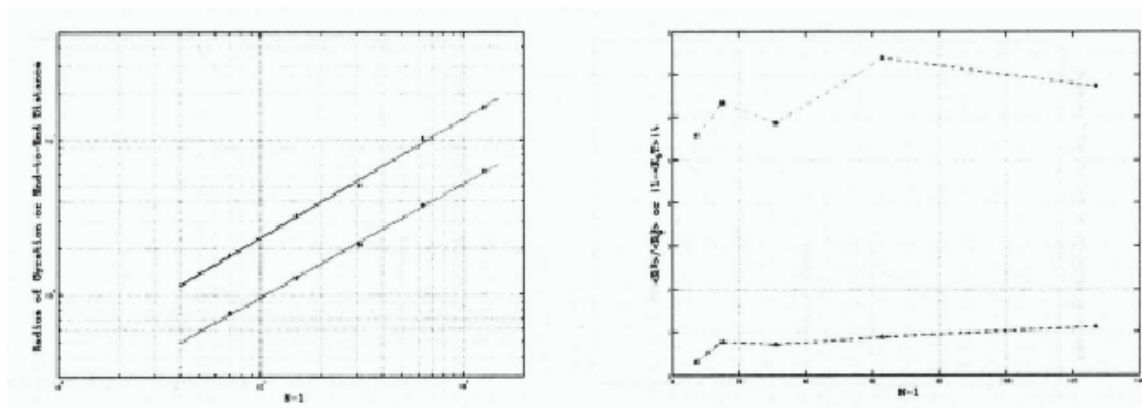


Figure 6.12 Left: Scaling of radius of gyration (red) or end-to-end distance (blue). Right: Ratio $\frac{\langle R^2 \rangle}{\langle R_g^2 \rangle}$ (red) and the chain temperature absolute error (blue). Simulation parameters: $L_p = 1.5$, $\lambda_p^{eff} = 0.15$, $a_{pf} = a_{ff}$, $L_c = 0.525$.

5 points $\langle \bar{R}_g^2 \rangle$ base	4 points $\langle \bar{R}_g^2 \rangle$ base	5 points $\langle \bar{R}^2 \rangle$ base	4 points $\langle \bar{R}^2 \rangle$ base
0.7312	0.7257	0.7357	0.7423

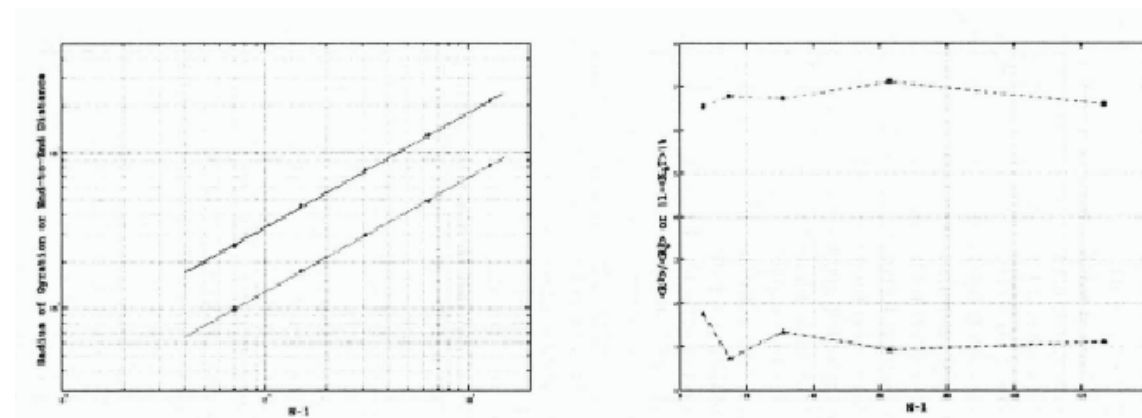


Figure 6.13 Left: Scaling of radius of gyration (red) or end-to-end distance (blue). Right: Ratio $\frac{\langle R^2 \rangle}{\langle R_g^2 \rangle}$ (red) and the chain temperature absolute error (blue). Simulation parameters: $L_p = 1.5$, $\lambda_p^{eff} = 0.15$, $a_{pf} = 0.75a_{ff}$, $L_c = 0.613$.

Chapter 6: Polymer Physics Theory, Basic Concepts and DPD

5 points $\langle \tilde{R}_g \rangle$ base	4 points $\langle \tilde{R}_g \rangle$ base	5 points $\langle \tilde{R} \rangle$ base	4 points $\langle \tilde{R} \rangle$ base
0.7301	0.7425	0.7364	0.7657

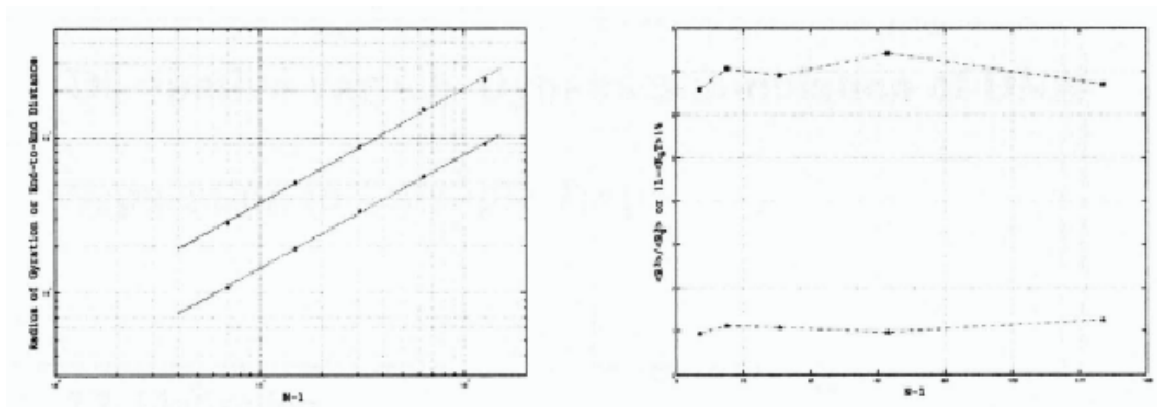


Figure 6.14 Left: Scaling of radius of gyration (red) or end-to-end distance (blue). Right: Ratio $\frac{\langle R^2 \rangle}{\langle R_g^2 \rangle}$ (red) and the chain temperature absolute error (blue). Simulation parameters: $L_{sp} = 1.5$, $\lambda_p^{eff} = 0.15$, $a_{pf} = 0.5a_{ff}$, $L_c = 0.667$.

5 points $\langle \tilde{R}_g \rangle$ base	4 points $\langle \tilde{R}_g \rangle$ base	5 points $\langle \tilde{R} \rangle$ base	4 points $\langle \tilde{R} \rangle$ base
0.4664	0.4720	0.3726	0.3863

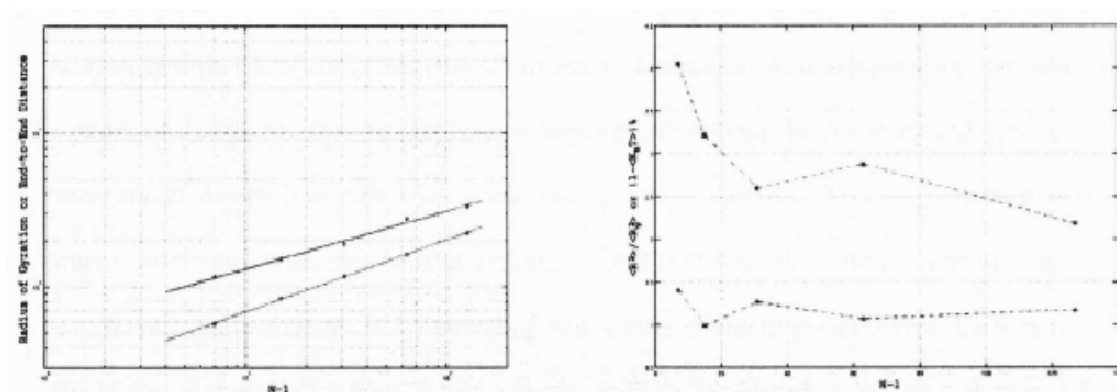


Figure 6.15 Left: Scaling of radius of gyration (red) or end-to-end distance (blue). Right: Ratio $\frac{\langle R^2 \rangle}{\langle R_g^2 \rangle}$ (red) and the chain temperature absolute error (blue). Simulation parameters: $L_{sp} = 1.5$, $\lambda_p^{eff} = 0.15$, $a_{pf} = 1.25a_{ff}$, $L_c = 0.485$.

Chapter 6: Polymer Physics Theory, Basic Concepts and DPD

5 points $\langle \tilde{R}_g \rangle$ base	4 points $\langle \tilde{R}_g \rangle$ base	5 points $\langle \tilde{R} \rangle$ base	4 points $\langle \tilde{R} \rangle$ base
0.7178	0.7685	0.6807	0.7929

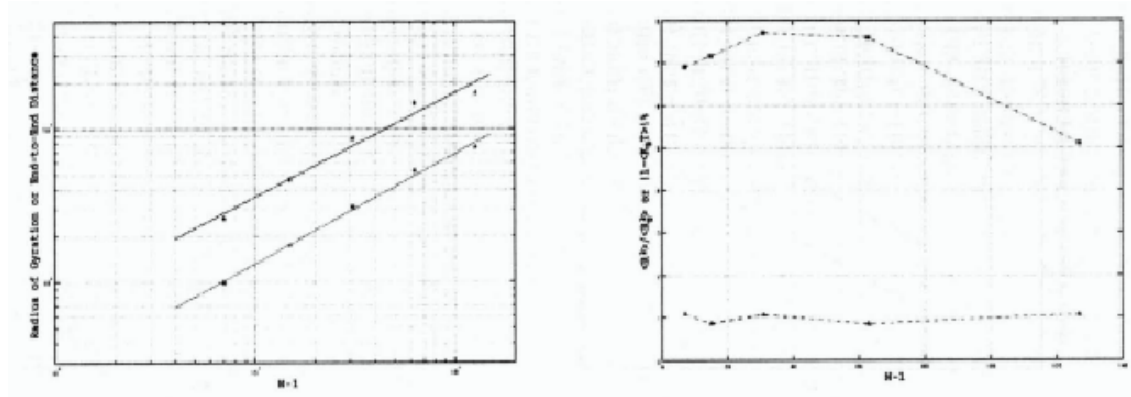


Figure 6.16 Left: Scaling of radius of gyration (red) or end-to-end distance (blue). Right: Ratio $\frac{\langle R^2 \rangle}{\langle R_g^2 \rangle}$ (red) and the chain temperature absolute error (blue). Simulation parameters: $L_{sp} = 1.5$, $\lambda_p^{eff} = 0.15$, $a_{pf} = a_{ff}$, $L_c = 0.566$, $S = 2$, $a_{pp} = 2a_{ff}$.

Chapter 7

Dissipative Particle Dynamics Simulation of DNA

Separation in Entropic Trap

7.1 Motivation

Microfluidics and more recently Nanofluidics are advancing fields traversing over vast areas of engineering, physics, chemistry and biotechnology. More importantly, micro/nano devices are fabricated in order to carry out highly efficient as well as simultaneous analysis of particles, molecules or cells such as in genomic, proteomic, and metabolic applications in biotechnology. In addition to the natural complexity of these devices (in terms of time and length scales) there may involve geometrical complexity as well as suspension of different particles or macro molecules. Achieving appropriate and optimized design for specific application requires advancements of the related electro-mechanical devices, in terms accuracy and speed of analysis. This development of micro- and nano-electromechanical systems (MEMS/NEMS) is leading to the need for continuous improvements in the modeling approaches. Numerical simulation is a way to model these complex systems, which usually involves simulation of coupled electrical, mechanical, thermal and fluid domains.

Chapter 7: DPD Simulation of DNA Separation in Entropic Trap

Here our focus is on these micro/nano channel devices, consisting of many entropic traps, which are designed and fabricated for the separation of long DNA molecules. The channel comprises narrow constrictions and wider regions that cause size-dependent trapping of DNA strands at the onset of a constriction. This process creates electrophoretic mobility differences, thus enabling efficient separation without the need for gel matrices or pulsed electric fields [1-3]. Simulation and in particular numerical simulation is an efficient way to investigate the complex flow in the related electro-mechanical devices and to understand the underlying physics and chemistry of the flow characteristics. For the purpose of simulation we choose the Dissipative Particle Dynamics (DPD) method, which is an appropriate mesoscale simulation approach due not only to its relatively larger time and length scales (compared to molecular dynamics) but also its ability to model rheology of complex systems with relative ease compared other mesoscale techniques.

7.2 Entropic Trapping – Theory and Experiment

7.2.1 Experimental background

DNA separation is important for various biological analyses, such as DNA fingerprinting and genome sequencing. Gel electrophoresis is the standard method for separation of DNA by length. However, it is efficient only for DNA molecules up to about 40kbp (kilo base pairs), where beyond this limit mobility difference is diminished. Slab gel pulsed-field gel electrophoresis (PFGE) can be used to separate longer (a few mbp) double-stranded DNA (dsDNA), but in addition to the length limits the process usually takes several days if not weeks. Advances in the field of micro-total analysis systems (μ -TAS) and especially the lab-on-a-chip devices provide many researchers with the

Chapter 7: DPD Simulation of DNA Separation in Entropic Trap

capability to propose novel separation mechanisms using these micro- and/or nano-fluidic devices. Turner [97] presented a device capable of separating DNA molecules according to their length. This device consists of pillar-free and pillared regions. A dense matrix of nano-pillars each with a diameter of 35nm, and spacing of 160nm is fabricated in the pillared region. When the driving electric field is applied, DNA molecules are forced into the pillared region where they are stretched to fit nano-channels inside the pillar matrix. When an entire small molecule enters the pillar matrix and only part of a large molecule enters, the electric field is turned off. The large molecule will recoil back in the pillar-free region because of the tendency to maximize its conformational entropy while the small molecule remains inside the matrix due to uniform entropy. In this manner, molecules of different lengths can be separated. Bakajin [98] devised a micro-chamber with hexagonal array of pillars 2 μ m wide where transverse pulsed electrical fields are applied alternatively along two axes of the array, separated by 120 degrees. Shorter molecules move faster in the array because they spend less time to reorient themselves along the axis of the field and longer molecules use most of the pulse period to align entirely to the axis of the field. Huang [99] applied a similar concept and fabricated a DNA prism where DNAs of different sizes are forced to follow different routes inside the micro-structured sieving matrix under an asymmetric pulsed electric field.

For efficient separation without the use of gel matrices or pulsed electric fields, Han et al. [1-3] designed and fabricated an entropic trapping array, which consists of alternative deep and shallow channels, to separate long DNA molecules (>2 kbp). These silicon based periodic constriction channels are fabricated using standard etching techniques and are enclosed with a Pyrex cover plate as shown in Figure 7.1. The DNA molecules are suspended in the cathode side of the device which is filled with buffer solution before the

Chapter 7: DPD Simulation of DNA Separation in Entropic Trap

start of the separation process. The DNA molecules start traveling from the cathode towards the anode when a dc electric field is applied. The shallow section is much smaller than the moving molecules' radius of gyration such that the molecules must change their conformations and uncoiled in order to pass through the channel. Size-dependent trapping is produced because entropic free energies for DNA molecules of different sizes are different. Thus, the separation is enabled using micro-fabricated entropic trapping array. More recently and following Han's work, Fu [100] introduced an anisotropic nano-filter array (ANA) for continuous-flow bio-molecule separation, where both small (short) and long molecules can be separated through Ogston sieving and entropic trapping mechanism respectively. He similarly demonstrated the separation of proteins with different charges with ANA [101].

7.2.2 Theoretical aspects

In the trapping array device of Han et al. [1-3], the authors observed counterintuitive phenomenon in that *“longer DNA molecules found to escape faster than shorter one”*. They proposed a simple kinetic theory (hernia nucleation in [102] or beachhead scenario in [103]) to obtain more insight into the separation mechanism which we shall review here briefly. Crossing over the thin region of channel requires the overcoming of the entropic barrier. The existence of this barrier is due to the conformational change and uncoiling of the DNA in the gap which reduces the entropic elasticity of the chain. The electric field drives the DNA towards the gap and the high intensity field region of the gap sucks the chain hernias at the entrance of the gap. Entering nucleated hernias with longitudinal length of x inside the gap causes decrease of the total energy by $x^2 E_s$, while the conformational free energy penalty cost is proportional to xT , where E_s is the electric field strength in shallow region and T is the temperature. Therefore the total free

Chapter 7: DPD Simulation of DNA Separation in Entropic Trap

energy difference during the escape process is $\Delta F = xT - x^2 E_s$. In intermediate electric field strengths, the escape of the DNA chain from the shallow region begins when a certain amount of DNA length x_c (critical hernia size [102]) is pushed into the gap longitudinally and at this time the free energy difference reaches its maximum which scales as $\Delta F_{\max} \propto \alpha / E_s$, where α is a constant that depends solely on experimental setup conditions and is not a function of the length of the chains [2]. Assuming the electric field dependence of energy barrier, the probability of escape would be proportional to $\exp(\Delta F_{\max} / k_B T) = \exp(\alpha / E_s k_B T)$ where k_B is the Boltzmann constant. In the condition of intermediate fields and at low E_s the entropic penalty dominates and the DNA chains retard into well while at high E_s the chains pass the energy barrier easily and escape from the trap. The long chains have higher probability of the monomers to contacting the gap region so the rate of escape for long DNA is higher than shorter ones. The authors [2] proposed the following simple expression for the trapping time of the chain:

$$\tau_{trap} = \tau_0 \exp(\alpha / E_s k_B T) \quad (7.1)$$

where τ_0 is dependent on the strength of electric field and chain length. τ_0 decreases as the DNA size increases and this implies the size-selective separation of the designed microfluidic device. Based on equation (7.1), the authors [2] predicted that the trapping time and more specifically the selectivity depend on structural parameters like the depth of well and shallow region and the length of channels as well as the strength of applied electric field and they proved this experimentally.

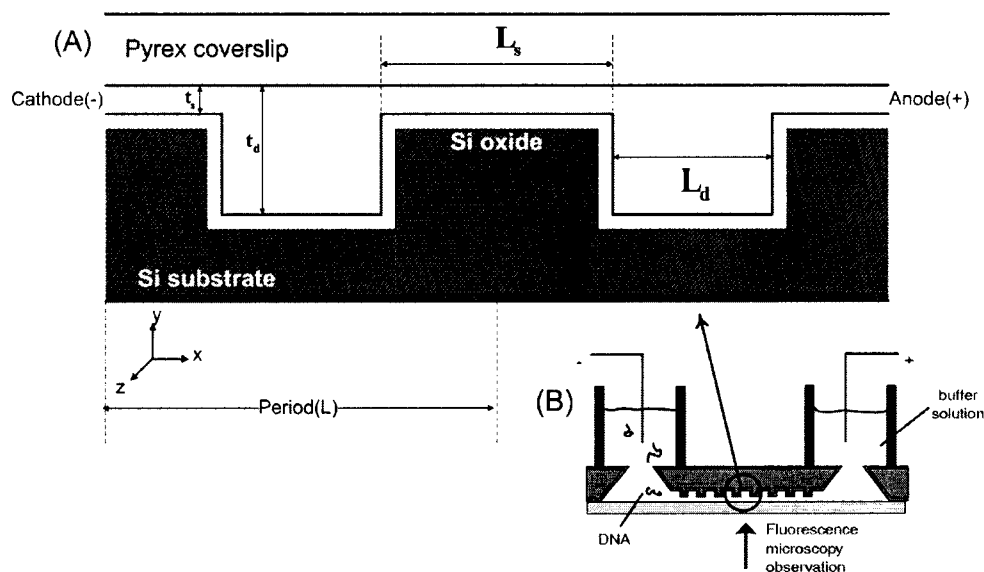


Figure 7.1 schematic diagram of nanofluidic separation device (adapted from Han et al. [1-3])

A: cross-section of two period of the device. B: experimental setup.

7.2.3 Numerical Simulation

Besides some of the mentioned experimental studies, numerical simulation provides an alternative route to study DNA separation processes which involve different time and length scales. The micro-channels used in the DNA separation have characteristic size from dozens of nanometers to several micrometers. In addition traveling and conformation of DNA in each trap is in the micro-second time scale regime, while the total experimental time has the scale of order of several minutes. Due to the molecular scales involved, direct simulation techniques, such as molecular dynamics (MD), are very expensive, if not completely infeasible. Furthermore, the mechanical properties of DNA are actually physically relevant at mesoscopic scale ($0.1\mu\text{m}$) level and can thus be used for understanding the separation process. Apart from DPD, the Monte Carlo (MC) method and the more widely used Brownian Dynamics (BD) simulation are examples of mesoscopic numerical techniques that have been applied in this area.

Chapter 7: DPD Simulation of DNA Separation in Entropic Trap

Using the Monte Carlo Technique, Tessier et al. [102] simulated the flow of DNA through entropic trap arrays where the polymer is modeled by a lattice model with bond fluctuation. Their results mostly confirmed the qualitative observation of Han et al. [1-3] that longer molecules were trapped for a shorter time due to high probability of hernia nucleation and the deformation of molecules at the gap entrance. However, the trapping time was unexpectedly long in their simulation and it may be due to the discrete lattice chain model. In the Monte Carlo simulation of Chen and Escobedo [104], the free energy barrier for escape ΔF_{\max} as a function of chain length was examined in different electric field regimes and in the intermediated fields ($\Delta F_{\max} \approx k_B T$) they confirmed that trapping lifetime decreases as the chain length increases. In addition they showed that in weak electric fields the main controlling factor in the escape process is $\exp(\Delta F_{\max} / k_B T) = \exp(\alpha / E_s k_B T)$ term while at moderate to strong fields τ_0 is dominant prefactor.

Streek et al. [105] performed BD simulations to model the same process using the chain model with Hookean linear spring force to represent the DNA. They found two key mechanisms which contribute to longer trapping lifetimes for smaller molecules, namely the probabilistic delayed entry of the short chains at the entrance of constriction and the diffusion of small molecules to the corner of the well. The latter may be explained by the shorter chains having higher diffusivity, such that the small molecules have more inertia to escape from the electric field lines and trapped in the deep regions.

To our knowledge, Panwar and Kumar [106] have done the most comprehensive work in characterizing time scales involving electrophoresis of polymer chains through constrictions. They modeled the polymer as a freely jointed linear bead-rod (Kramers) chain and used BD simulations in order to identify three time scales, i.e. τ_{app} , τ_{act} and

Chapter 7: DPD Simulation of DNA Separation in Entropic Trap

τ_{cross} . Their results are characterized in different conditions of varying electric field strength, size of narrow channel and problem dimensionality (2D and 3D). They found that the approach time τ_{app} , which is related to the motion of the polymer in the deep region towards the entrance of constriction, and activation time τ_{act} , which defines the time scale for overcoming entropic barrier, are both decreased as the sizes of the molecules become larger. However the traveling time through the shallow region τ_{cross} , increased upon increase of the length of the chains. Furthermore, they identified crossing mechanisms involved in polymer electrophoresis through confined geometries and nanopores.

More recently and in similar manner, Lee and Joo [107] used the worm like chain (WLC) models and performed BD numerical experiments for the electrophoretic motions of both linear and branched polyelectrolyte molecules traversing entropic traps. In addition, they applied the coarse grained bead spring model to investigate the effects of polymer topology and found the radius of gyration to be the dominant factor influencing time scales during escape of polymer through the entropic array.

In most of the above simulations, several important physical phenomena were not considered, these include:

- According to [108], the surface of channel walls may be negatively charged during the experiment generating electroosmotic flow which slows down DNA molecules from their migration towards the anode. Since in most experimental conditions the induced forces from electroosmotic flow on chains segments were found to be weak, this effect was neglected. However electroosmotic flow is strengthened in intense

Chapter 7: DPD Simulation of DNA Separation in Entropic Trap

electric fields and high buffer concentrations which lead to converging or diverging flow patterns as well as circulation.

- Debye screening length of DNA in usual buffer solutions is of the order of a few nanometers. However the persistence length of DNA is about 50nm , thus electrostatic interactions between monomers were omitted.
- DNA and solvent hydrodynamic interactions were neglected. The assumption was made by the argument that the induced friction by motion of counter ions cancels the hydrodynamic flow generated by the migration of chain segments in the cases of free solution electrophoresis. However, according to Viovy [109], hydrodynamic interaction is not negligible for DNA undergoing electrophoresis. Jendrejack et al. [110] also claimed that a hydrodynamic interaction model will generate results which are in qualitative agreement with experimental data. Moreover, the cancellation argument is not valid if the chain blocked by an obstacle [111, 112] and this is the case especially near the entrance of the constriction.
- Both hydrodynamic and electrostatic interactions between chains and the walls are disregarded. This could be unnatural, since the walls are being charged during the process and have some electrostatic effects especially during the migration of polymer through the shallow region and when the chain contacts the walls or are very close to the wall boundaries. In addition, walls always induce hydrodynamic effects thus affecting flow patterns as well as chain trajectories.
- Some authors have not taken into account the excluded volume interactions. However, it is obvious that the chain segments do not overlap each other and cannot occupy the same position.

Chapter 7: DPD Simulation of DNA Separation in Entropic Trap

Bearing in mind the above restrictions, we investigate an alternative approach in order to simulate the migration of DNA through constriction. We find dissipative particle dynamics (DPD), which is a mesoscopic method that can bridge the gap between atomistic simulations and continuum network simulations, as an appropriate tool to explore the process. Using the DPD technique with appropriate parameters, we can naturally capture some of the dynamical and rheological properties, such as the hydrodynamic interactions, the DNA-wall interactions and excluded volume effects. In particular, the DPD is becoming noted as a promising method for the simulation of complex fluids such as suspensions of DNA, polymers and colloids, and thus it is more easier to simulate electroosmotic effects with DPD than other techniques.

7.3 Description of Simulation Model and Parameters

7.3.1 DPD Algorithm and Chain Model

DPD algorithm was explained in detail in detail in Chapter 2 and the time evolution of the system is adopted using the velocity Verlet algorithm equation (4.6) with the same parameters described earlier Table 7-1 lists the parameters used in the present DPD simulations.

Table 7-1 DPD simulation parameters.

$k_B T$	ρ_f	ρ_w	r_c	σ	dt
0.2	4	6	1	3	0.02

We employ the WLC model that was described earlier in Chapter 6 and the chain parameters are shown in Table 7-2, where a_{ff} is the repulsive force coefficient between fluid-fluid particles, a_{pp} that between polymer-polymer, a_{pf} that between polymer-fluid,

Chapter 7: DPD Simulation of DNA Separation in Entropic Trap

a_{wf} that between wall-fluid and a_{pw} that between polymer-wall. The choices of these coefficients are based on the results obtained in the previous chapter, the quality of the solvent and the excluded volume effects. In addition to all the inter-particle forces, the electrical force (see next section) is applied on each bead according to the chain position in the channel.

Table 7-2 Simulation parameter sets for WLC model.

λ_p^{eff}	L_{sp}	$a_{ff} = a_{pp} = a_{pf}$	a_{wf}	a_{pw}
0.106	2 or 4	3.75	5.6	7.5

7.3.2 Microchannel Geometry and Wall Boundary Conditions

The electrophoretic motion of DNA is mimicked by distributing uniform charges q among each of the beads in the chain. In order to find the driving force, the 2D electric potential $\phi(x, y)$ in the channel was determined by solving the Laplace equation $\nabla^2 \phi = 0$. The equation was solved numerically, using a second-order finite difference scheme on a very refined mesh of size $\Delta x = \Delta y = 0.04$. The channel walls are insulated implying zero electric flux or von Neumann boundary conditions at surface boundaries ($\mathbf{n} \cdot \nabla \phi = 0$, where \mathbf{n} is the wall normal vector). We enforced the periodic voltage drop condition at the two sides of the slits $\phi(L, y) - \phi(0, y) = E_{av} L$, where L is the length of each period and E_{av} is the average electric field applied to the microchannel. Subsequently the nonuniform local electric field is obtained from the gradient of the electric potential $\mathbf{E} = -\nabla \phi$ and the electric force exerted on each bead is thus $\mathbf{F}_i^e = q\mathbf{E}$. In solving the Laplace equation for this case it is sufficient to solve the equation for unit voltage drop ($\Delta V = E_{av} L = 1$). To obtain solutions for different potential differences we only need to multiply the unity solution to the required voltage drop. Figure 7.2 and

Chapter 7: DPD Simulation of DNA Separation in Entropic Trap

Figure 7.3 depict the field contour plots of ϕ , E_x and E_y with the channel dimensions shown in Table 7-3. In Figure 7.2 the x -component of the electric field along the channel is plotted and it shows good agreement with the following approximation

$$E_s = \frac{2t_d}{t_d + t_s} E_{av} = \frac{t_d}{t_s} E_d \quad (7.2)$$

where t_d and t_s are the depths of thick and shallow regions and E_d is the electric field strength at the well (see Figure 7.1).

Table 7-3 The dimensions of the microchannel.

L_d	L_s	t_d	t_s
40	40	20	2

In DPD simulations we impose periodic boundary conditions on both the fluid and chain particles in the x (along two sides of the constriction) and z directions. As described in Chapter 6, we use the method of ghost particles to impose periodic boundary condition to the chain beads. The walls are simulated using the earlier proposed random distribution of fixed particles and in order to prevent the chain and fluid particles penetrating to walls, we applied the earlier developed bounce normal reflection as described in Chapter 5.

Chapter 7: DPD Simulation of DNA Separation in Entropic Trap

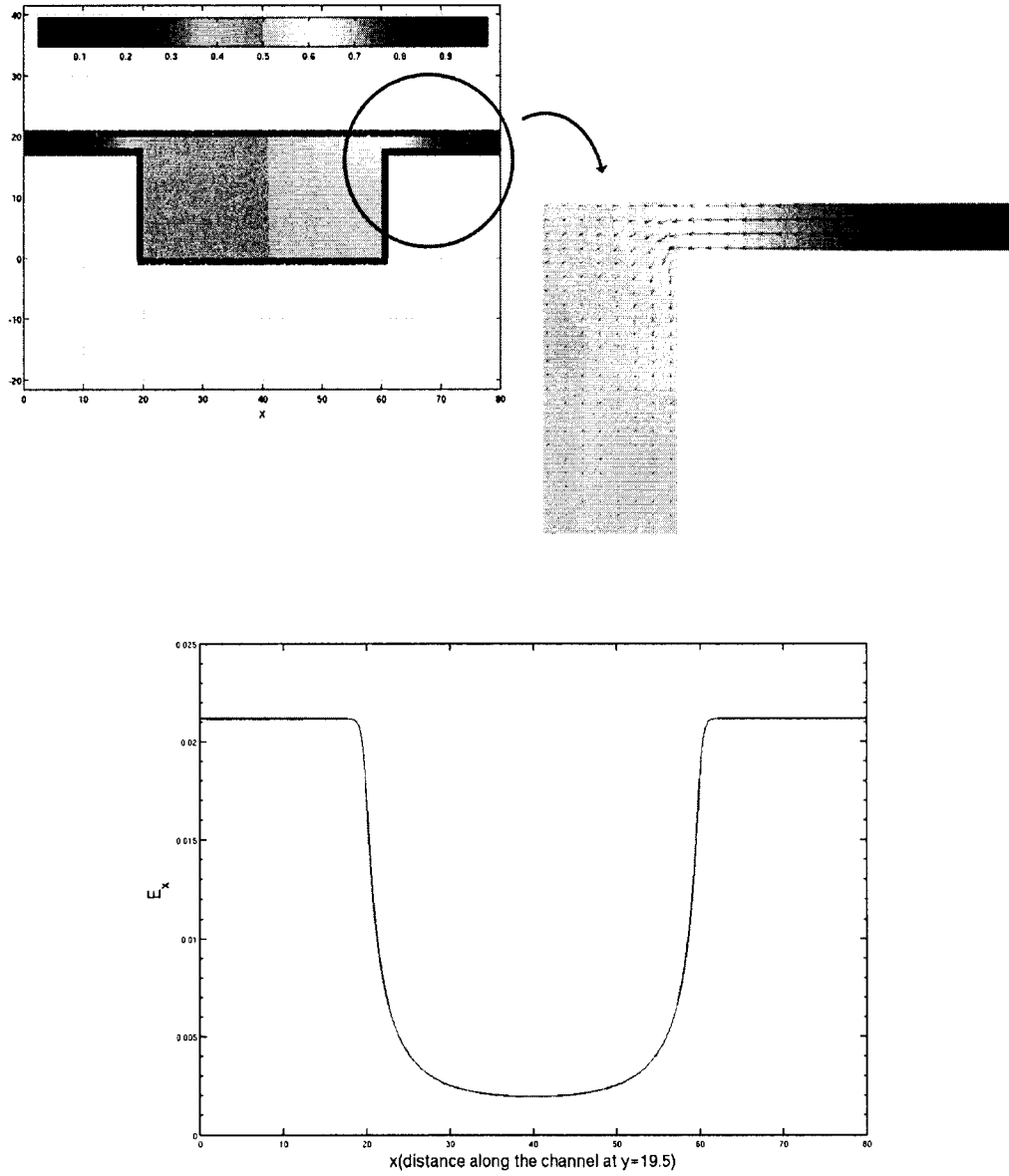


Figure 7.2 Top: The electric potential ϕ contour plot and representation of several electric field vectors near the slit. Bottom: The x-component of the electric field inside the channel E_x , as a function of length of channel, measured along the plane in middle of the shallow region.

Chapter 7: DPD Simulation of DNA Separation in Entropic Trap

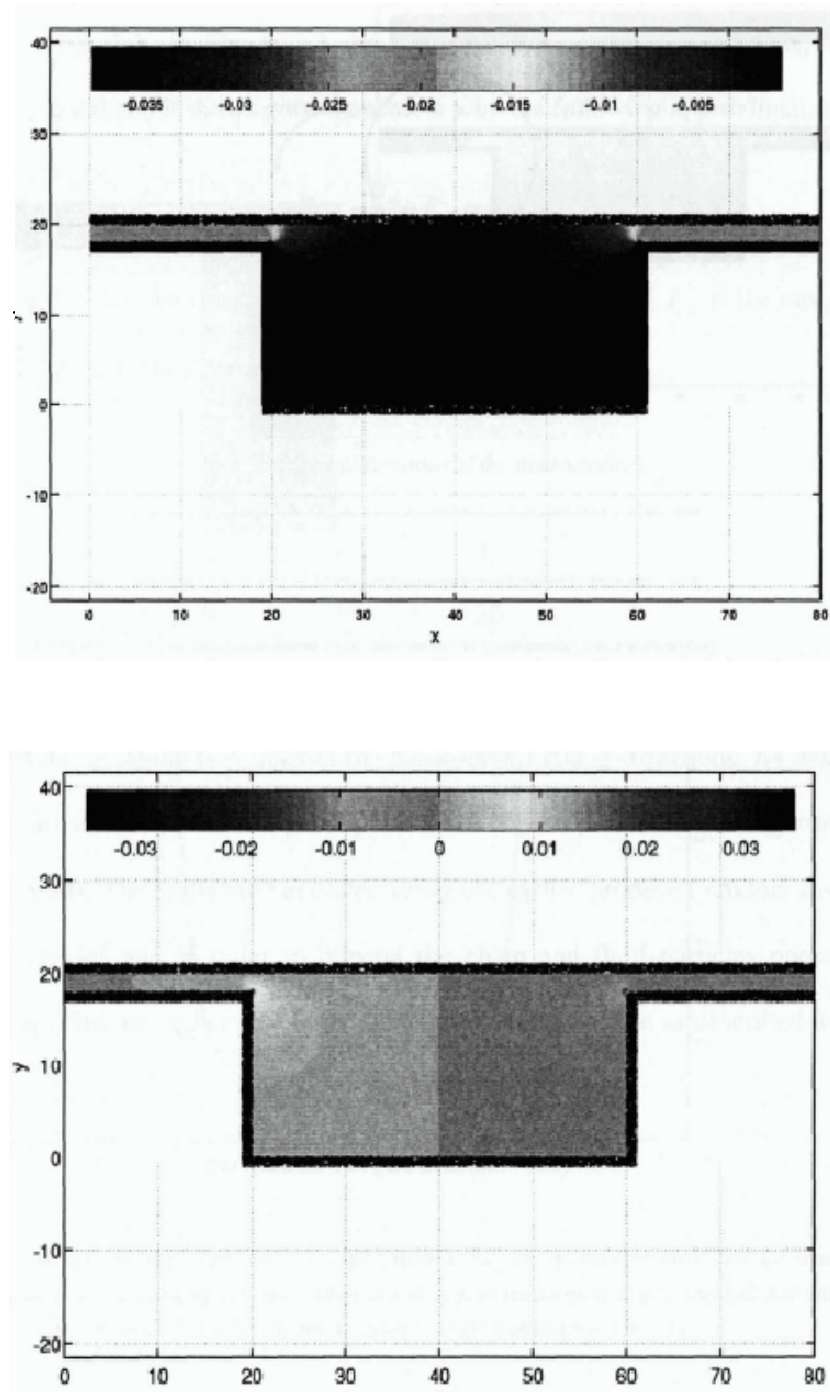


Figure 7.3 Top: The electric field x-component E_x contour plot. Bottom: The electric field y-component E_y contour plot.

7.4 Results and Discussions

In this section the migration of DNA chains in microchannels is examined as we present the results of the present simulations. First the electric field was set to $E_{av} = 0.5$ and we found the x-component of the center of mass trajectories for DNA chains of length $N = 5, 10, 20, 40, 80$, as shown in Figure 7.4. This allows us to define the dimensionless mobility μ . We estimated μ as the slope of the line fitted through the x-component trajectory of the chain which has passed at least 20 periods. From Figure 7.4, we observed that when the chain length increased, we found that in addition to higher slope of the trajectories, they also became smoother. More specifically, for the longest chain of length $N = 80$, the steps in the trajectory appear smaller and gentler than the shortest chain of length $N = 5$.

In order to study the effects of the electric field strength and the chain length on mobility, we conducted several simulation runs. We performed runs for different chain lengths of $N = 10, 20, 40, 80, 160, 320$ in average field values of $E_{av} = 0.0625, 0.125, 0.25, 0.5$. The estimated mobility μ as a function of N or E_{av} are plotted in Figure 7.5. For all field values we find that the longer chains travel faster. In this figure we observe that the mobility of the chain increased significantly when the chain length increased from $N = 40$ to $N = 80$ or 160 , and this is in a good qualitative agreement to the experimental observations of Han et al. [1-3]. Furthermore, as the electric field is intensified, the mobility variation also becomes larger.

In this work, our main interest is the overall motion of the chains and our results generally show that the longer the chains, the greater the mobility. Three regions are

Chapter 7: DPD Simulation of DNA Separation in Entropic Trap

identified where chains with different sizes translate with different conformation and speed. Following we describe the mechanisms of chain migration in each region qualitatively.

First is the migration of the chain through the deep region. In this region the electric field lines are nonuniform and due to higher Brownian mobility smaller chains are more probable to diffuse out of the field lines. This causes small molecules to reach the deeper areas or the corner of the well and be trapped there for longer times. The x-y trajectories of chains with $N=5, 20, 80$ are illustrated in Figure 7.6. The effect of random Brownian diffusion from the field lines is more visible in high electric fields and for smaller molecules. Here the random motion depends on two dominant parameters, namely the length of the chain and the conformation of the molecule. When the chain is longer, it has more segments which come under influence of the electric field lines and so there is very low probability of a sudden crossing of the molecule occurring. In addition the relaxation time of a small chain is very low and as a result when the molecule gets pushed out of the slit, it would quickly recoil. The coiled chains have little surface contact with the solvent molecules and electric field lines so they would have higher random motion while long chains remain stretched and move in a smoother manner (see Figure 7.6 and Figure 7.4).

The opening of the slit is the second region where several migration mechanisms were discussed in earlier sections. From our results, we found two main conformations by which the chains approach and pass through the opening of the gap; the hairpin and two ends escapes. The formation of each state near the slit depends mainly on the size of the chain and the conformation of the chain as it approaches the gap from the well. Sebastian and Paul [113] argued that the free energy barrier for the hairpin escape is twice that of

Chapter 7: DPD Simulation of DNA Separation in Entropic Trap

the two ends escape because each hairpin can be considered as two chains crossing from the ends. Similar to Han et al. [1-3], they found that in the case of hernia formation and chain migration in the hairpin shape, the speed of escape is decreased as the chain length increased. However when the chain approaches slit through its end they claimed that the speed of process is not dependent on molecule size since all linear chains have two ends. In our present simulations, we observed both mechanisms. However when the chain becomes longer, we found that hairpin formation is the dominant mode of escape (see Figure 7.7 to Figure 7.10 for two ends and hairpin migration of DNA chains). We note that for very small chains ($R_g \ll t_s$), none of the above mechanisms were present and the chain passes through the slit rapidly and without significant deformation.

Finally the speed of migration of molecules crossing through the shallow region is size dependant and we expect it to increase with N as discussed in [113]. We observed that due to high electric field strength, the DNAs generally travel very fast in this region. Also, we note that when the DNA enters the slit from one of its ends, it would have the chance to stretch out and uncoil completely. In Figure 7.7 and Figure 7.8, the conformation evolution snapshots of a DNA chain with $N = 80$ approaching and passing the gap are shown. In these figures, the DNA is approaching with one end having a small hairpin formed. The DNA is completely uncoiled as it travels through the slit but recoils soon after exiting from the gap. In Figure 7.9 and Figure 7.10, the DNA approaches the slit while forming two hairpins in the middle of the chain. As the chain length increases, the probability of the number of hairpins which would be formed also increases, and this assists in faster travel of the DNA from the entrance of the slit. The extension of the chain in z direction in order to form higher contact surface with the gap is the other physical trend which was generally observed for longer chains.

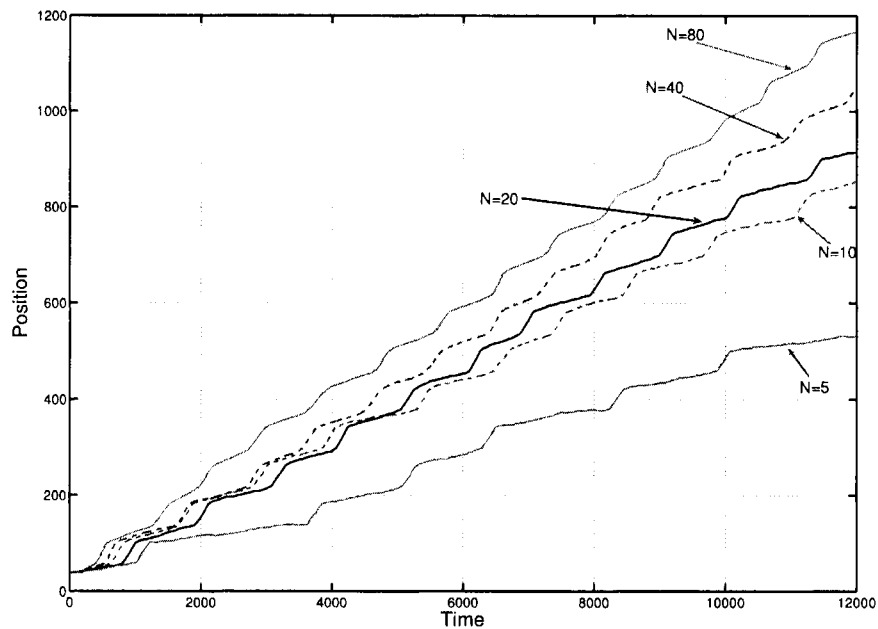


Figure 7.4 The x -component of the center of mass trajectories of DNA chains of $N = 5, 10, 20, 40, 80$ beads for the case of $E_{av} = 0.5$ and $L_{sp} = 4$.

7.5 Concluding Remarks

We have presented DPD simulations studies of migration of DNA chains through entropic traps and our results generally show a good qualitative agreement with existing experimental data. The mesoscopic features of the DPD technique enabled us to capture the hydrodynamic interactions automatically. Three distinct regions where the chains migrate with different mechanisms were distinguished. Each region has different effects on the speed of the total process. Moreover, we observed several conformational phenomena which depend on chain length, the geometry of the microchannel and the strength of the electric field. The chains formed hernias and were sucked into the gap while approaching the shallow region. The geometrical and field (electrical) conditions in the gap force the DNA chains to uncoil and travel smoothly through the slit. The chain

Chapter 7: DPD Simulation of DNA Separation in Entropic Trap

then escapes from the gap and recoils in the deep region. According to the speed and form of relaxation and evolution of the chain in the well, it becomes ready to approach the next constriction.

Two mechanisms are identified that cause the size-dependent trapping of DNA chains and thus mobility differences. Firstly, small molecules are found to be trapped in the deep region due to higher Brownian mobility and crossing of electric field lines. Secondly, longer chains have higher probability to form hernias at the entrance of the gap and can pass the entropic barrier more easily. Consequently longer DNA molecules have higher mobility and travel faster than shorter chains.

Chapter 7: DPD Simulation of DNA Separation in Entropic Trap

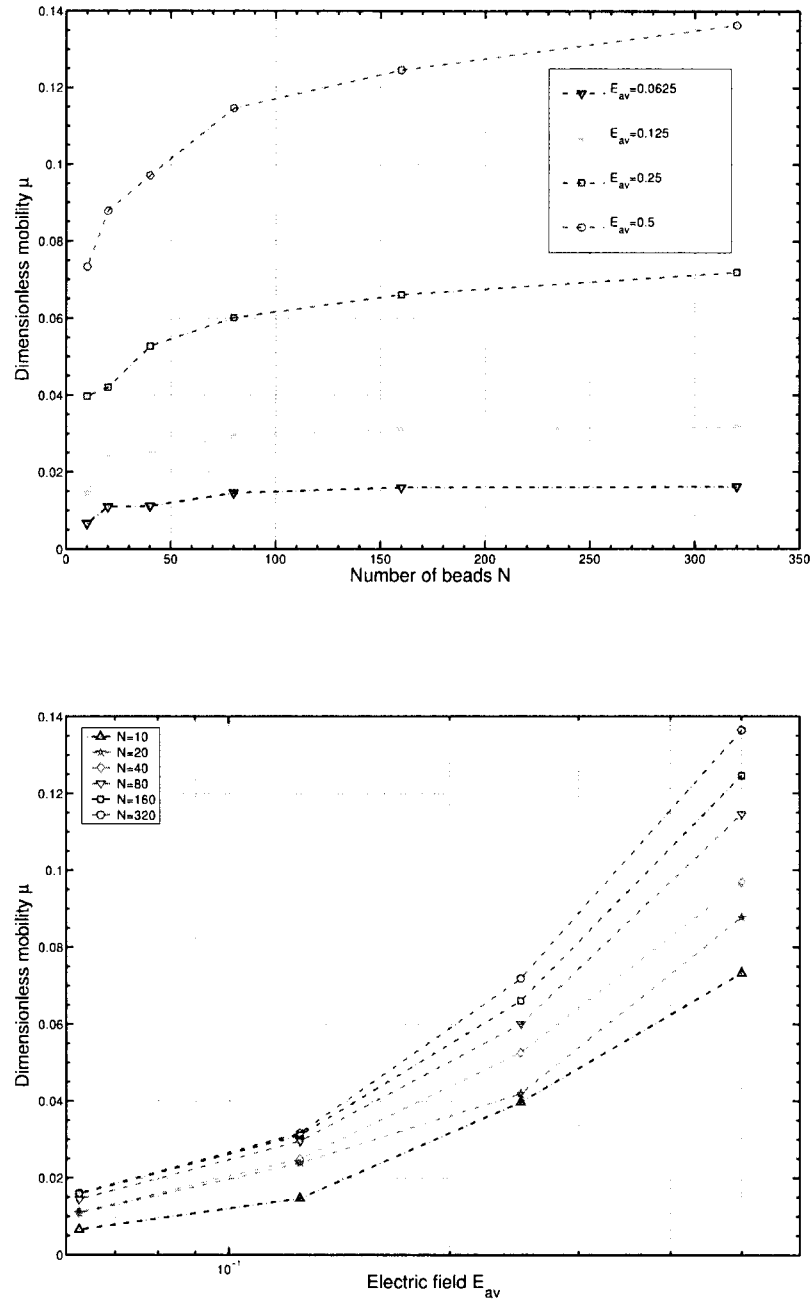


Figure 7.5 Top: Dimensionless mobility μ of DNA chains for $E_{av} = 0.0625, 0.125, 0.25, 0.5$ as a function of N . Bottom: Dimensionless mobility μ of DNA chains for $N = 5, 10, 20, 40, 80, 160$ as a function of E_{av} .

Chapter 7: DPD Simulation of DNA Separation in Entropic Trap

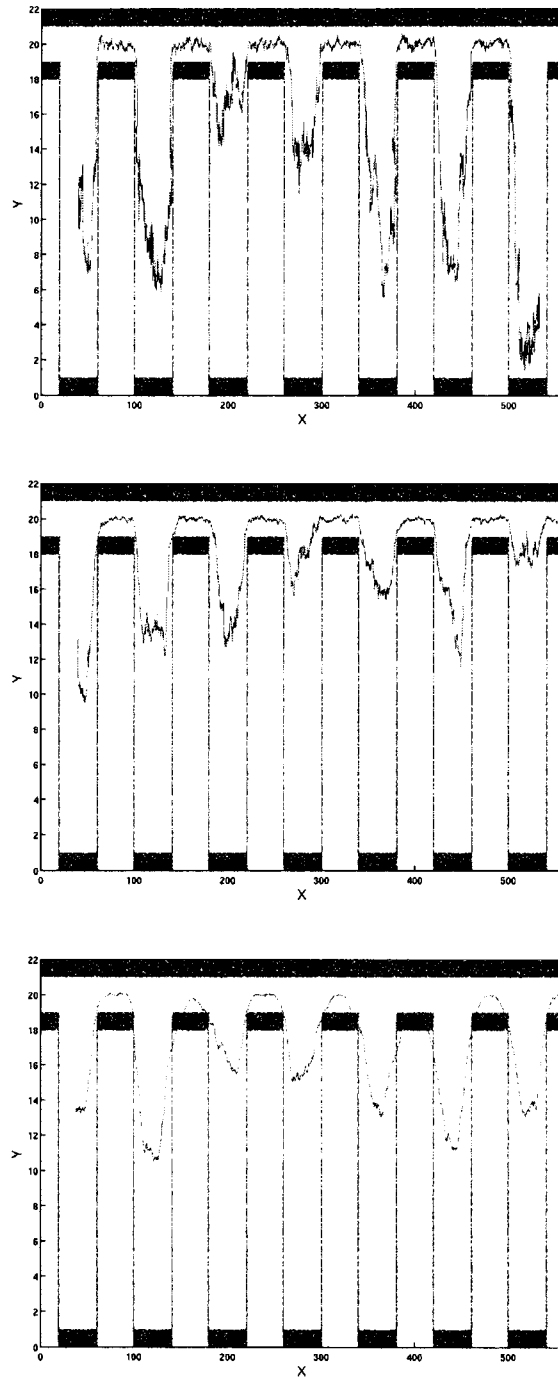
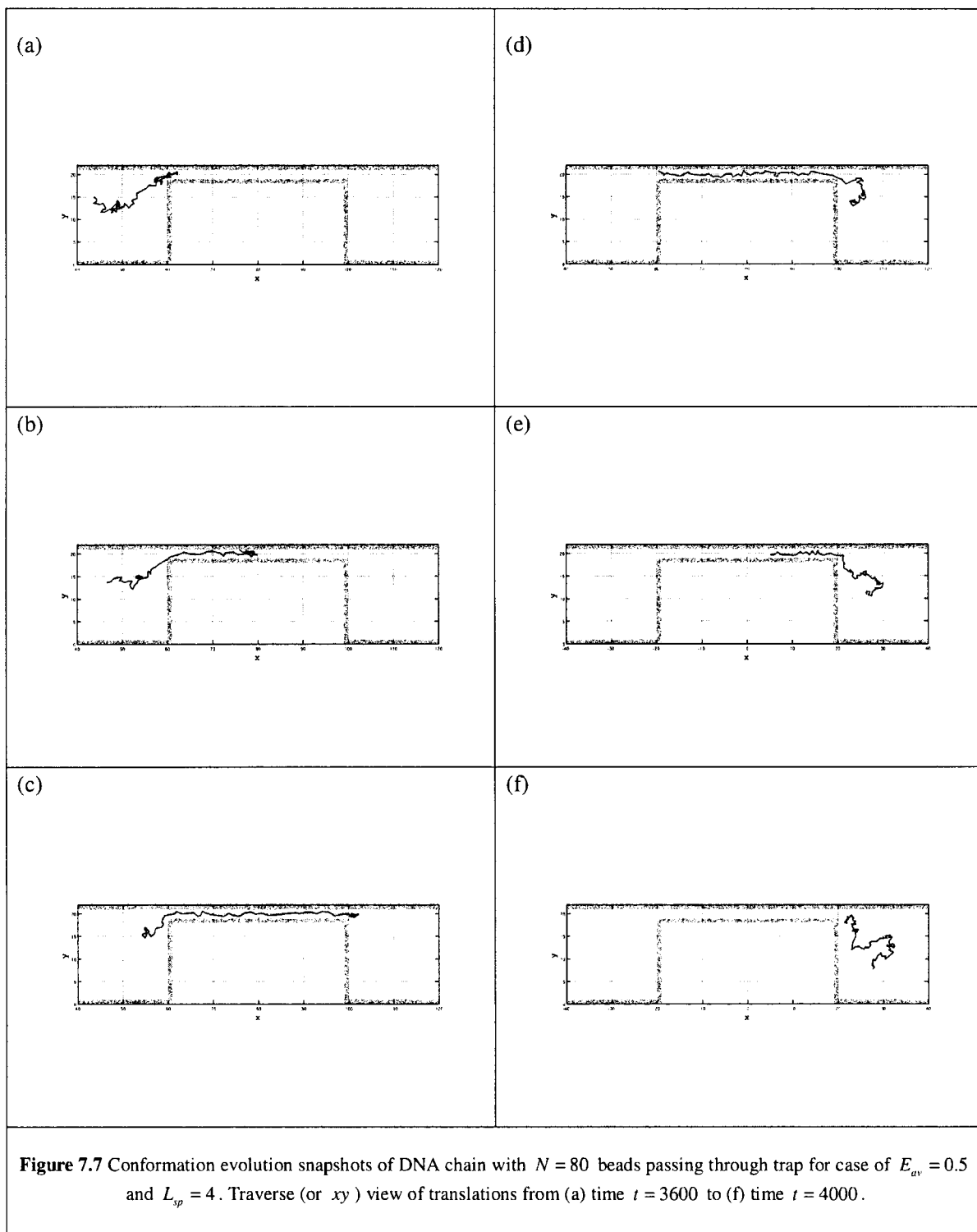
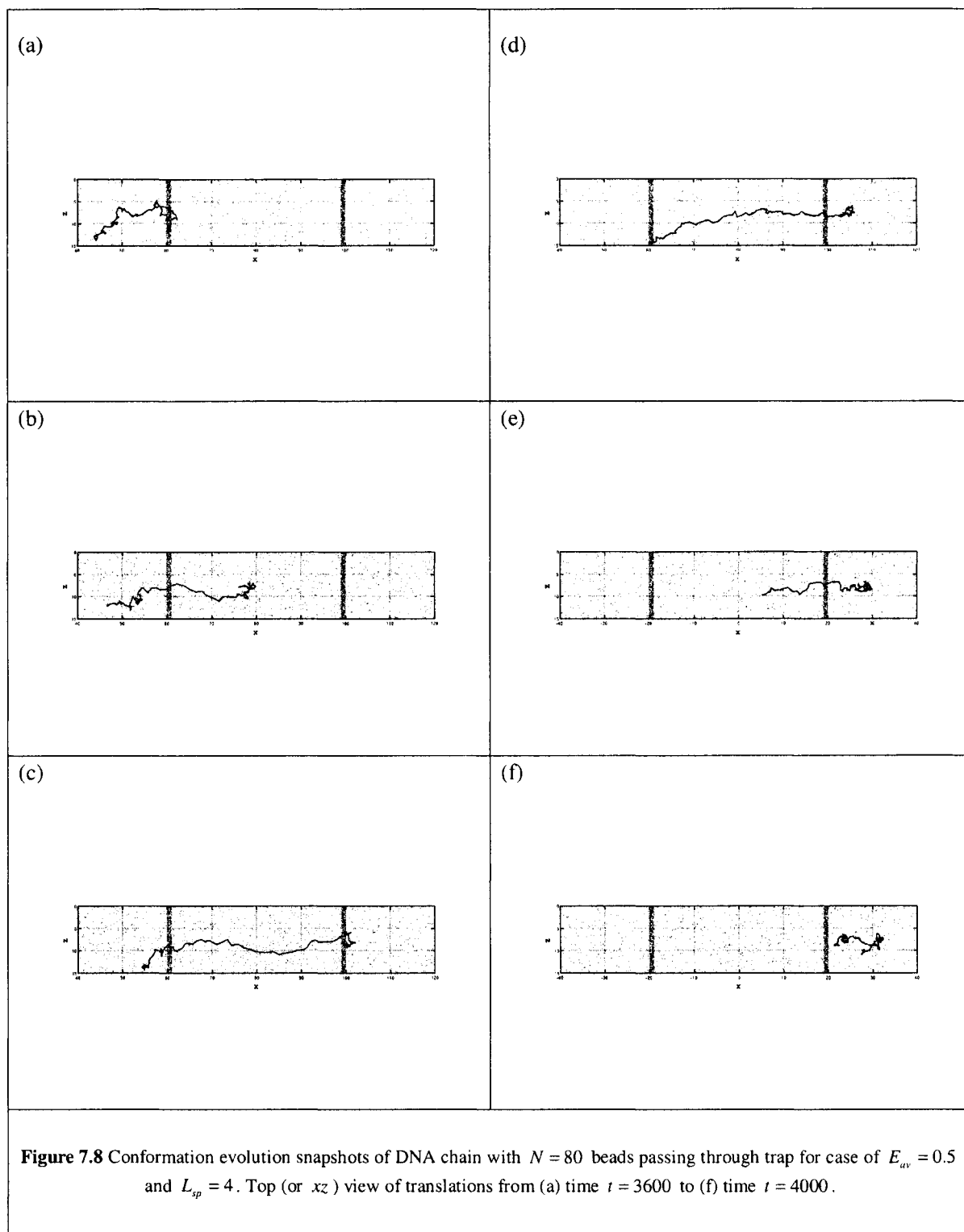


Figure 7.6 Traverse (or xy) view of the center of mass trajectories (blue lines) of migrating DNA chains of different sizes through array for the case of $E_{uv} = 0.5$ and $L_{sp} = 4$. Top: $N = 5$. Middle: $N = 20$. Bottom: $N = 80$.

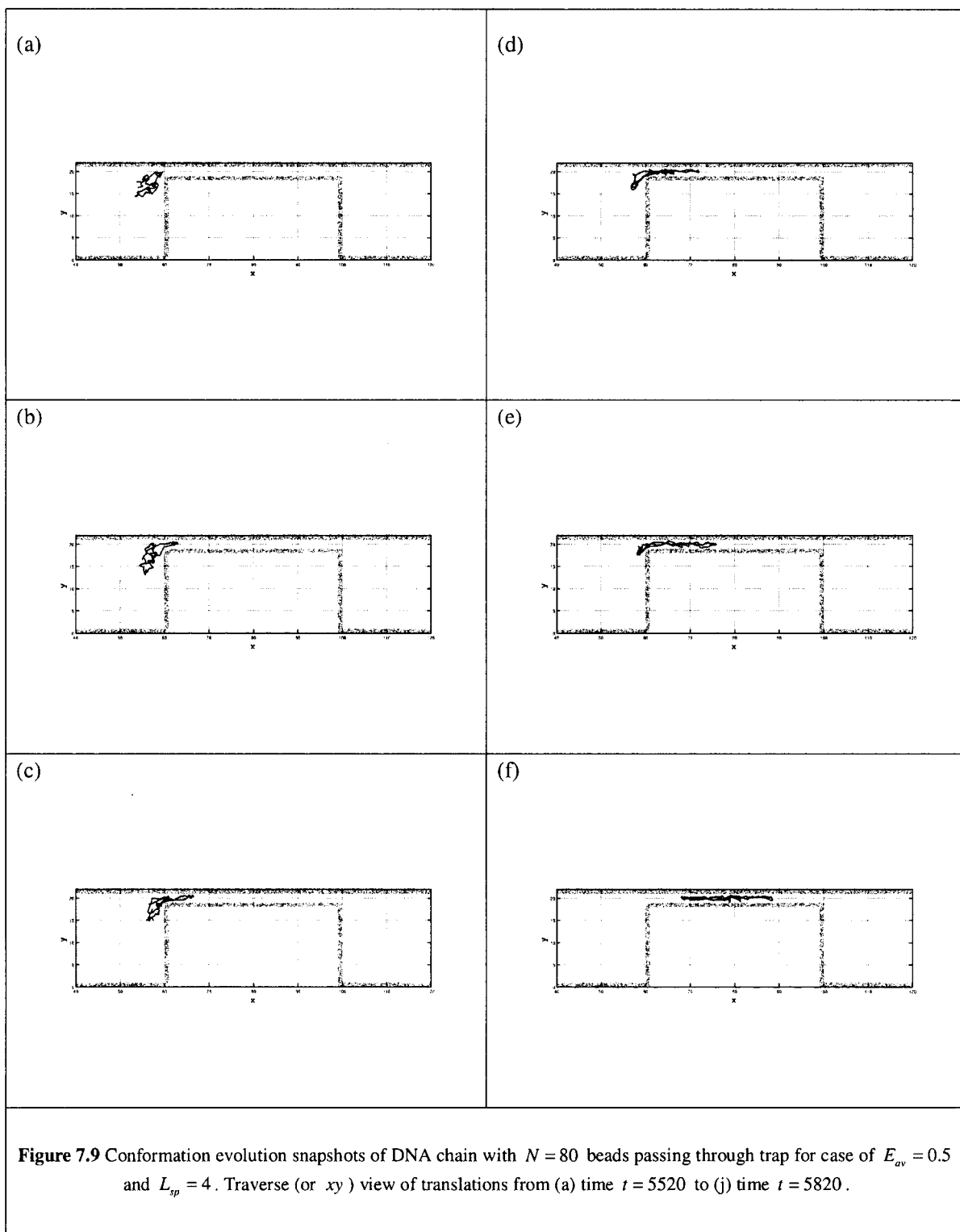
Chapter 7: DPD Simulation of DNA Separation in Entropic Trap



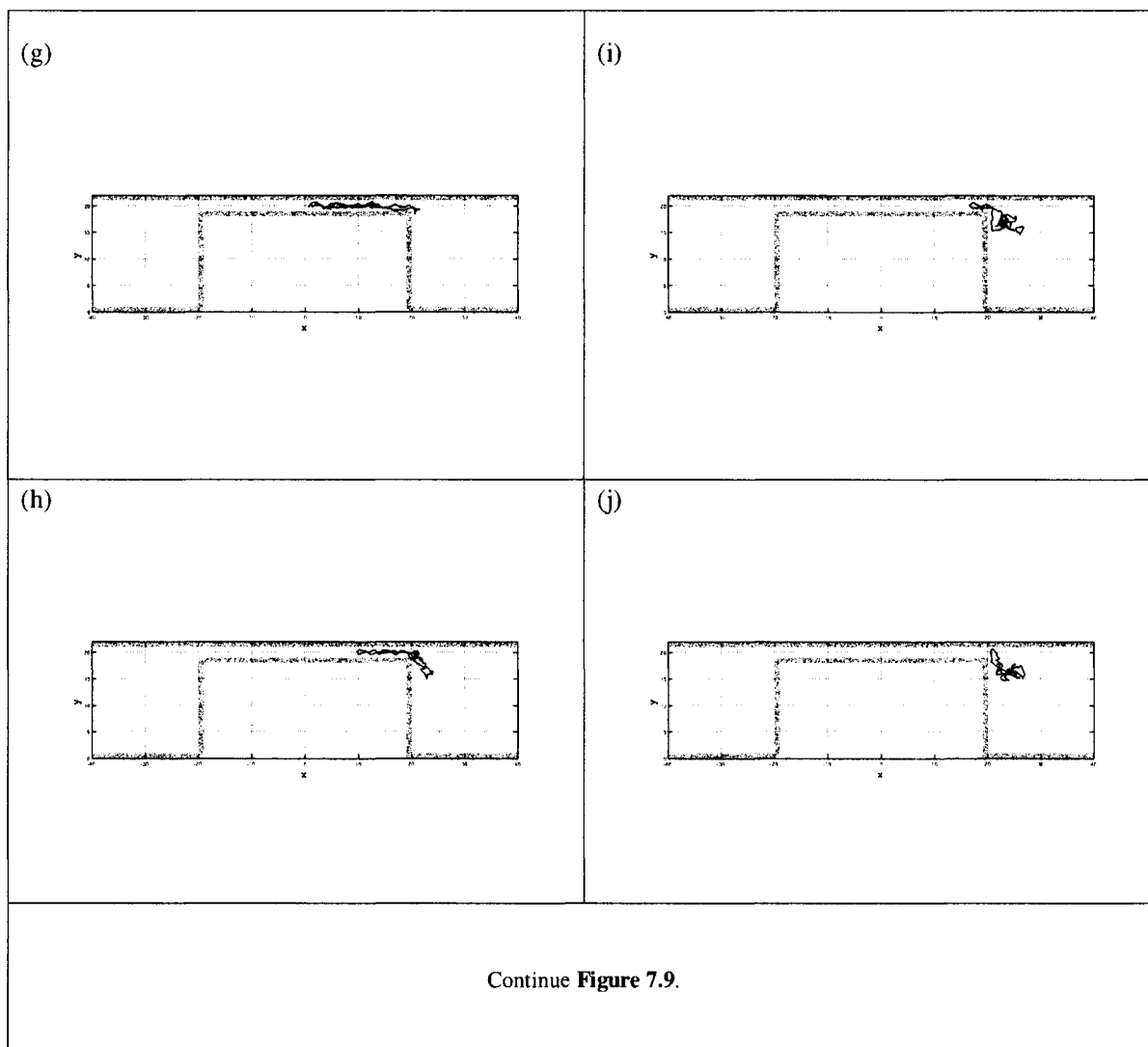
Chapter 7: DPD Simulation of DNA Separation in Entropic Trap



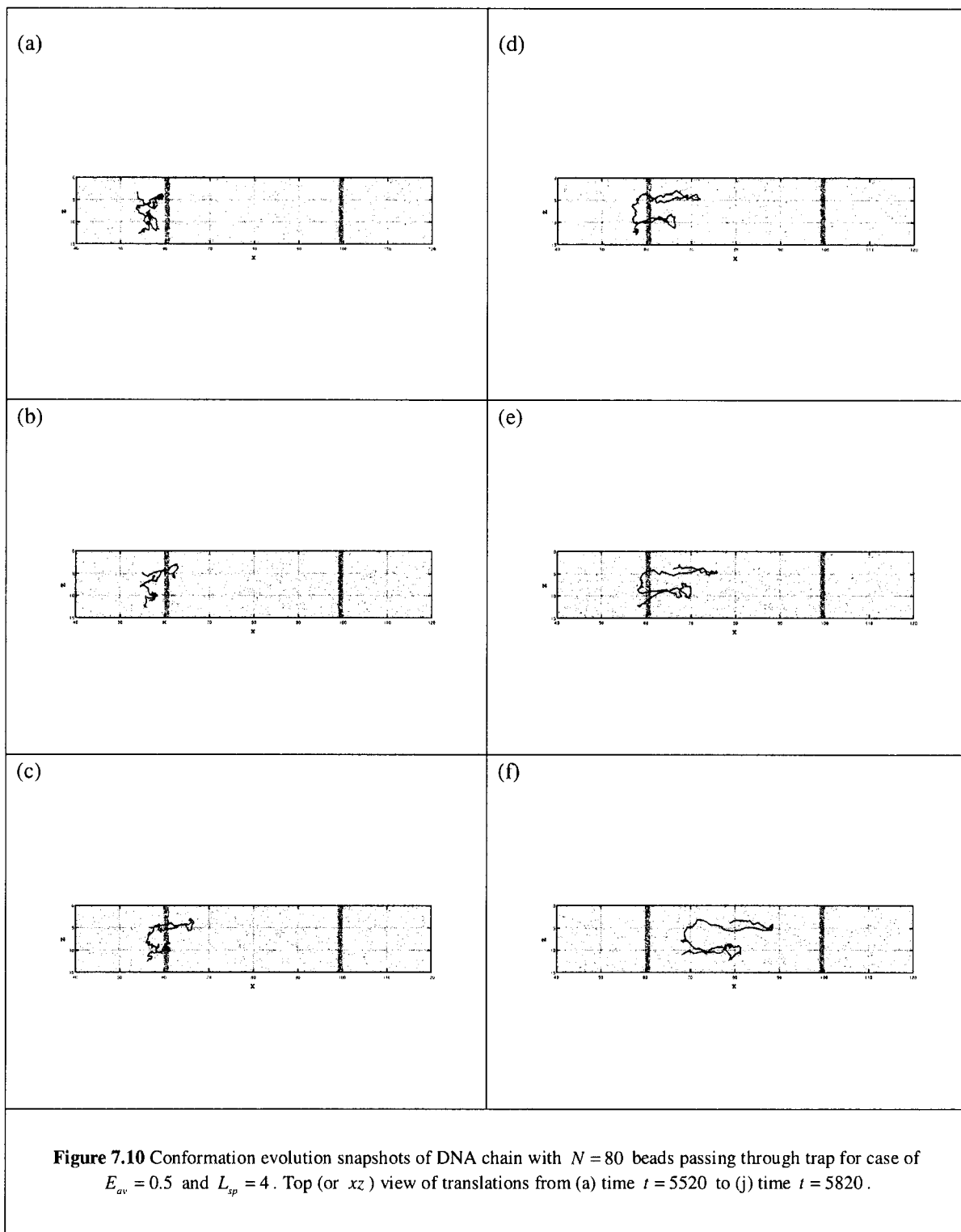
Chapter 7: DPD Simulation of DNA Separation in Entropic Trap



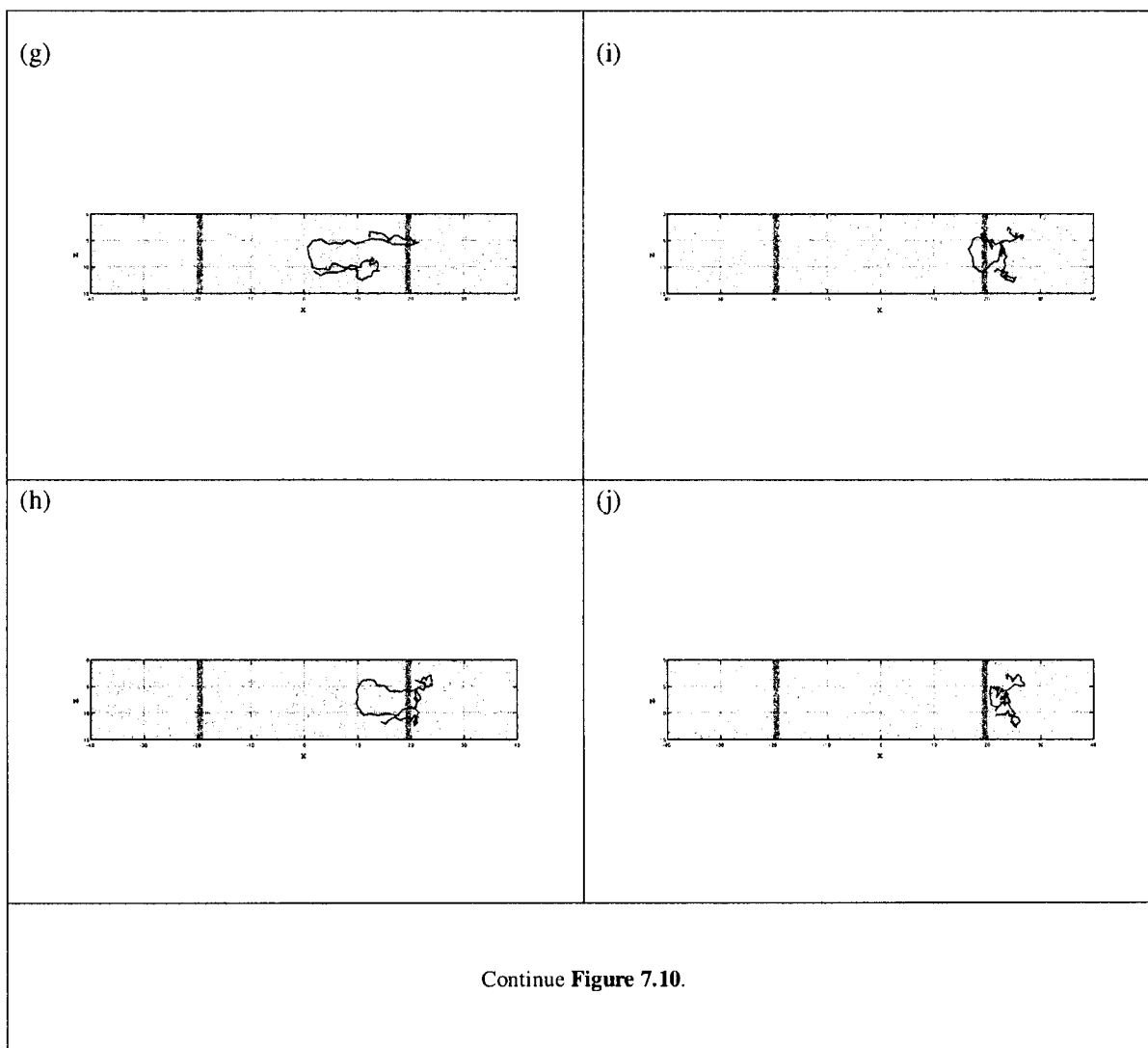
Chapter 7: DPD Simulation of DNA Separation in Entropic Trap



Chapter 7: DPD Simulation of DNA Separation in Entropic Trap



Chapter 7: DPD Simulation of DNA Separation in Entropic Trap



Chapter 8

Concluding Remarks and Future Perspective

8.1 Concluding Remarks and Major Contribution

This thesis can be divided into two parts. The first part started with the introduction of the DPD method followed by in depth review and derivation of the theoretical features of DPD. Next we have a very comprehensive review of boundary models for the DPD. Following the definition of required DPD simulation models and parameters, we propose in Chapter 5 a new boundary condition for the significant reduction of density fluctuations. In the second part of this work which begins in Chapter 6, we formulate a coarse grained DPD WLC model to simulate and determine the static properties of polymer chains in dilute solutions. Eventually we study the motion of DNA molecules traveling through entropic channels.

The major contributions of this work can be summarized as follow:

1. We derived the DPD algorithm and identified the appropriate DPD simulation parameters. Subsequently we comprehensively studied different boundary models applicable in DPD simulations and identified their characteristics.
2. We proposed the new bounce normal reflection in combination with random wall distribution in order to capture the density fluctuations near the wall boundaries. To

validate our new boundary condition, we applied it to three flow regimes and we obtained very good results which were consistent with macroscopic features.

3. We indentified the DPD bead spring models for polymer chains. Following this, we optimized the WLC bead spring DPD model to obtain the correct exponent value of polymer scaling laws.

4. We applied the DPD in simulation of WLC bead-spring models to explore the electrophoresis migration of DNA molecules traveling through narrow constrictions and our results generally show excellent qualitative agreement with existing experimental data.

8.2 Possible Future Work

The DPD method, a relatively new mesoscopic simulation technique for the simulation of complex systems, addresses certain features such as geometry complexity that other methods like BD fail to point out. However there are several open issues associated with the DPD that may require new development work or future refinements. These include possible new directions in theoretical aspects as well as applications.

8.2.1 Theoretical Aspects

- **Heat Transfer:** To formulate appropriate DPD theories and algorithms that can handle heat transfer problems would be one of the most desired theoretical features for DPD in the future.
- **Time Integration Techniques:** Fast time evolution algorithms to speed up the simulations are still in high demand.

Chapter 8: Summary and Future Perspective

- **Computer Algorithms:** Depending on the application, huge computational cost may be required. There are vast opportunities for particle methods to decrease this cost by improving cell algorithms (such as the Neighbor List method) as well as efficient parallel implementation.
- **Inter Particle Forces:** The particle based nature of DPD offers promising potential in modeling not only different types of interaction within the same type of particles in single phase but also for various other multi phase interactions. This requires enhancements in defining particle forces, such as conservative forces for example.
- **Boundary Conditions:** Although we introduced the bounce normal boundary reflection at the walls, further refinements for implementation of boundary conditions for other geometries and problems may still be necessary.
- **Multiscale Modeling:** It would a major achievement if we can concurrently couple DPD with other particle based methods like MD in order to handle multiscale problems. In the nano scale regions or close to boundaries where DPD can not capture the details of microscale or even nanoscale interactions, more refined techniques can be used while DPD is being used to simulate the bulk region.

8.2.2 Applications

- Variety of single phase, two phase or multiphase problems.
- Complex flow in nano/micro systems and porous media.

Chapter 8: Summary and Future Perspective

- Simulation of biological macromolecules subject to different flows and geometries.
- Rheology and suspension of polymers in various applications.

Publications Arising from Thesis

Emadaldin Moeendarbary, T.Y. Ng and K.Y. Lam, A New “Bounce-Normal” Boundary in DPD Calculations for the Reduction of Density Fluctuations. Proceedings of the ASME Micro/Nanoscale Heat Transfer International Conference, Tainan, Taiwan, January 6-9, 2008

E. Moeendarbary, T.Y. Ng and K.Y. Lam, Boundary Condition Diagnostics In Dissipative Particle Dynamics And A New "Bounce-Normal" Boundary For The Accurate Simulation Of Density Fluctuations (Submitted to Computational Science & Discovery).

E. Moeendarbary, T.Y. Ng and K.Y. Lam, Migration of DNA Molecules Through Entropic Trap Arrays: A Dissipative Particle Dynamics Study (To be submitted).

References:

1. Han, J. and H.G. Craighead, *Separation of long DNA molecules in a microfabricated entropic trap array*. Science, 2000. **288**(5468): p. 1026-1029.
2. Han, J. and H.G. Craighead, *Characterization and optimization of an entropic trap for DNA separation*. Analytical Chemistry, 2002. **74**(2): p. 394-401.
3. Han, J., S.W. Turner, and H.G. Craighead, *Entropic Trapping and Escape of Long DNA Molecules at Submicron Size Constriction*. Physical Review Letters, 1999. **83**(8): p. 1688-1691.
4. Karniadakis, G., A. Beskök, and N.R. Aluru, *Microflows and nanoflows: fundamentals and simulation*. 2005, Springer Online Book: Springer.
5. Groot, R.D. and K.L. Rabone, *Mesoscopic simulation of cell membrane damage, morphology change and rupture by nonionic surfactants*. Biophysical Journal, 2001. **81**(2): p. 725-736.
6. Groot, R.D. and P.B. Warren, *Dissipative particle dynamics: Bridging the gap between atomistic and mesoscopic simulation*. Journal of Chemical Physics, 1997. **107**(11): p. 4423-4435.
7. Boek, E.S., et al., *Simulating the rheology of dense colloidal suspensions using dissipative particle dynamics*. Physical Review E - Statistical Physics, Plasmas, Fluids, and Related Interdisciplinary Topics, 1997. **55**(3 SUPPL. B): p. 3124-3133.
8. Koelman, J.M.V.A. and P.J. Hoogerbrugge, *Dynamic simulations of hard-sphere suspensions under steady shear*. Europhysics Letters, 1993. **21**(3): p. 363-8.
9. Schlijper, A.G., P.J. Hoogerbrugge, and C.W. Manke, *Computer simulation of dilute polymer solutions with the dissipative particle dynamics method*. Journal of Rheology, 1995. **39**(3): p. 567-79.
10. Groot, R.D. and T.J. Madden, *Dynamic simulation of diblock copolymer microphase separation*. Journal of Chemical Physics, 1998. **108**(20): p. 8713-24.
11. Groot, R.D., T.J. Madden, and D.J. Tildesley, *On the role of hydrodynamic interactions in block copolymer microphase separation*. Journal of Chemical Physics, 1999. **110**(19): p. 9739.
12. Jury, S., et al., *Simulation of amphiphilic mesophases using dissipative particle dynamics*. Phys. Chem. Chem. Phys, 1999. **1**: p. 2051.
13. Groot, R.D., *Mesoscopic simulation of polymer-surfactant aggregation*. Langmuir, 2000. **16**(19): p. 7493-7502.
14. Venturoli, M. and B. Smit, *Simulating the self-assembly of model membranes*. PhysChemComm, 1999. **2**: p. 45-49.
15. Fan, X., et al., *Simulating flow of DNA suspension using dissipative particle dynamics*. Physics of Fluids, 2006. **18**(6): p. 063102-10.
16. Marsh, C.A., G. Backx, and M.H. Ernst, *Static and dynamic properties of dissipative particle dynamics*. Physical Review E - Statistical Physics, Plasmas, Fluids, and Related Interdisciplinary Topics, 1997. **56**(2): p. 1676-1691.
17. Marsh, C., *Theoretical Aspects of Dissipative Particle Dynamics*. PhD thesis, 1998, University of Oxford.

18. Hoogerbrugge, P.J. and J. Koelman, *Simulating Microscopic Hydrodynamic Phenomena with Dissipative Particle Dynamics*. Europhysics Letters, 1992. **19**(3): p. 155-160.
19. Espanol, P. and P. Warren, *Statistical-Mechanics of Dissipative Particle Dynamics*. Europhysics Letters, 1995. **30**(4): p. 191-196.
20. Kubo, R., *The fluctuation-dissipation theorem*. Reports on Progress in Physics, 1966. **29**: p. 255-284.
21. Risken, H., *The Fokker-Planck equation*, vol. 18 of. Springer Series in Synergetics.
22. McQuarrie, D., A., 1976, *Statistical Mechanics*, New York: Harper & Row.
23. van Kampen, N.G., *Stochastic processes in physics and chemistry*. 1992: North-Holland Amsterdam.
24. Marsh, C.A., G. Backx, and M.H. Ernst, *Fokker-Planck-Boltzmann equation for dissipative particle dynamics*. Europhysics Letters, 1997. **38**(6): p. 411-416.
25. Español, J. and F.J. de La Rubia, *Mixing and equilibrium probability densities in classical statistical mechanics*. Physica A, 1992. **187**(3-4): p. 589-602.
26. Reichl, L.E., *A Modern Course in Statistical Mechanics*. University of Texas Press, Austin, TX, 1980.
27. Résibois, P.M. and M.d. Leener, *Classical kinetic theory of fluids*. 1977: John Wiley.
28. Chan, D.Y.C. and R.G. Horn, *The drainage of thin liquid films between solid surfaces*. The Journal of Chemical Physics, 1985. **83**: p. 5311.
29. Watts, E.T., J. Krim, and A. Widom, *Experimental observation of interfacial slippage at the boundary of molecularly thin films with gold substrates*. Physical Review B, 1990. **41**(6): p. 3466-3472.
30. Koplik, J., J.R. Banavar, and J.F. Willemsen, *Molecular dynamics of fluid flow at solid surfaces*. Physics of Fluids A: Fluid Dynamics, 1989. **1**: p. 781.
31. Thompson, P.A. and M.O. Robbins, *Shear flow near solids: Epitaxial order and flow boundary conditions*. Physical Review A, 1990. **41**(12): p. 6830-6837.
32. Visser, D.C., H.C.J. Hoefsloot, and P.D. Iedema, *Comprehensive boundary method for solid walls in dissipative particle dynamics*. Journal of Computational Physics, 2005. **205**(2): p. 626-639.
33. Revenga, M., I. Zuniga, and P. Espanol, *Boundary conditions in dissipative particle dynamics*. Computer Physics Communications, 1999. **121**: p. 309-311.
34. Hansen, J.P. and I.R. McDonald, *Theory of Simple Liquids*. 2006: Academic Press.
35. Allen, M.P. and D.J. Tildesley, *Computer Simulation of Liquids*. 1987, USA: Oxford University Press.
36. Wang, S.S. and J.A. Krumhansl, *Superposition approximation. II. High density fluid argon*. Journal of Chemical Physics, 1972. **56**: p. 4287-4290.
37. Adams, D.J., E.M. Adams, and G.J. Hills, *The computer simulation of polar liquids*. Molecular Physics, 1979. **38**(2): p. 387-400.
38. Haile, J.M., *Molecular Dynamics Simulation. Elementary Methods*. By. J. Am. Chem. Soc, 1976: p. 98.
39. Wood, W.W. and F.R. Parker, *Monte Carlo Equation of State of Molecules Interacting with the Lennard-Jones Potential. I. A Supercritical Isotherm at about Twice the Critical Temperature*. The Journal of Chemical Physics, 1957. **27**(3): p. 720-733.

40. Lees, A.W. and S.F. Edwards, *The computer study of transport processes under extreme conditions*. Journal of Physics C (Solid State Physics), 1972. **5**(15): p. 1921-8.
41. Boek, E.S., P.V. Coveney, and H.N.W. Lekkerkerker, *Computer simulation of rheological phenomena in dense colloidal suspensions with dissipative particle dynamics*. J. Phys.: Condens. Matter, 1996. **8**: p. 9509.
42. Backer, J.A., et al., *Poiseuille flow to measure the viscosity of particle model fluids*. The Journal of Chemical Physics, 2005. **122**: p. 154503.
43. Fan, X., et al., *Microchannel flow of a macromolecular suspension*. Physics of Fluids, 2003. **15**(1): p. 11-21.
44. Duong-Hong, D., N. Phan-Thien, and X. Fan, *An implementation of no-slip boundary conditions in DPD*. Computational Mechanics, 2004. **35**(1): p. 24-29.
45. Pivkin, I.V. and G.E. Karniadakis, *A new method to impose no-slip boundary conditions in dissipative particle dynamics*. Journal of Computational Physics, 2005. **207**(1): p. 114-128.
46. Xu, J.B., et al., *Dissipative particle dynamics simulation on the meso-scale structure of diblock copolymer under cylindrical confinement*. Molecular Simulation, 2006. **32**(5): p. 357-362.
47. Chen, S., et al., *Flow around spheres by dissipative particle dynamics*. Physics of Fluids, 2006. **18**(10): p. 103605-14.
48. Liu, M., P. Meakin, and H. Huang, *Dissipative particle dynamics with attractive and repulsive particle-particle interactions*. Physics of Fluids, 2006. **18**(1): p. 017101-13.
49. Liu, M., P. Meakin, and H. Huang, *Dissipative particle dynamics simulation of fluid motion through an unsaturated fracture and fracture junction*. Journal of Computational Physics, 2007. **222**(1): p. 110-130.
50. Liu, M., P. Meakin, and H. Huang, *Dissipative particle dynamics simulation of multiphase fluid flow in microchannels and microchannel networks*. Physics of Fluids, 2007. **19**(3): p. 033302-11.
51. Revenga, M., et al., *Boundary models in DPD*. International Journal of Modern Physics C, 1998. **9**(8): p. 1319-1328.
52. Colmenares, P.J. and R. Rousse, *Effective boundary forces for several geometries in dissipative particle dynamics*. Physica A: Statistical Mechanics and its Applications, 2006. **367**: p. 93-105.
53. Kong, Y., et al., *Simulation of a confined polymer in solution using the dissipative particle dynamics method*. International Journal of Thermophysics, 1994. **15**(6): p. 1093-1101.
54. Jones, J.L., et al., *Dynamics of a drop at a liquid/solid interface in simple shear fields: A mesoscopic simulation study*. Faraday Discuss, 1999. **112**: p. 129-142.
55. Willemsen, S.M., H.C.J. Hoefslot, and P.D. Iedema, *No-slip boundary condition in dissipative particle dynamics*. Int. J. Mod. Phys. C, 2000. **11**(5): p. 881-890.
56. Darias, J.R., et al., *Simulation of suspensions in constricted geometries by dissipative particle dynamics*. Molecular Simulation, 2003. **29**(6-7): p. 443-449.
57. Chen, S., et al., *Dissipative particle dynamics simulation of polymer drops in a periodic shear flow*. Journal of Non-Newtonian Fluid Mechanics, 2004. **118**(1): p. 65-81.
58. Pietro De Palma, P.V. and M. Napolitano, *Dissipative particle dynamics simulation of a colloidal micropump*. Physics of Fluids, 2006. **18**: p. 027103.
59. Rapaport, D.C., *The Art of Molecular Dynamics Simulation*. 2004: Cambridge University Press.

60. Greengard, L. and V. Rokhlin, *A fast algorithm for particle simulations*. Journal of Computational Physics, 1997. **135**(2): p. 280-292.
61. Kim, J., *Dynamic simulation of suspended particles and drops at finite Reynolds numbers by dissipative particle dynamics*. PhD thesis, 2003, University of California, Davis.
62. Boryczko, K., W. Dzwiniel, and D.A. Yuen, *Parallel implementation of the fluid particle model for simulating complex fluids in the mesoscale*. Concurrency and Computation: Practice and Experience, 2002. **14**(2): p. 137-161.
63. Novik, K.E. and P.V. Coveney, *Finite-difference methods for simulation models incorporating nonconservative forces*. The Journal of Chemical Physics, 1998. **109**(18): p. 7667-7677.
64. Shardlow, T., *Splitting for dissipative particle dynamics*. SIAM Journal of Scientific Computing, 2003. **24**(4): p. 1267-1282.
65. Lowe, C.P., *An alternative approach to dissipative particle dynamics*. Europhysics Letters, 1999. **47**(2): p. 145-51.
66. Pagonabarraga, I., M.H.J. Hagen, and D. Frenkel, *Self-consistent dissipative particle dynamics algorithm*. Europhysics Letters, 1998. **42**(4): p. 377-382.
67. Nikunen, P., M. Karttunen, and I. Vattulainen, *How would you integrate the equations of motion in dissipative particle dynamics simulations?* Computer Physics Communications, 2003. **153**(3): p. 407-423.
68. Dwyer, G.P., Jr. and K.B. Williams, *Portable random number generators*. Journal of Economic Dynamics and Control, 2003. **27**(4): p. 645-50.
69. Green, M.S., *Markoff random processes and the statistical mechanics of time-dependent phenomena. II. Irreversible processes in fluids*. J. Chem. Phys, 1954. **22**(3): p. 398-413.
70. Kubo, R., *Statistical-Mechanical Theory of Irreversible Processes. I. General Theory and Simple Applications to Magnetic and Conduction Problems*. J. Phys. Soc. Japan, 1957. **12**: p. 570-586.
71. Einstein, A., *On the movement of small particles suspended in a stationary liquid demanded by the molecular-kinetic theory of heat*. Annals of Physics, 1905. **17**(4): p. 891-921.
72. Tysanner, M.W. and A.L. Garcia, *Measurement bias of fluid velocity in molecular simulations*. Journal of Computational Physics, 2004. **196**(1): p. 173-183.
73. Todd, B.D., D.J. Evans, and P.J. Daivis, *Pressure tensor for inhomogeneous fluids*. Physical Review E, 1995. **52**(2): p. 1627-1638.
74. Irving, J.H. and J.G. Kirkwood, *The Statistical Mechanical Theory of Transport Processes. IV. The Equations of Hydrodynamics*. The Journal of Chemical Physics, 1950. **18**(6): p. 817-829.
75. Schofield, P. and J.R. Henderson, *Statistical Mechanics of Inhomogeneous Fluids*. Proceedings of the Royal Society of London. Series A, Mathematical and Physical Sciences, 1982. **379**(1776): p. 231-246.
76. Lovett, R. and M. Baus, *Fluid interfaces as treated by density functional theory*. Physica A, 1993. **194**(1-4): p. 93-104.
77. Evans, D.J. and G.P. Morriss, *Statistical Mechanics of Nonequilibrium Liquids*. 1990, London: Academic Press London.
78. Arya, G., E.J. Maginn, and H.-C. Chang, *Efficient viscosity estimation from molecular dynamics simulation via momentum impulse relaxation*. The Journal of Chemical Physics, 2000. **113**(6): p. 2079-2087.

79. Palmer, B.J., *Transverse-current autocorrelation-function calculations of the shear viscosity for molecular liquids*. Physical Review E, 1994. **49**(1): p. 359.
80. Hess, B., *Determining the shear viscosity of model liquids from molecular dynamics simulations*. The Journal of Chemical Physics, 2002. **116**(1): p. 209-217.
81. Ladd, A.J.C., *Equations of motion for non-equilibrium molecular dynamics simulations of viscous flow in molecular fluids*. Molecular Physics, 1984. **53**(2): p. 459 - 463.
82. Haber, S., et al., *Dissipative particle dynamics simulation of flow generated by two rotating concentric cylinders: Boundary conditions*. Physical Review E - Statistical, Nonlinear, and Soft Matter Physics, 2006. **74**(4): p. 046701-8.
83. Pivkin, I.V. and G.E. Karniadakis, *Controlling density fluctuations in wall-bounded dissipative particle dynamics systems*. Physical Review Letters, 2006. **96**(20): p. 206001-4.
84. Rubinstein, M. and R.H. Colby, *Polymer physics*. 2003: Oxford University Press New York.
85. Hagerman, P.J., *Flexibility of DNA*. Annual Reviews in Biophysics and Biophysical Chemistry, 1988. **17**(1): p. 265-286.
86. Wang, M.D., et al., *Stretching DNA with optical tweezers*. Biophysical Journal, 1997. **72**(3): p. 1335-1346.
87. Marko, J.F. and E.D. Siggia, *Stretching DNA*. Macromolecules, 1995. **28**(26): p. 8759-8770.
88. Bouchiat, C., et al., *Estimating the Persistence Length of a Worm-Like Chain Molecule from Force-Extension Measurements*. Biophysical Journal, 1999. **76**(1): p. 409-413.
89. Doi, M., *Introduction to Polymer Physics*. 1996: Oxford University Press.
90. Flory, P.J., *Principles of Polymer Chemistry*. 1953: Cornell University Press.
91. de Gennes, P.G., *Scaling Concepts in Polymer Physics*. 1979: Cornell University Press.
92. Le Guillou, J.C. and J. Zinn-Justin, *Critical exponents from field theory*. Physical Review B, 1980. **21**(9): p. 3976-3998.
93. Kong, Y., et al., *Effect of solvent quality on the conformation and relaxation of polymers via dissipative particle dynamics*. The Journal of Chemical Physics, 1997. **107**: p. 592.
94. Spenley, N.A., *Scaling laws for polymers in dissipative particle dynamics*. Europhysics Letters, 2000. **49**(4): p. 534-540.
95. Symeonidis, V. and G.E. Karniadakis, *A family of time-staggered schemes for integrating hybrid DPD models for polymers: Algorithms and applications*. Journal of Computational Physics, 2006. **218**(1): p. 82-101.
96. Symeonidis, V., G. Em Karniadakis, and B. Caswell, *Dissipative Particle Dynamics Simulations of Polymer Chains: Scaling Laws and Shearing Response Compared to DNA Experiments*. Physical Review Letters, 2005. **95**(7): p. 76001.
97. Turner, S.W.P., M. Cabodi, and H.G. Craighead, *Confinement-Induced Entropic Recoil of Single DNA Molecules in a Nanofluidic Structure*. Physical Review Letters, 2002. **88**(12): p. 128103.
98. Bakajin, O., et al., *Separation of 100-kilobase DNA molecules in 10 seconds*. Anal. Chem, 2001. **73**(24): p. 6053-6056.
99. Huang, L.R., et al., *A DNA prism for high-speed continuous fractionation of large DNA molecules*. Nature Biotechnology, 2002. **20**(10): p. 1048-1051.

100. Fu, J., J. Yoo, and J. Han, *Molecular Sieving in Periodic Free-Energy Landscapes Created by Patterned Nanofilter Arrays*. Physical Review Letters, 2006. **97**(1): p. 18103.
101. Fu, J., et al., *A patterned anisotropic nanofluidic sieving structure for continuous-flow separation of DNA and proteins*. Nature Nanotech, 2007. **2**: p. 121–128.
102. Tessier, F., J. Labrie, and G.W. Slater, *Electrophoretic separation of long polyelectrolytes in submolecular-size constrictions: a Monte Carlo study*. Macromolecules, 2002. **35**(12): p. 4791–4800.
103. Cheng, K.L., et al., *Electrophoretic size separation of particles in a periodically constricted microchannel*. The Journal of Chemical Physics, 2008. **128**: p. 101101.
104. Chen, Z. and F.A. Escobedo, *Simulation of Chain-length Partitioning in a Microfabricated Channel via Entropic Trapping*. Molecular Simulation, 2003. **29**(6): p. 417–425.
105. Streek, M., et al., *Mechanisms of DNA separation in entropic trap arrays: A Brownian dynamics simulation*. Journal of Biotechnology, 2004. **112**(1-2): p. 79–89.
106. Panwar, A.S. and S. Kumar, *Time Scales in Polymer Electrophoresis through Narrow Constrictions: A Brownian Dynamics Study*. Macromolecules, 2006. **39**(3): p. 1279–1289.
107. Lee, Y.M. and Y.L. Joo, *Brownian dynamics simulations of polyelectrolyte molecules traveling through an entropic trap array during electrophoresis*. The Journal of Chemical Physics, 2007. **127**: p. 124902.
108. Streek, M., et al., *Two-state migration of DNA in a structured microchannel*. Physical Review E, 2005. **71**(1): p. 11905.
109. Viovy, J.L., *Electrophoresis of DNA and other polyelectrolytes: Physical mechanisms*. Reviews of Modern Physics, 2000. **72**(3): p. 813–872.
110. Jendreyack, R.M., J.J. de Pablo, and M.D. Graham, *Stochastic simulations of DNA in flow: Dynamics and the effects of hydrodynamic interactions*. The Journal of Chemical Physics, 2002. **116**: p. 7752.
111. Long, D., J.L. Viovy, and A. Ajdari, *Simultaneous Action of Electric Fields and Nonelectric Forces on a Polyelectrolyte: Motion and Deformation*. Physical Review Letters, 1996. **76**(20): p. 3858–3861.
112. Andr, et al., *Polyelectrolyte/post collisions during electrophoresis: Influence of hydrodynamic interactions*. The European Physical Journal B- Condensed Matter, 1998. **4**(3): p. 307–312.
113. Sebastian, K.L. and A.K.R. Paul, *Kramers problem for a polymer in a double well*. Physical Review E, 2000. **62**(1): p. 927–939.